Università degli Studi di Ferrara

Dottorato di Ricerca in

Fisica

Ciclo XXIII

Coordinatore Prof. Filippo Frontera

Design studies of the muon detector for the SuperB experiment

Settore Scientifico Disciplinare FIS/04

Dottorando

Dott. Munerato Mauro

Tutore

Dott. Bettoni Diego

Cotutore

Dott. Cibinetto Gianluigi

Anni 2008/2010

Introduction

The SuperB project is an international collaboration to build the asymmetric e^+ e^- collider and the related detector, in order to launch a high competitive physics program which will provide high precision tests of the Standard Model and possible evidence for New Physics (beyond the Standard Model). The collider and the detector will be built by a consortium, led by Istituto Nazionale di Fisica Nucleare (INFN), which includes members from USA, Canada, France, Russia, United Kingdom and other countries. Probably the location of this international experiment will be in Laboratori Nazionali di Frascati (LNF) or on the campus of the nearby University of Rome at Tor Vergata and the principal feature of this project is the high luminosity of the accelerator machine: 10^{36} cm^{-2} s^{-1}. The idea to build a more powerful machine dates back to 2001, when the two B factories, BABAR and *Belle*, published their first results on CP violation in the B meson decays. Naturally the construction of a project of this relevance embraces different fields, from engineering to physics, from geology to computing science and so on, requiring a lot of R&Ds in order to study the best current technologies to construct this cutting edge detector and accelerator machine.

In March 2007 the collaboration started with the writing of the Conceptual Design Report (CDR) and in the December 2010 the project has been approved by the Italian Government. Until this date lot of activities has been conducted and the collaboration is moving to Technical Design Report (TDR), with a detailed description of the detector and accelerator, starting point for the construction of the SuperB machine.

During these years extensive of Monte Carlo simulations, using the GEANT4 CERN package, have been carried out in order to study different geometry detector, and accelerator, configurations to search the best choice for SuperB detecttor and to satisfy the physics constraints. Naturally a detector is composed by different sub-detectors and the subject of this thesis is in particular the design study of the Instrumented Flux Return, i.e. the muon detector.

This thesis is composed by these chapters:

Chapter 1: this chapter explains the physics goals of the SuperB project: starting from results of the current B factories, the SuperB project can improve these results and in particular can find some signals of New Physics;

Chapter 2: a detector that can satisfy physics constraints is needed. In this chapter there are detailed descriptions of the SuperB detectors and accelerator.

Chapter 3: this thesis section is focused on all the aspects of the muon detector for the SuperB experiment: the Instrumented Flux Return. This chapter will present a general overview of this detector, including R&D activities, that will consist of by optical fibres carrying out signal inside the scintillator bars to silicon photo multipliers .

Chapter 4: one of the principal problems of the IFR is the neutron damage of the silicon photo multipliers. This chapter, starting from simulations, studies the neutron rate on the IFR detector and shows a possible solution to avoid high neutron rate.

Chapter 5: the optimization of a detector is one of the main subjects. In fact in this chapter will present different geometry configurations studied, starting from the CDR baseline design detector three different geometries has been proposed and studied, in particular analyzing the impact of a fixed geometry on the muon identification. These studies have been possible with a software package which will be described in this chapter,where there is also a section focused on the study of the hadronic shower behaviour inside the IFR detector.

Chapter 6: during the last period of the Ph. D. course the prototype has been assembled in Ferrara and tested at Fermilab. In this chapter there we will show the structure of the prototype and we will give a first look at the data sample collected during the first Fermilab beam test in November - December 2010.

Conclusions

Contents

Chapter 1

The physics at SuperB

The next decade will be focused on physics of elementary particles, in particular on the search for evidence of physics beyond the Standard Model. While LHC at CERN will search the Higgs boson and in general it is possible to search new physics at energies around 1 TeV, another way is to find some new virtual effects in decays of Standard Model particles such as B and D meson and τ leptons.

With the B-factories PEP-II/BABAR and KEKB/Belle it has been possible to show that the CKM phase explains all CP-violating phenomena in B decays. With these B-factories it has been possible to improve knowledge on flavour physics and to test the Standard Model on the quark and lepton sectors. The SuperB project will provide a much larger data sample, about 75 ab^{-1}, so new studies will be possible. The power of this new B-factory is the capability to measure the CP-violating asymmetries in very rare b decays, c quark decays and the possibility to access branching fractions of heavy quark and heavy lepton decay, studying either extremely rare or forbidden decays in the Standard Model.

1.1 What has be done and what SuperB could do

BABAR and Belle, measuring the CP-violating asymmetries in the B meson system, have shown that the CKM phase allows all observed CP-violating phenomena in b decays.

It is known that the Unitarity Triangle(UT) provides us with a set of tests about the self-consistency of the three generation Standard Model. Fig. 1.1 shows the Unitarity Triangle before the SuperB with allowed regions in $\overline{\rho} - \overline{\eta}$ plane delineated only by sides of triangle (dashed lines). The ellipses show statistical errors for different theoretical parameters chosen.

While in Fig. 1.1 it is possible to see the Unitarity Triangle with present errors, Fig.

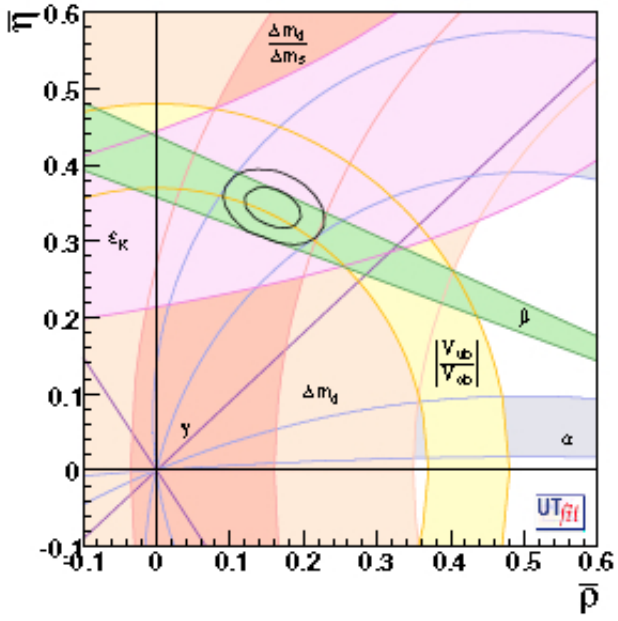

Figure 1.1: *The Unitarity Triangle with present errors.*

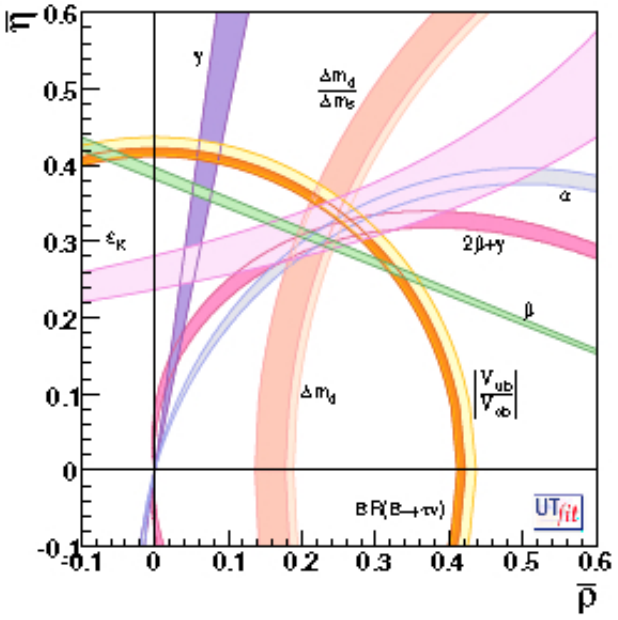

Figure 1.2: *The Unitarity Triangle with errors expected at SuperB.*

1.2 shows the triangle with errors expected at SuperB. With the SuperB precision, the discrepancies would indicate the presence of New Physics in the flavour sector.

At present, the two B Factories, BABAR and Belle, will accumulate a total of $\sim$2 ab^{-1} of integrated luminosity, and the crucial problem about the construction of the Unitarity Triangle is the limited statistics. It is convenient to analyze different sectors of Physics improved by B-factories, and to compare these with the results expected from SuperB.

1.1.1 B Physics at the $\Upsilon(4S)$

A convenient representation of UT is shown in figure 1.3 and one of the unitarity conditions of the CKM matrix is given by:

$$V_{ud}V_{ub}^{*} + V_{cd}V_{cb}^{*} + V_{td}V_{tb}^{*} = 0 \tag{1.1}$$

In the physics literature it is possible to find popular conventions for the UT:

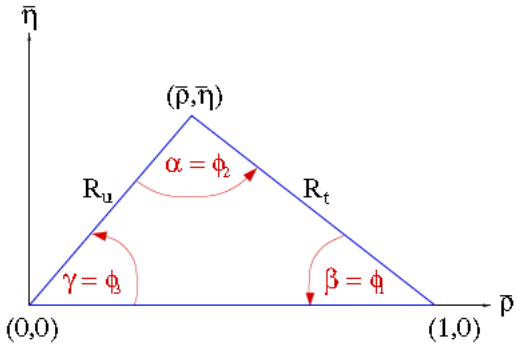

Figure 1.3: *The Unitarity Triangle.*

$$\alpha \equiv \phi_2 = \arg\left[-\frac{V_{td}V_{tb}^{*}}{V_{ud}V_{ub}^{*}}\right], \quad \beta \equiv \phi_1 = \arg\left[-\frac{V_{cd}V_{cb}^{*}}{V_{td}V_{tb}^{*}}\right], \quad \gamma \equiv \phi_3 = \arg\left[-\frac{V_{ud}V_{ub}^{*}}{V_{cd}V_{cb}^{*}}\right]$$

The B physics is aimed to measure the properties of this triangle and to search a New Physics effects, this will continue to be a crucial point of physics program of SuperB.

Status of β measurements

Through mixing-induced CP violation in the decay $B^0 \to J/\psi K^0$ it is possible to measure the $\sin(2\beta)$, one of the theoretically cleanest channels. The world average measurements of $\sin(2\beta)$[14, 37, 27]:

$$\sin(2\beta) = 0.675 \pm 0.026 \tag{1.2}$$

This result provides one of the tightest constraints on the Standard Model parameters in the $\overline{\rho}-\overline{\eta}$ plane and this channel is an important benchmark of any B physics experiment. BaBar and Belle analysis evidence that the systematic uncertainty of this channel is $\sim$0.010 [72].

This channel is an important benchmark for any B physics experiment, and a best understanding of detector-related systematic effects will have benefits for all analyses. In particular, using the high statistics available at SuperB, it will be possible to reduce this error from 0.010 to $\sim$ 0.005.

Complementary measurements of β

In the previous paragraph we showed a decay which is important for B physics. Decays such as $B^0 \to J/\psi\pi^0$ and $B^0 \to D^+D^-$ are expected to be dominated by the $b \to \overline{c}cd$ tree diagram, even if contributions from the $b \to d$ penguin amplitude are also allowed.

It is possible to see some effects of New Physics in the $b \to d$ penguin topology, for example in decays such ad $B^0 \to D\pi^0$, where the D meson is reconstructed from CP eigenstate (K^+K^-) or from a multibody final state ($K^0_S\pi^+\pi^-$). This channel also allows a clean determination of $\cos(2\beta)$ [35].

With 75 ab^{-1}, these channels will provide measurements of $\sin(2\beta)$ and $\cos(2\beta)$ with precisions of about 0.02 and 0.04 respectively.

Measurement of β with $b \to s$ penguins

Some New Physics effects happen in mixing-induced CP violation in the $b \to s$ penguin transition, in fact New Physics particles can cause deviations from Standard Model predictions.

Recent calculations indicate there are modes with smallest uncertainties, such as $B^0 \to \phi K^0$, $B^0 \to \eta' K^0$ and $B^0 \to K^0\overline{K}^0K^0$, these uncertainties are $\sim 0.02 - 0.05$[63, 62]. The current world averages of $\sin(2\beta)$ measured using these decays have uncertainties of 0.18, 0.07 and 0.21 respectively[43, 39, 40]. At the end of this decade, these errors are estimated to be reduced by a factor of $\sqrt{2}$.

Some studies [64, 12, 59] have showed that 75 ab^{-1} are needed to reduce the experimental error to the level of theoretical precision in $B^0 \to \phi K^0$ and $B^0 \to K^0\overline{K}^0K^0$. These analyses provide constraints on the hadronic parameters by using as input a large number of branching fractions of charmless hadronic B decays; the complete set of these measurements can be obtained at SuperB Factory, where it will be possible to study also $B^0 \to \pi^0K^0, B^0 \to \rho^0K^0, B^0 \to \omega K^0, B^0 \to f_0K^0$. While hadronic machines perform well on study of time-dependent CP asymmetries in $B_s \to \phi\phi$ decay, the SuperB machine,

running at $\Upsilon(5S)$, can complete these results with measurements of related channels such as $B_s \to K^0\overline{K}^0, B_s \to \phi\eta, B_s \to \eta\eta'$.

Measurement of γ

A large number of techniques for measuring γ has been proposed, because many different processes are sensitive to the UT angle γ.

Using $B \to DK$ decays, it is possible to investigate the $D^0(b \to c\bar{u}s$ transition) or a $\overline{D}^0(b \to u\bar{c}s)$ production studying the interference between these amplitude, that is correlated to the γ angle.

The sensitivity to γ depends on the (unknown) ratio of the magnitudes of the $b \to u$ and $b \to c$ decay amplitudes, denoted r_B, as well as on the structure of the D decays.

BABAR and Belle have made measurements for each of these channels cited [41, 42] and the most precise constraints on γ:

$$\text{BABAR: } \gamma = (92 \pm 42 \pm 11 \pm 12) \quad \text{Belle: } \gamma = (53^{+15}_{-18} \pm 3 \pm 9)$$

currently come from analyses of the multibody decay $D \to K^0_S\pi^+\pi^-$ [15, 79].

Using all the available measurements, the value of γ is determined with an error of about 20, the central value of r_B is found to be around 0.08 [33], slightly smaller than the expectation.

Recent studies [8] have shown that with 2 ab^{-1}, assuming r_B =0.10 and a Dalitz plot model error of 6°, the uncertainty on γ can be reduced to $\sim 6.4°$.

With 75 ab^{-1}, it should be possible to determine the γ angle with an uncertainty of 2°-3° using decays to CP eingenstates and double-Cabibbo suppressed states alone; assuming that D decays model can be improved and exploiting the large variety of D decays, at SuperB an uncertainty of 1° may be possible.

Measurement of $2\beta + \gamma$

Interference effects between $b \to c$ and $b \to u$ decay amplitudes in $B^0 \to D^{(*)\pm}\pi^{\mp}$ and $B^0 \to D^{(*)\pm}\rho^{\mp}$ allow to measure the combination of two angles of UT, in particular $2\beta + \gamma$. Starting from these analyses the $r\sin(2\beta + \gamma \pm \delta)$ can be determined, where r is the absolute ratio of the $b \to u$ and $b \to c$ decay amplitudes and δ the difference between their strong phase. Measurements from BABAR ($D^{(*)\pm}\pi^{\mp}$, $D^{(*)\pm}\rho^{\mp}, D^{\pm}\pi^{\mp}$) and from Belle (not the $D^{(*)\pm}\rho^{\mp}$ channel) have been used for performing these three variables and now the world average is $2\beta + \gamma = \pm(90 \pm 33)$[47].

With SuperB luminosities precise constraints can be imposed on the $2\beta+\gamma$ angle, and the uncertainty could be better than 5°.

Measurement of α

The measurement of the angle α derives from the interference between $B^0\overline{B^0}$ mixing and the $b \to u$ decays amplitude, for example $B \to \pi\pi$, $B \to \rho\pi$ and $B \to \rho\rho$. One method for extracting α is to use an isospin analysis of $B \to \pi\pi$[61], the same method can also be employed on $B \to \rho\rho$ analysis. While the B decay into $\pi\pi$ can be described in terms of isospin amplitudes with $\Delta I = 1/2, 3/2, 5/2$, the decay into $\rho\pi$ is more complicated.

Combining all the available analyses, α can be determined quite precisely, the current value is $\alpha = (92 \pm 7)$[57]. However it has been shown that the effect of the dominant electroweak penguin (EWP) operators, can be included in the isospin analysis and their effects produce a shift in the extracted value of α equal to $(1.5 \pm 0.3 \pm 0.3)$, where the first error is experimental and the second comes from neglected subdominant EWP operators [34, 91].

The uncertainty on α induced by the EWP correction to the isospin analyses can be reduced at SuperB. The strength of this experiment is that multiple approaches are possible: studying decays of B into $\pi\pi$ and $\rho\rho$, the consistency between the results for α, obtained in the different channels, will allow to test with high statistics the theoretical assumptions used to extract α.

1.2 CKM Elements $|V_{ub}|$ and $|V_{cb}|$

The determination of the CKM matrix elements V_{cb} and V_{ub} from inclusive and exclusive semileptonic decays, needs a most precise knowledge of the branching fractions. This knowledge is possible improving the detector acceptance and the detection efficiency for neutral and charged particles, because semileptonic decays involve an undetected neutrino.

The reduced beam-energy asymmetry at SuperB leads to an increase in solid-angle coverage; in fact detailed studies of detection efficiencies and misidentification rates with a large control sample data are critical to achieving simulations accurate to better than one percent.

In this section is possible we will review current measurements on inclusive and exclusive semileptonic decays and the possible improvement with SuperB experiment.

Perspectives on Exclusive Semileptonic Measurements

Measurement of exclusive decays such as $B \to \pi l \nu$ can give a very precise determination of $|V_{ub}|$. From the experimental point of view, it is possible to provide measurements of $\delta\Gamma/\delta q^2$, where the q^2 is the invariant mass-squared of the lepton-neutrino pair.

For reducing the background and improving the determination of kinematic quantities, some different tagging techniques have been developed, using a full or partial reconstruction of one of the two B mesons in the event. In particular the signal-to-background ratio is about 20 times higher for the tagged reconstruction approach than for the untagged one. BABAR studies showed that the full reconstruction techniques provide an error on the branching fraction of 29%, dominated by the 25% statistical uncertainty.

At SuperB, the branching fraction can be measured with a precision of a few percent, a total error of 3-4% on $|V_{ub}|$ from exclusive analyses appears possible with large SuperB data samples.

About the $|V_{cb}|$ matrix element, the experimental and theoretical uncertainties are currently $\sim 3\%$. It is difficult to improve the experimental uncertainties, due principally to detector effects, such as reconstruction of the low momentum pion from the decay of the D^* meson, below 1-2%. The simultaneous measurement of $B \to Dl\nu$ and $B \to D^*l\nu$ would be useful for a better control of the background. So a total error on $|V_{cb}|$ of 1-2% from exclusive analyses can be expected at SuperB.

Perspectives on Inclusive Semileptonic Measurements

At the current B factories, the determination of $|V_{cb}|$ has a precision of a 1.5%, utilizing the total decay rate and lepton spectra for inclusive semileptonic B meson decays into charmed final states. By the start of SuperB, $|V_{cb}|$ is expected to be determined inclusively with a total error below 1%.

For the determination of $|V_{ub}|$, the situation is more complicated because charmless inclusive semileptonic decays play a crucial role. In fact the separation of the $B \to X_u l\nu$ signal from the $B \to X_c l\nu$ requires strict kinematical cuts. For future inclusive determinations of $|V_{ub}|$, it is important to minimize the dependence on the shape function by avoiding overly stringent kinematical cuts at the expense of higher backgrounds. The large data sample available at SuperB is useful because it can improve the determination of the backgrounds.

It is important to note that the most important remaining source of theoretical error on $|V_{ub}|$ from inclusive measurements would be the mass of the bottom quark, so a determination of $|V_{ub}|$ with a precision of about 2% might be possible.

Measurement of $\mathcal{B}(B \to D^{(*)}\tau\nu)$

The decays $B \to D\tau\nu$ and $B \to D^*\tau\nu$ are sensitive to New Physics through virtual exchange of charged Higgs bosons. In the Standard Model the branching fraction is about

8×10^{-3}. A large data sample is so required with respect to that used for measuring the $\mathcal{B}(B \to D^{(*)}\mu\nu)$ and $\mathcal{B}(B \to D^{(*)}e\nu)$. Simulations show that by combining hadronic and leptonic τ decays, a relative precision of $\sim 10\%$ can be reached with 2 ab^{-1}. With more statistics, provided by SuperB, the precision of this measurement can be improved to 2%.

1.3 Rare Decays

The New Physics window can be explored with rare B decays. These are highly suppressed within the Standard Model, so when New Physics is introduced some effects can be observed. With the clean environment and excellent particle identification of SuperB, a large number of rare decays can be studied. It is possible to provide here a brief summary of these channels.

Leptonic Decays: $\mathcal{B}(B \to l^+\nu_l(\gamma))$ and $\mathcal{B}(B^0 \to l^+l^-)$

Leptonic decay processes are described by annihilation diagrams and the rate of these decays are proportional to $f_B^2|V_{ub}|^2$, where f_B is the same pseudoscalar constant that enters the determination of Δm_d.

The branching fractions are expected to be about 10^{-4} for $\mathcal{B}(B^+ \to \tau^+\nu_\tau)$, 5×10^{-7} for $\mathcal{B}(B^+ \to \mu^+\nu_\mu)$ and 10^{-11} for $\mathcal{B}(B^+ \to e^+\nu_e)$. The first decay has recently been reported [65], and the world average for the branching ratio is $\mathcal{B}(B^+ \to \tau^+\nu_\tau) = (1.3 \pm 0.5) \times 10^{-4}$; for the muonic decay upper limits are approaching the Standard Model expectation [45], while those for the highly suppressed $B \to e^+\nu_e$ decay are still far away from the Standard Model value.

We focus now on the measurement of branching ratios for these different leptonic decays.

$\mathcal{B}(B^+ \to \tau^+\nu_\tau)$

Since the decay of the τ lepton necessarily involves at least one neutrino, there are multiple sources of missing energy, making conventional reconstruction techniques impossible.

The analysis technique proceeds by reconstructing either exclusively or partially on a B meson in the event (the *tag*), and compares the remainder of the event with the signature for the signal decay. Current analyses assign total systematic errors of more than 10%; with 75 ab^{-1} the statistical error will be about 3-4%, so the systematic effects will have to be much better controlled to match this statistical precision.

$\mathcal{B}(B^+ \to \mu^+\nu_\mu)$

Unlike tauonic decay, the muonic decay has a very unique signature: a high transverse muon momentum and a missing energy vector that balances the momentum of the lepton. It is expected to have a statistical error of 5% on the measured branching fraction at the Standard Model value. Since the backgrounds are small, it should be possible to control systematic errors to a similar value.

$\mathcal{B}(B^+ \to e^+\nu_e)$

The case when the lepton is an electron is as clean as the muonic mode, but the small electron mass leads to a high helicity suppression, so the rate in the Standard Model is expected to be around $\mathcal{O}(10^{-9})$, below the SuperB sensitivity.

$\mathcal{B}(B^+ \to l^+\nu_l\gamma)$ **and** $\mathcal{B}(B^0 \to l^+l^-)$

Radiative decays don't suffer the same degree of helicity suppression as the purely leptonic decays, in fact SuperB has an excellent sensitivity for $B^+ \to l^+\nu_l\gamma$ [10]. The neutrinoless decays $B^0 \to e^+e^-$, $B^0 \to \mu^+\mu^-$ and $B^0 \to \tau^+\tau^-$ can also be studied at SuperB, with their lepton flavour-violating counterparts [20, 23]. With 75 ab^{-1} the sensitivity would reach the 10^{-10} level for the e^+e^- and $\mu^+\mu^-$ final states, which is close to the Standard Model expectation for the muon mode. The tauonic decay can only be studied at SuperB factory, despite the fact that the sensitivity will still be far above the Standard Model expectation.

Radiative decays: $b \to s\gamma$ and $b \to d\gamma$

These decays are very sensitive probes of New Physics. These measurements, which can be performed at SuperB also provide clean tests of the Standard Model, they can be done in the theoretically cleaner inclusive modes, and they are not restricted only to exclusive channels.

$b \to s\gamma$**, exclusive mode**

The aim of exclusive measurements is the CP asymmetries, which have comparatively small theoretical error in contrast to the rates. Direct CP violation in these decays is expected to be $\sim 0.5\%$ in the Standard Model, but could an order of magnitude larger if there are New Physics contributions.

The most accessible channel for studying this decay mode is $B^0 \to K^{*0}\gamma$, but it is possible to obtain an average with the $B^+ \to K^{*+}\gamma$, and search for isospin violation, caused by New Physics. The current experimental average is $A_{CP}(B \to K^*\gamma) = -0.010 \pm 0.028$ [24, 54, 75].

With 75 ab^{-1}, the limiting factor in this measurement will be the systematic uncertainty due to asymmetries in the detector response to positive and negative kaons. With the SuperB factory it will be possible to have an ultimate precision around 0.4%.

$b \to d\gamma$, exclusive mode

The ratio of rates of $b \to d\gamma$ and $b \to s\gamma$ decays, can give a crucial determination of $|V_{td}/V_{ts}|$, completing the information obtained from the ratio of oscillation frequencies $\Delta m_d/\Delta m_s$. This ratio can be measured utilizing branching fractions $\mathcal{B}(B \to \rho\gamma)/\mathcal{B}(B \to K^*\gamma)$; the current experimental world averages are $\mathcal{B}(B^0 \to \rho^0\gamma) = (0.91 \pm 0.19) \times 10^{-6}$ [24, 9, 17] and $\mathcal{B}(B^0 \to K^{*0}\gamma) = (40.1 \pm 2.0) \times 10^{-6}$[24, 54, 75]. The limiting factor is currently the statistical precision $\mathcal{B}(B^0 \to \rho^0\gamma)$, but, with the SuperB statistics of 75 ab^{-1}, it can be reduced to a level of about 2% and it is also possible to measure the direct CP asymmetries in the $b \to d\gamma$ processes, which have not been seen at the current B Factories, with a precision of about 10%, value expected by the Standard Model.

$b \to s\gamma$, inclusive mode

Measurements of this inclusive branching fraction provide clean constraints on New Physics. Theoretical calculations of the Standard Model give the value of $\mathcal{B}(B \to X_s\gamma, E_\gamma > 1.6 \text{ GeV}) = (3.15 \pm 0.23) \times 10^{-4}$ [73], which is in good agreement with the latest experimental determination $(3.53 \pm 0.24 \pm 0.10 \pm 0.03) \times 10^{-4}$[24, 21, 70, 38]. Even though further reduction of the theoretical error will be difficult, with larger statistics, so with improved measurements of the total rate, is possible to improve our knowledge of the photon energy spectrum.

The current world average for the CP asymmetry is $A_{CP}(B \to X_s\gamma) = 0.004 \pm 0.037$,[24], using results in which both BABAR[18] and Belle[76] reconstruct the X_s as sum of exclusive final states and correct for the missing fraction. With the SuperB experiment, the level of precision is limited to the same level as the exclusive modes, about 0.004.

$b \to d\gamma$, inclusive mode

This inclusive mode has not been studied at the B factories, but preliminary studies show that such analysis can be possible around 10 ab^{-1}, so this result is very interesting with the full SuperB statistics. In the Standard Model, the partial width differences in $b \to s\gamma$ and $b \to d\gamma$ should cancel, so the $A_{CP}(B \to X_{s+d}\gamma)$ is predicted to be zero. With SuperB statistics it will be possible to do this using full reconstruction of the other B meson in the event. A first measurement of $A_{CP}(B \to X_{s+d}\gamma)$ has been carried out by BABAR[25], but with SuperB this asymmetry can be measured to subpercent precision.

Photon polarization measurements

In the Standard Model photons emitted in radiative b decays are predominantly left-handed, while those emitted in $\bar{b}$ decay are right-handed. The amplitude for the emission of wrong-helicity photons is suppressed by a factor proportional to m_q/m_b, where m_q=m_s for $b \to s\gamma$ and m_q=m_d for $b \to d\gamma$ transitions.

A signal of New Physics can modify this suppression without introducing any CP violating phase, so measurements of the photon polarization provide a powerful approach to search for New Physics. Different methods of measuring this polarization have been suggested, but the only approach adopted so far uses mixing-induced CP asymmetries to examine the level of interference between b and $\bar{b}$ decays[50, 51]. The current experimental world average is $S(K^0_S\pi^0\gamma)$=-0.09 ± 0.24[24, 22, 86]. Using the recent results from BABAR ($S(K^0_S\pi^0\gamma)$=-0.06 ± 0.37 [22], obtained with $\sim$ 220 fb^{-1}) and extrapolating these, is possible to estimate a precision of 0.02, that could be reached with 75 ab^{-1}.

The same approach can be used with different final states, as $B^0 \to K^0_S\eta\gamma$, $B^0 \to K^0_S\phi\gamma$, $B^0 \to \rho^0\gamma$ and $B^0 \to \omega\gamma$. A precision of ~ 0.10 on S($\rho^0\gamma$) can be obtained with 75 ab^{-1} and this could be an unmistakable sign of a New Physics.

Radiative Decays: $b \to sll$ and $b \to dll$

Exclusive modes such as $B \to Kl^+l^-$ and $B \to K^*l^+l^-$, with $l = e, \mu$, can be used for studying rates, direct CP asymmetries and the forward-backward asymmetry A_{FB}. The results from BABAR[26] and Belle[66] show some hints of New Physics effects, but the precision of the B Factories in not sufficient for making the required stringent tests.

With SuperB experiment it is possible to study a larger set of interesting channels, and also parameters for the inclusive decays can be measured. B Factories carried out initial studies of the exclusive process $b \to sl^+l^-$[19, 67], and SuperB could be able to probe the asymmetries down to the percent level.

Radiative decay: $b \to s\nu\overline{\nu}$

Both BABAR [16] and Belle[11], studied channels in which the emitted leptons are neutrinos; the study of these B decays is challenging. The B Factories obtained limits of $\mathcal{B}(B^+ \to K^+\nu\overline{\nu})$=$40 \times 10^{-6}$, about an order of magnitude above the Standard Model expectation. With SuperB statistics it is expected to have about 20% relative error for this branching fraction, and it is also possible to study $b \to s\nu\overline{\nu}$ channels, such as $B \to K^*\nu\overline{\nu}$; the sensitivity is such that it should be possible to observe $B^+ \to \pi^+\nu\overline{\nu}$.

Charmless Hadronic B Decays

Studies of charmless hadronic B decays are highly sensitive to new Physics contributions both in rates and in direct CP asymmetries. This kind of tests can be performed at the SuperB factory, and with 75 ab^{-1} it is possible to reach a precision of 1-2%[60]. As well for the other hadronic decays, the important extraction of information on fundamental Standard Model and New Physics parameters requires a model-independent check, preferably on data, of the theoretical predictions: SuperB can do this.

The measurements that can be performed at the SuperB Factory will be important attempts for improving our knowledge of different theoretical issues related to hadronic amplitudes (factorization, power corrections, flavour-symmetry breaking, etc.) and reduce the associated theoretical uncertainties.

1.4 Summary of experimental expectations

As described in this chapter, SuperB with an expected integrated luminosity of 75 ab^{-1} can perform a wide range of crucial measurements and can, in a sensitive manner, improve upon the results from the current B Factories. In particular it can be useful to classify the various results in two categories:

- **Searching for New Physics** Lot of measurements can be made at SuperB that are sensitive to New Physics effects, for example the mixing-induced CP asymmetry parameter for $B^0 \to \phi K^0$ decays can be measured to a precision of 0.02, as can equivalent parameters for numerous decay channels dominated by the $b \to s$ penguin transition. These are very stringent tests of any New Physics scenario which introduces new CP violation sources, beyond the Standard Model.

- **Future metrology of the CKM matrix** There are several measurements which are not affected by New Physics effects and which allow us to improve out knowledge

on the CKM parameters, for example the γ angle can be measured with a precision of 1°-2°and the precision of $|V_{ub}|$ and $|V_{cb}|$ can be improved.

In Tab. 1.1, 1.2 it is possible to see a schematic summary of all experimental expectations from the SuperB Factory.

Table 1.1: *Precisions reached with the current B factories at 2 ab^{-1} compared to those that can be obtained with SuperB, with 75 ab^{-1}.*

Observable	B Factories (2 ab^{-1})	SuperB (75 ab^{-1})
$\sin 2\beta(J/\psi K^0)$	0.018	0.005
$\cos 2\beta(J/\psi K^{*0})$	0.30	0.05
$\sin 2\beta(Dh^0)$	0.10	0.02
$\cos 2\beta(Dh^0)$	0.20	0.04
$S(J/\psi\pi^0)$	0.10	0.02
$S(D^+D^-)$	0.20	0.03
$S(\phi K^0)$	0.13	0.02
$S(\eta' K^0)$	0.05	0.01
$S(K^0_S K^0_S K^0_S)$	0.15	0.02
$S(K^0_S\pi^0)$	0.15	0.02
$S(\omega K^0_S)$	0.17	0.03
$S(f_0 K^0_S)$	0.12	0.02
$\gamma(B \to DK, D \to$ CP eingenstates)	∼15°	2.5°
$\gamma(B \to DK, D \to$ suppressed states)	∼12°	2.0°
$\gamma(B \to DK, D \to$ multibody states)	∼9°	1.5°
$\gamma(B \to DK$, combined)	∼6°	1°-2°
$\alpha(B \to \pi\pi)$	∼16°	3°
$\alpha(B \to \rho\rho)$	∼7°	1°-2°
$\alpha(B \to \rho\pi)$	∼12°	2°
α(combined)	∼6°	1°-2°
$2\beta + \gamma(D^{*\pm}\pi^{\mp}, D^{\pm}K^0_S\pi^{\mp})$	20°	5°

Table 1.2: *Precisions reached with the current B factories at 2 ab^{-1} compared to those that can be obtained with SuperB, with 75 ab^{-1}.*

Observable	B Factories (2 ab^{-1})	SuperB (75 ab^{-1})
$\|V_{cb}\|$ exclusive	4%	1.0%
$\|V_{cb}\|$ inclusive	1%	0.5%
$\|V_{ub}\|$ exclusive	8%	3.0%
$\|V_{ub}\|$ inclusive	8%	2.0%
$\mathcal{B}(B \to \tau\nu)$	20%	4%
$\mathcal{B}(B \to \mu\nu)$	visible	5%
$\mathcal{B}(B \to D\tau\nu)$	10%	2%
$\mathcal{B}(B \to \rho\gamma)$	15%	3%
$\mathcal{B}(B \to \omega\gamma)$	30%	5%
$A_{CP}(B \to K^*\gamma)$	0.007	0.004
$A_{CP}(B \to \rho\gamma)$	$\sim$0.20	0.05
$A_{CP}(b \to s\gamma)$	0.012	0.004
$A_{CP}(b \to (s+d)\gamma)$	0.03	0.006
$S(K^0_S\pi^0\gamma)$	0.15	0.02
$S(\rho^0\gamma)$	possible	0.10
$A_{CP}(B \to K^*ll)$	7%	1%
$A_{FB}(B \to K^*ll)$	25%	9%
$A_{FB}(B \to X_sll)$	25%	5%
$\mathcal{B}(B \to K\nu\overline{\nu})$	visible	20%
$\mathcal{B}(B \to \pi\nu\overline{\nu})$	-	possible

Chapter 2

The SuperB project: accelerator and detector

SuperB is a project founded on international collaboration with the aim to construct an asymmetric e^+e^- collider, with a luminosity of order 10^{36} cm^2 s^{-1}, taking a larger number of data with respect to the current B Factories, BABAR and Belle. The SuperB accelerator will be installed in Italy near Frascati(RM) and it will be an asymmetric collider, in which a 4 GeV e^+ beam collides with a 7 GeV e^- beam. Fig. 2.1 shows a possible location for SuperB facility.

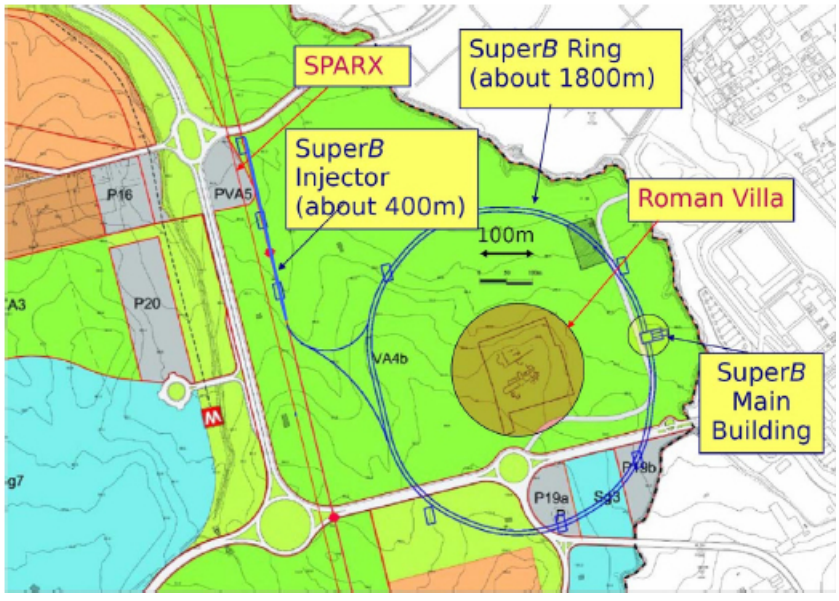

Figure 2.1: *The SuperB site at the Campus of Tor Vergata University.*

The SuperB collider, operating at the unprecedented luminosity of 10^{36} cm^2 s^{-1}, can collect in a running year (10^7 s) about 15 ab^{-1} (see Fig. 2.2), so 7 times the total data samples collected by the current B factories.

The design of the SuperB collider combines the extensions of the design of the current B

Figure 2.2: *SuperB luminosity.*

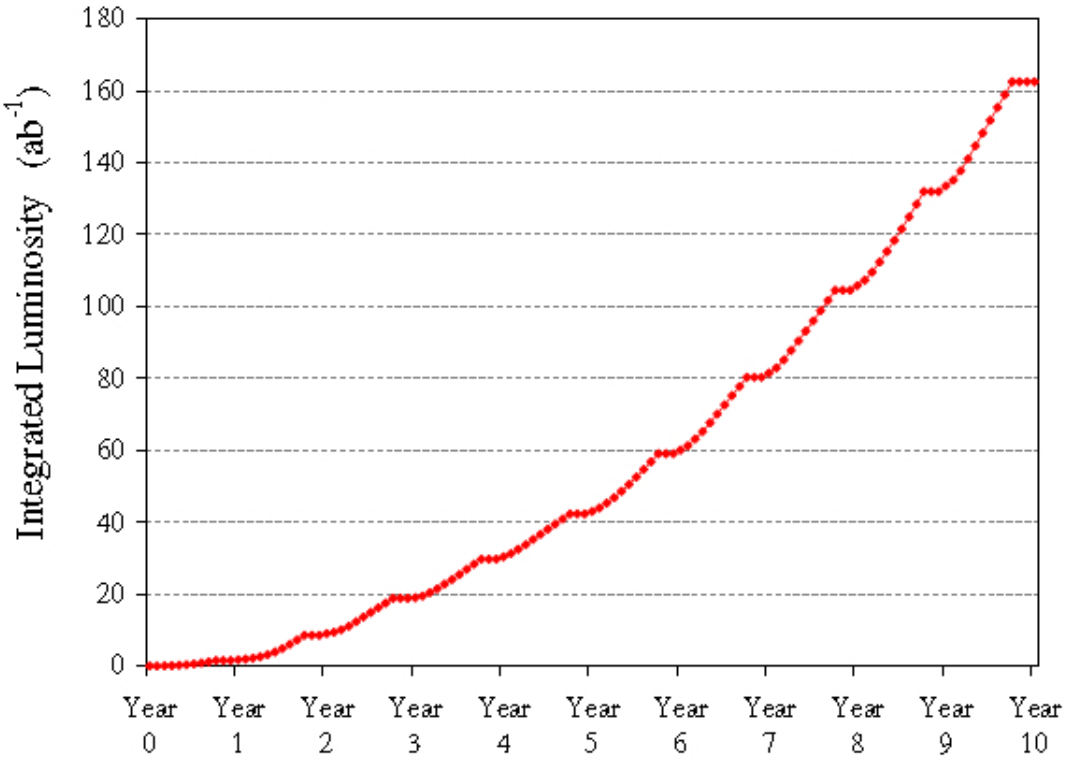

(a) The SuperB integrated luminosity projection over 10 years.

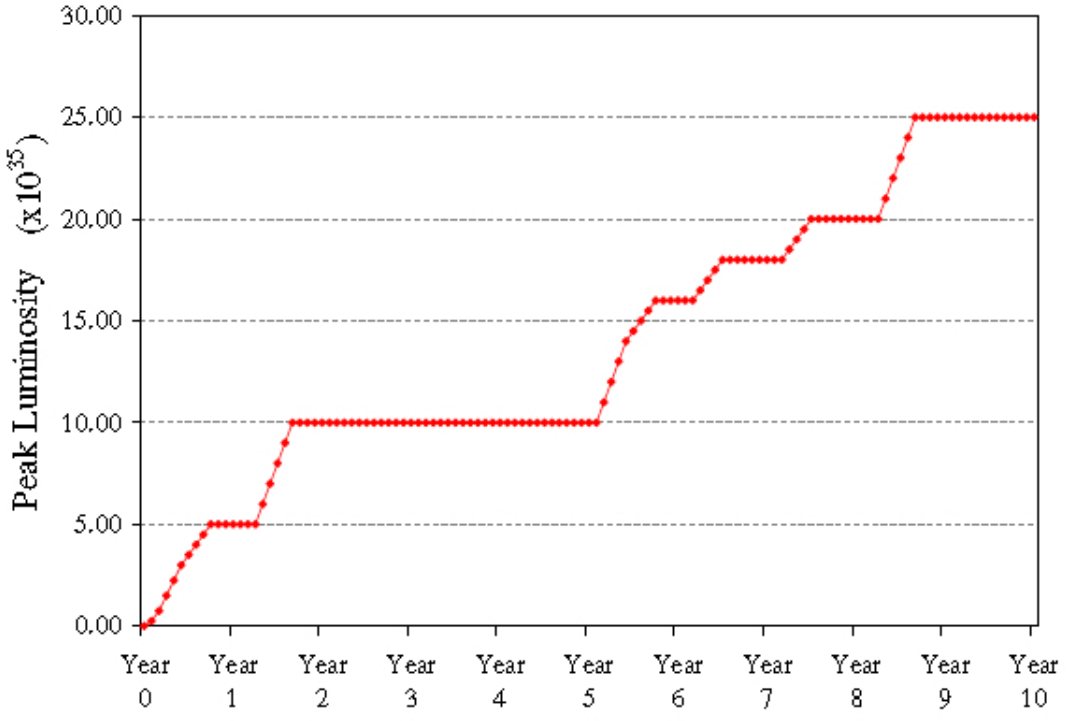

(b) The SuperB peak luminosity projection over 10 years.

Factories with new linear collider concepts to produce an extraordinary leap in B Factory luminosity without increasing beam currents or power consumption.

It is crucial to note that the union between the innovation of the continuos injection and the high efficiency of the accelerator and detectors is the key point of the SuperB project.

In this chapter we will show some features of this new collider and each part of the detector will be described in detail.

2.1 The accelerator

The luminosity $\mathcal{L}$ of an e^+e^- collider is given by the expression

$$\mathcal{L} = \frac{N^+ N^-}{4\pi\sigma_y\sqrt{(\sigma_z \tan\theta/2)^2 + \sigma_x^2}} f_c \tag{2.1}$$

$$\sigma_{x,y} = \sqrt{\beta_{x,y}\epsilon_{x,y}} \tag{2.2}$$

where f_c is the frequency of collision of each bunch, $N^{+(-)}$ is the number $e^{+(-)}$, σ is the beam size in the considered directions (x,y,z), ϵ the emittance, β is the beta function (in cm) at the collision point in each plane and θ is the crossing angle between the beam lines at the interaction point (IP).

The principal innovation of the SuperB collider is the "crabbed waist", a new scheme of collision: this allows to reach the high luminosity of 10^{36} cm^2s^{-1}, without increasing the beam currents and decreasing the bunches length. In Tab. 2.1 the parameters of the accelerator are listed.

2.1.1 Crabbed Waist

In high luminosity colliders, one of the key requirements are the very short bunches, in order to decrease the β_y^* at the interaction point, and low emittance. Moreover high luminosity requires small vertical emittance, so large horizontal beam size and horizontal emittance, to minimize the beam-beam effect; unfortunately this is difficult to obtain.

With the crabbed waist scheme[80] for beam-beam collisions it is possible to reach high luminosity without decreasing the bunch length, using one crucial idea:

large Piwinski angle for collisions at a crossing angle θ, the Piwinski angle is defined as:

$$\phi = \frac{\sigma_z}{\sigma_x}\tan\frac{\theta}{2}, \text{ if } \theta \ll 1 \ \phi \approx \frac{\sigma_z}{\sigma_x}\frac{\theta}{2} \tag{2.3}$$

Table 2.1: *SuperB parameters.*

Parameter	LER	HER
Particle type	e^+	e^-
Energy (GeV)	4	7
Luminosity (cm^2 s^{-1})	3.4×10^{36}	
Circumference (m)	2250	
Revolution freq. (MHz)	0.13	
Long. polarization(%)	0	80
RF Frequency (MHz)	476	
Harmonic Number	3570	
Momentum spread ($\times$ 10^{-4})	10	10
Momentum compaction ($\times$ 10^{-4})	1.8	3.0
RF Voltage (MV)	7.5	18
Energy loss/turn (MeV)	2.3	4.1
Number of bunches	3466	
Particle/bunch ($\times$ 10^{10})	6.16	3.52
Beam current (A)	4.55	2.60
β_y^* (mm)	0.20	
β_x^* (mm)	20	
ϵ_y^* (pm-rad)	2	
ϵ_x^* (nm-rad)	0.8	
σ_y^* (nm)	20	
σ_x^* (μm)	4000	
Bunch length (mm)	6	
Full crossing angle (mrad)	34	
Wigglers (#)	4	4
τ_{Damping} (trans/long) (ms)	25/12.5	
Luminosity lifetime (min)	6.1	3.5
Touschek lifetime (min)	2.3	15
Total beam lifetime (min)	1.7	2.8
Inj. rate pps (100%) $\times$ 10^{11}	21	7.2
ξ_y	0.009	
ξ_x	0.2	
RF Power (MW)	44	

where σ_x is the horizontal bunch size, σ_z the bunch length. So for a collision at crossing angle θ, the luminosity $\mathcal{L}$, tune shifts ξ_x and ξ_y scale according to [81]:

$$\mathcal{L} = \frac{\gamma^+ \xi_y N^+ f_c}{2 r_e \beta_y} \left(1 + \frac{\sigma_y}{\sigma_x}\right) \propto \frac{N^+ \xi_y}{\beta_y} \tag{2.4}$$

$$\xi_y = \frac{r_e N^-}{2\pi\gamma^+} \frac{\beta_y}{\sigma_y \left(\sigma_x \sqrt{1+\phi^2} + \sigma_y\right)} \propto \frac{N^- \sqrt{\beta_y}}{\sigma_x \sigma_y \theta} \tag{2.5}$$

$$\xi_x = \frac{r_e N^-}{2\pi\gamma^+} \frac{\beta_y}{\sigma_x^2 \left[(1+\phi^2) + \frac{\sigma_y}{\sigma_x}\sqrt{1+\phi^2}\right]} \propto \frac{N^- \sqrt{\beta_y}}{(\sigma_z \theta)^2} \tag{2.6}$$

where γ^+ is the Lorentz factor for positrons, ξ_x is the horizontal tune and ξ_y is the vertical tune. For very large ϕ angle the beam-beam interaction can be considered one-dimensional, since the horizontal footprint in the tune plane shrinks. In the crabbed waist scheme, the Piwinski angle is increased by decreasing the horizontal beam size and increasing the crossing angle. In this way, the luminosity is increased and the horizontal tune shift due to the crossing angle decreases.

The most important effect is the reduction of the overlap area of colliding bunches proportional to σ_x/θ. Thus if $\beta_y \approx \frac{\sigma_x}{\theta}$, several advantages are gained:

- Small spot size at the IP, so the luminosity is increased;
- reduction of the vertical tune shift;
- suppression of the vertical synchrobetatron resonances[52].

However, the collision at large Piwinski angle introduces new beam-beam resonances and may strongly limit the maximum achievable tune shifts [77]. Resuming the crabbed waist transformation boots the luminosity, mainly by the suppression of betatron (and synchrobetatron) resonances, that usually arise through the vertical motion modulation by the horizontal beam oscillations. Fig. 2.3 presents a sketch of the crabbed waist scheme.

The SuperB design, as seen previously, aims to reach a luminosity of 10^{36} cm^2 s^{-1}; some of the key design elements are briefly discussed here.

1. **Luminosity:** for very flat beams, the luminosity can be written as:

$$\mathcal{L} = \frac{2.17 \times 10^3 4}{\text{GeV cm C}} \frac{EI\xi_y}{\beta_y} \tag{2.7}$$

where I is the Low Energy Ring(LER) beam current, E is the LER energy, ξ_y the vertical tune shift and β_y the vertical beta at the IP.

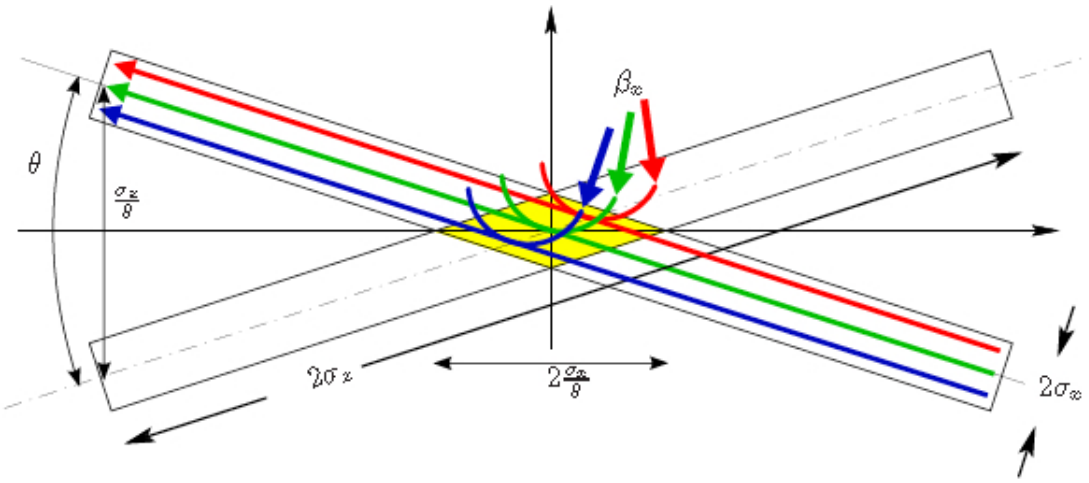

Figure 2.3: *Crabbed waist scheme, in the yellow the collision area*

2. **Synchrotron radiation power:** the power dissipation is related to the beam current by the relation:

$$P = IU_o \tag{2.8}$$

where I is the beam current and U_o the energy loss per turn. All colliders aim to minimize P, but SuperB is based on large Piwinski angle and crabbed waist scheme, allowing to decrease β_y and increasing the vertical tune shift, as described above. SuperB has a luminosity about two orders of magnitude larger than that achieved currently, with beam currents and power energy consumption essentially unchanged.

3. **Detector backgrounds:** for an experiment it is important to maintain the backgrounds under control. In the SuperB design, the combination of large crossing angle and small beam sizes, allows to decrease the background levels with respect to the current B Factories; in fact the emittances and the beam angular-divergences at the IP are very advantageous.

4. **Beam lifetime:** in the current e^+e^- factories, the beam lifetime is determined by ring characteristics, vacuum quality, dynamic aperture, etc. In the SuperB design, the beam lifetime is dominated by luminosity itself: radiative Bhabhas limit the lifetime to a few minutes for both rings but it is important to note that the Touschek lifetime causes a worsening by a factor 1.3. So the injection system must be able to provide particles at a rate about 10 times larger than those for the present factories.

5. **Beam emittance:** the horizontal emittance ϵ_x is dominated mainly by the ring lattice optics, the vertical emittance e_y is determined by ring imperfections. The

current B Factories have achieved vertical and horizontal emittance ratios similar to the SuperB design.

6. **Polarization:** SuperB can provide collisions with longitudinally polarized electrons using a polarized electron gun and spin rotators in the ring. The possibility to use the polarized electrons is being evaluated in relation to the additional physics benefit.

7. **Cost:** the SuperB accelerator is based mainly on the SLAC PEP-II machine [7], so the cost is not dominated by the requirements for dealing high luminosity: higher current and short bunches.

In the Fig. 2.4 the distribution of beams in the IR is shown, in fact it can be seen that in the intersection the two beams are thiner.

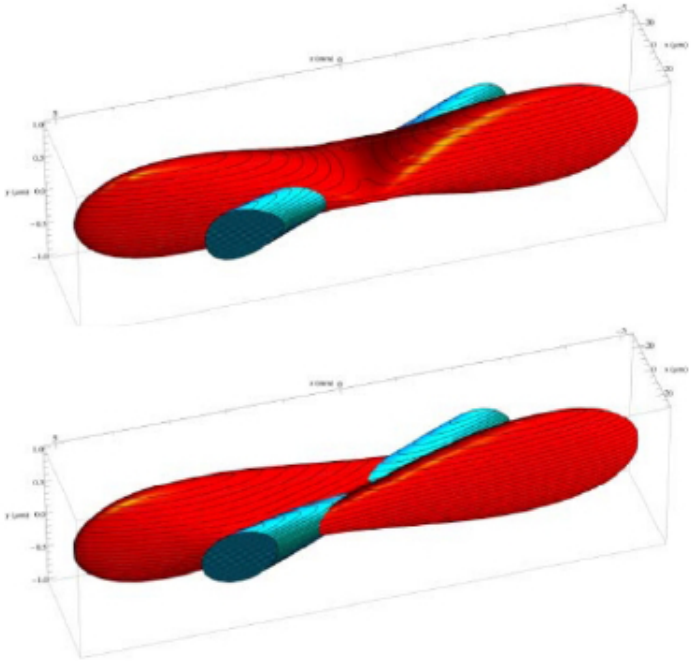

Figure 2.4: *Behavior of beams without crabbed waist (top) and with crabbed waist (bottom)*

2.1.2 The Rings

The rings of SuperB must satisfy several requirements:

- Very small emittances;
- Asymmetric energies (4×7 GeV);
- Insertion of a final focus with very small β^*;

- Good dynamic aperture and lifetimes;

- Reuse of available PEP-II hardware as much as possible.

The 7 GeV high energy ring (HER) and the 4 GeV low energy ring (LER) will be built on the same horizontal plane, with a horizontal crossing angle of 2×17 mrad. The beams will travel together only over a short section of the interaction region (IR), where they will collide at the interaction point (IP). On the opposite side of the IP the beams will be vertically separated in order not to collide, and the rings will be horizontally separated by a magnetic chicane (see Fig. 2.5).

The magnetic layouts of the two rings are identical: each ring has a 6-fold symmetry, with 6 arcs separated by 6 long straight sections, similar to the PEP-II design. Wiggler magnets will be installed in some of the straight sections in order to control the emittance and damping time.

A special final focus (FF) section brings the beams together, focuses them to the very small β functions required by the design, and separates them after the collision.

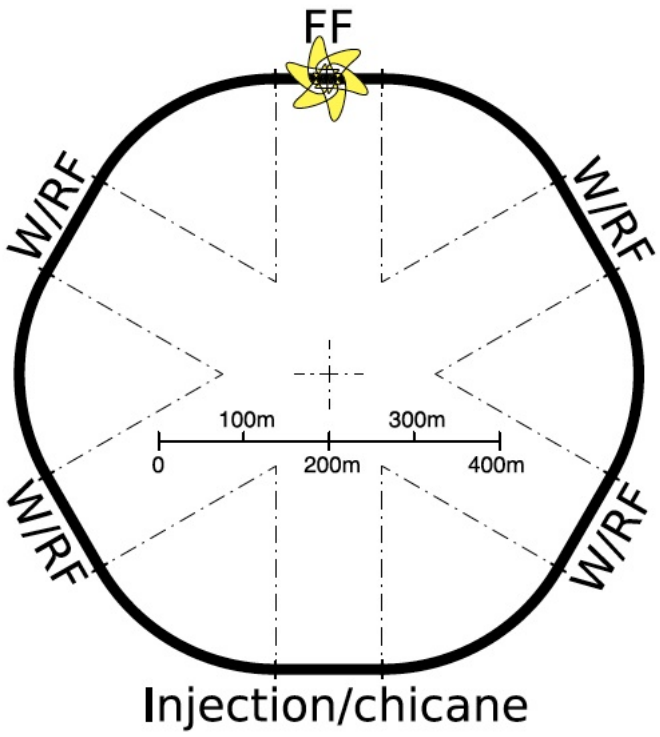

Figure 2.5: *One ring scheme.*

2.1.3 The Interaction Region

The SuperB interaction region (IR) has been designed to satisfy the following requirements:

- Very small spot sizes at the IP;
- Local correction for the very high chromaticity due to the highly focused beam, keeping geometric aberrations small;
- Separation of the LER and HER beams as soon as possible;
- Preventing synchrotron radiation (SR) production from hitting the beam pipe and the detector;
- Compatibility with a beam pipe of minimum radius and thickness;
- Keeping the largest possible angular acceptance for the detector.

In Tab. 2.2 the IP collision parameters are listed; they have been chosen based on beam-beam simulations and the crossing angle has been fixed by optimization of the interaction region design.

Table 2.2: *IP Parameters*

IP horizontal β_x	20 mm
IP vertical β_y	0.2 mm
Horizontal beam size σ_x	4 mm
Horizontal beam divergence $\sigma_{x'}$	200 mrad
Vertical beam size σ_y	20 nm
Vertical beam divergence $\sigma_{y'}$	100 mrad
Bunch length σ_z	7 mm
Crossing angle θ	2× 17 mrad

The Final Focus of the SuperB design requires small β_x^*(20 mm) and β_y^*(0.2 mm); in order to have these beta functions so small, it needs to have the FF magnets as close as possible to the IP, in order to keep also the generated chromaticity at the minimum.

Starting from the structure of PEP-II, in the SuperB design a beam-stay-clear (BSC) envelope has been maintained[7]. The x stay-clear is defined as 15 uncoupled beam σ_x + 1mm for closed orbit distortion (COD), otherwise the y stay-clear is defined as 15 fully coupled beam $\sigma_y + 1$ COD: these two envelopes are 1.8 mm. So a first quadrupole

magnet (QD0, 46 cm), shared by the two beams, has been positioned to start 0.3 m away from the IP and in order to produce similar final focus beta functions for both beams, another magnet QD0H (where the two beams enter separate beam pipes) is positioned for the high energy beam (HEB) but not for the low energy beam (LEB); the request to place the QD0H (29 cm) stems from condition to respect the high-energy beam requirements.

The interaction region layout is shown in Fig.2.6.

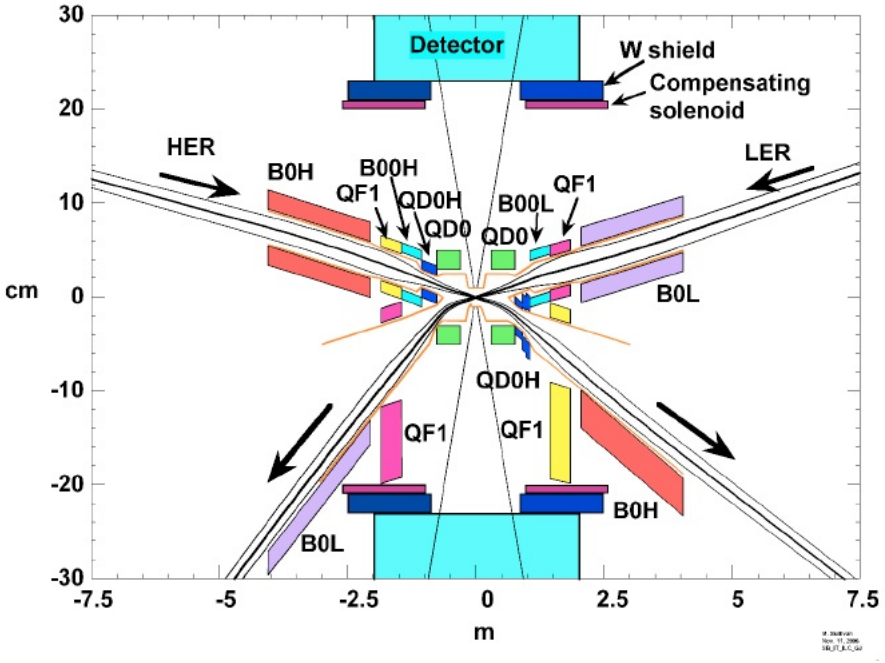

Figure 2.6: *Layout of the interaction region (two axes have different scales).*

In the Tab. 2.3 some SuperB parameters influencing IR design are listed.

Table 2.3: *SuperB parameters that influence the IR design*

	LER	HER
Energy (GeV)	4	7
Beam current (A)	3.95	2.17
N^o of bunches	1733	1733
Bunch spacing(m)	1.26	1.26
β_x^* (mm)	20	20
β_y^* (mm)	0.2	0.2
ϵ_x (nm-rad)	1.6	1.6
ϵ_y (pm-rad)	4	4
Crossing angle (mrad)	34	34

2.2 The Detector

The SuperB detector concept is based on the BABAR detector[4], with some modifications required to operate at a luminosity of 10^{36} cm^{-2} s^{-1} and with a reduced center-of-mass boost[1]. Further improvements needed to cope with higher beam-beam and other beam-related backgrounds, as well as to improve detector hermeticity and performances.

The BABAR detector consisted of a tracking system with a 5 layer double-sided silicon strip vertex tracker (SVT) and 40 layer drift chamber (DCH) inside a magnetic field of 1.5 T, a Cherenkov detector with fused silica bar radiator (DIRC), an electromagnetic calorimeter (EMC) consisting of 6580 CsI(Tl) crystals and an instrumented flux return (IFR) composed of both limited streamer tube (LST) and resistive plate chamber (RPC) detectors for the identification of K_L^0 and μ.

The crucial point is that SuperB detector reuses a number of components from BABAR, for example the flux return steel, the superconducting coil, the barrel of the EMC and the fused silica bars of the DIRC; but some differences occur:

- **Flux return:** additional absorber inserted to increase the number of interaction lengths for muons $\sim 7\lambda$;
- **IFR:** the LSTs and RPCs will be replaced by scintillator bars with photomultipliers (see next chapter);
- **DIRC:** the chamber will be replaced by a 12-fold modular chamber using multi-channel plate (MCP) photon detectors in a focusing configuration using fused silica optics to reduce the impact of beam-related backgrounds and improve performance;
- **forward EMC:** it will consist of cerium-doped LSO (lutetium orthosilicate) or LYSO (lutetium yttrium orthosilicate) crystals, which have a much shorter scintillation time constant, a lower Molière radius and a better radiation hardness.
- **SVT:** a new detector will be built since the BABAR SVT cannot operate at SuperB luminosities. The vertex resolution will be improved by reducing the radius of the beam pipe, placing the innermost edges at a radius of roughly 1.2 cm. This layer

[1]The boost is important to study the dependance of the CP asymmetries from the $\Delta t = t_{CP}$ - t_{tag} in the $\Upsilon(4S) \rightarrow B\overline{B}$, where one of the two B mesons decays into particular CP eingenstates and the other one into a mode whose b-quark flavour can be ascertained (the tag B). Reconstructing B mesons vertices the Δz is related to Δt by the equation $\gamma\beta c\Delta t = \Delta z$. The angular coverage of the detector must be greater than 95.5% in laboratory centre of mass frame and the resolution on the proper time of decay of the B mesons must match or exceed the BABAR value in spite of reducing the Lorentz boost of centre of mass frame.

will be constructed of either silicon striplets or Monolithic Active Pixel Sensors (MAPS) or other pixelated sensors, depending on the estimated occupancy from beam-related backgrounds.

The Fig. 2.7 shows the SuperB detector baseline concept with some optional configurations.

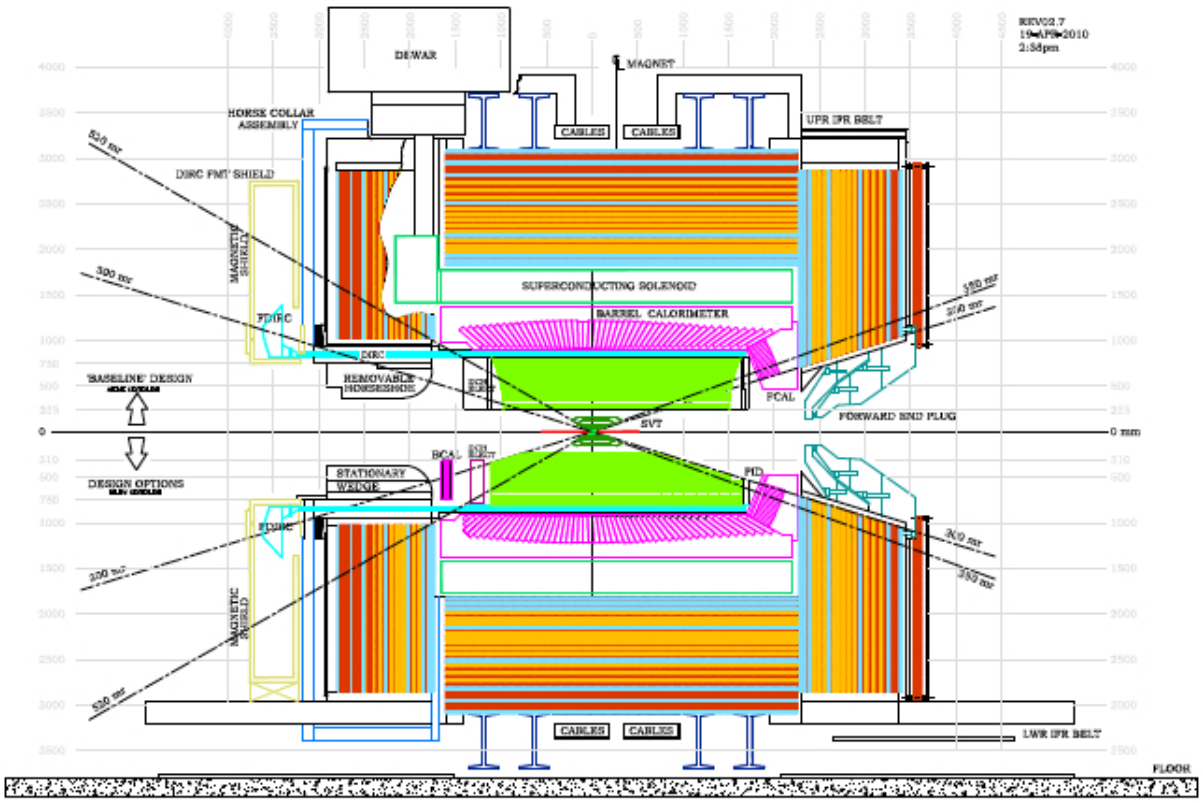

Figure 2.7: *Concept of SuperB detector. The upper half shows the baseline concept, the bottom half optional detector configurations are shown.*

2.2.1 SVT: Silicon Vertex Tracker

As seen previously, the vertex detector provides precise information on both the position and direction of charged particle trajectories as close as possible to the IP. This detector is in fact very important for low momentum particles (<100 MeV/c), because track parameters need to be determined within. In BABAR the average separation along the z coordinate between the vertices was $<\Delta z> \approx 250\ \mu m = \beta\gamma c\tau$ (where $\beta\gamma \sim 0.55$ is the boost value), which implied a precision on Δz distance of the order of 125 μm. The precision of the vertex measurement also determines the ability to distinguish between the signal and background.

Concerning the SuperB detector, the boost value $\beta\gamma$=0.28 which will decrease the average separation along the z coordinate by a factor 2 with respect to the BABAR experiment; in fact SuperB can achieve a resolution of order 60 μm for an optimal CP time-dependent measurements. The innermost layer (Layer 0) will be placed at a radius between 1.2-1.5 cm, detecting the first hit of the tracks as close as possible to the production vertex. There are five additional tracking layers, at radii between 4 and 14 cm. In Fig. 2.8 a longitudinal sections of the SuperB SVT is showed.

Figure 2.8: *Silicon Vertex Tracker views.*

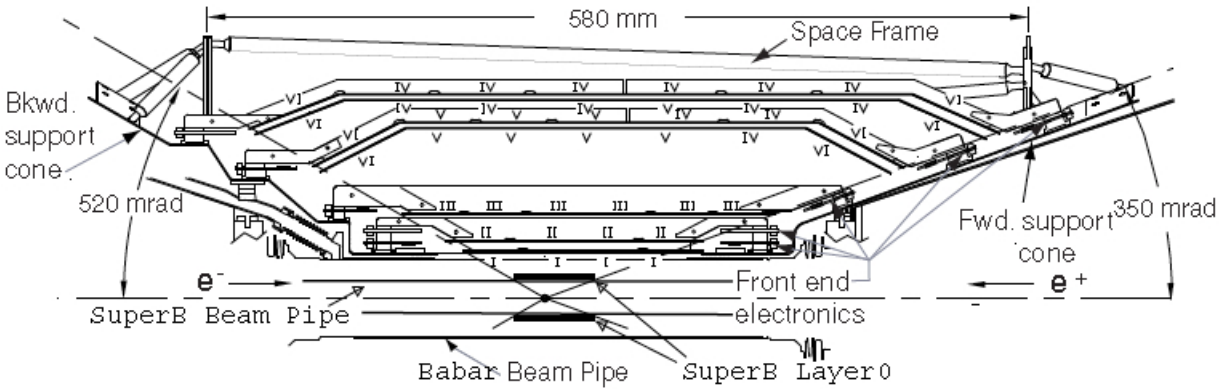

(a) Longitudinal section of the Silicon Vertex Tracker.

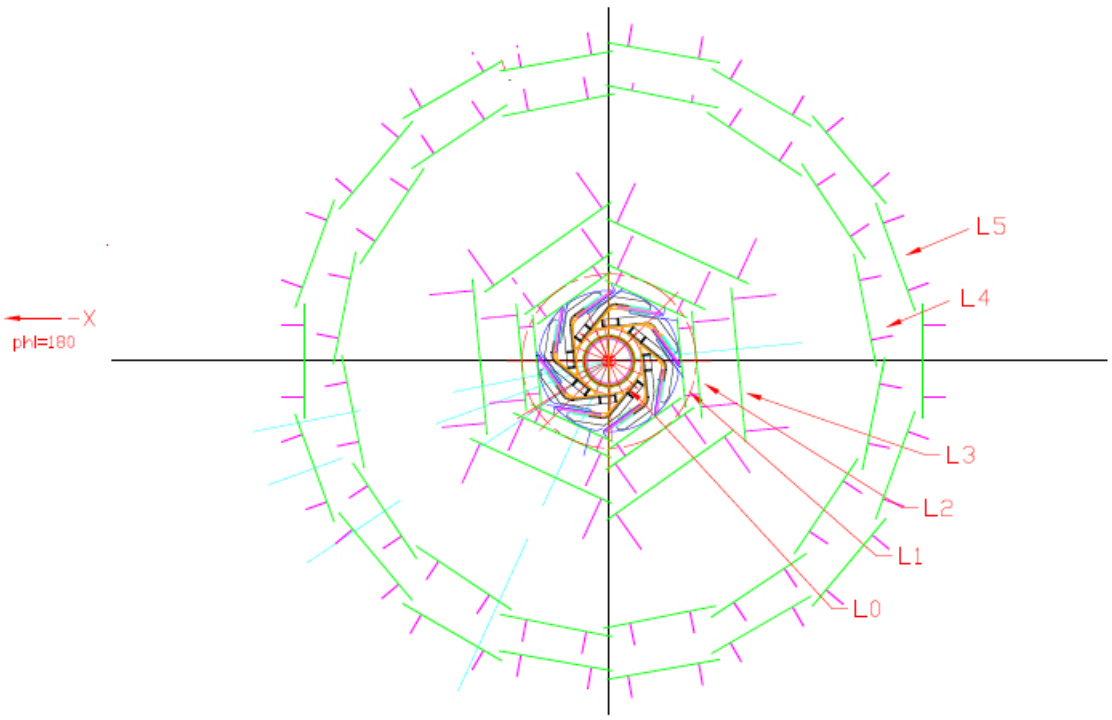

(b) r-ϕ view of the Silicon Vertex Tracker.

The angular acceptance will be 300 mrad in forward and backward directions, cor-

responding to a solid angle coverage of $\sim$ 95% in the centre-of-mass frame. While for the external SVT layers (1-5) the technology adopted is the same as for BABAR, for the Layer-0 sensors three options are being evaluated: striplets[68], CMOS monolithic active pixel sensor (MAPS)[82, 32] and hybrid pixels.

Striplets: these consist of double sided silicon strip detectors 200 μm thick with 50 μm readout pitch (placed at 45° with respect to the detector edges, Fig. 2.9) , that allow a resolution of $\sim$ 10 μm and a reduced material budget of 1% X_0. Each module consists of one silicon sensor, a multilayer printed flexible circuit and two double-sided hybrid circuits, for reading the two halves of the silicon sensor. The signal to noise ratio for a 200 μm detector is about 26, providing a good noise margin; the total amount of material for Layer0 will be about 0.46% X_0 but, if the aluminum microcable technology will be employed, a reduction down to 0.35% X_0 will occur. The crucial point is that the silicon detector fabrication technology will be very similar to that used for the present BABAR SVT sensors, which have proved to be sufficiently radiation hard for the dose expected in the SuperB environment. The silicon sensors will have an active area of 1.29×9.7 cm^2, providing an overlap region between adjacent modules which is useful for alignment of sensors with reconstructed tracks. In Layer0 striplets the occupancy would be of 12% in the 132 ns time window, including a safety factor of 5 and hit rate of 100 MHz/cm^2; the efficiency expected from simulations is 90% or more. Regarding the radiation damage, the SuperB silicon sensors will receive an equivalent fluence of about 6×10^{12} n$_{eq}$/cm^2/yr with a subsequent signal to noise deterioration and a reduction in charge collection efficiency; after five years of operation, the efficiency drop expected is of about 10%[31].

MAPS: starting from the fact the expected Layer0 pixel occupancy is about 0.1% per pixel in 1 μs time window with the five times safety factor included, the pixel technologies adopted from previous experiments are not adequate for this application. A new CMOS MAPS is challenging technology, the advantage is the integration of sensor and readout in a single CMOS layer of $\sim$ 50 μm, reducing the detector material budget to 0.05% X_0 . The MAPS devices use an n-well/p-epitaxial diode to collect, through thermal diffusion, the charge generated by a particle passing through the thin epitaxial layer underneath the readout electronics. Each module will be made of several MAPS chips glued onto a support structure hosting the metal traces for connection to power, command and data lines. The efficiency measured is about 92%, but there are margins to improve the detection efficiency with

Figure 2.9: *Striplets sensor.*

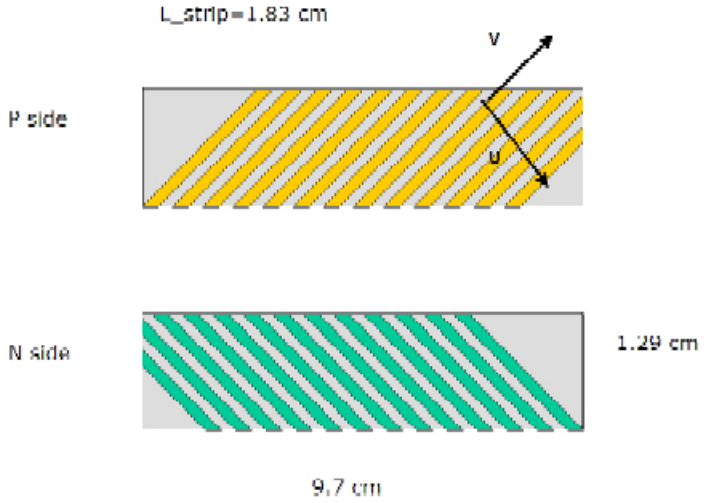

(a) Schematic design of a 45° striplet sensor.

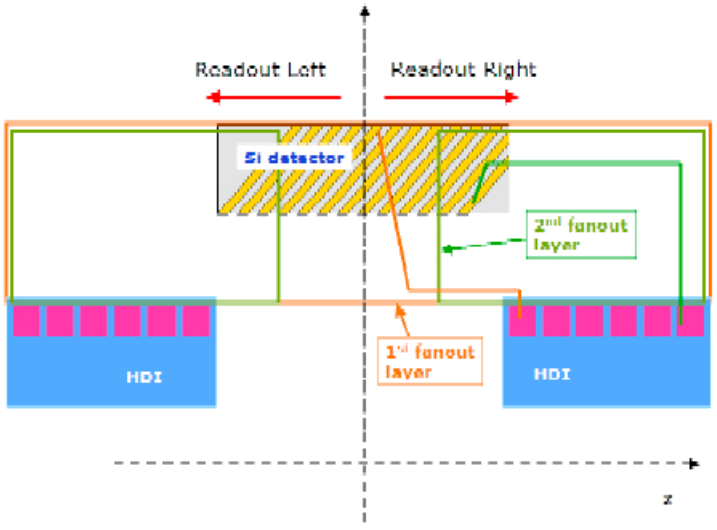

(b) View of a Layer 0 striplet module.

a different sensor layout. For MAPS the radiation hardness requires further investigation, but preliminary tests[89] indicate that this technology can be applied, with modest deterioration, to the SuperB detector. The signal to noise performance can deteriorate in two ways: a reduction in charge collection efficiency and an increase of leakage current of the collecting diode. First results from irradiation with neutrons and protons, show that a fluence of $\sim 10^{12}$ n_{eq}/cm^2 can be tolerated, with a 5% reduction of the collected signal.

Hybrid Pixels: this solution requires some research and development for satisfying the Layer0 requirements. The readout architecture has been developed previously by the SLIM5 Collaboration[46] and has been optimized for the target Layer0 rate of 100 MHz/cm^2.

From simulations it appears that a hit efficiency of 98% is possible, but it is important to note that this solution is still under investigation.

Fig. 2.10 compares errors on $\sin(2\beta)$ for different technologies adopted for SVT Layer0.

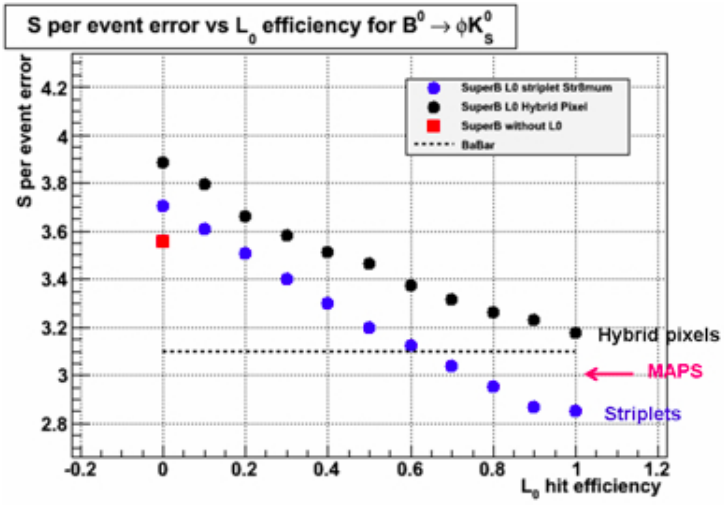

Figure 2.10: $\sin 2\beta$ *per event error as function of the SVT Layer0 efficiency for different technology adopted*

2.2.2 Drift Chamber

The drift chamber (DCH) is the main tracking and momentum-measuring system, providing a good particle identification for low momentum tracks and for tracks in the forward direction. The only detector able to measure particle momenta below approximately 700 MeV/c, the SuperB DCH is based on that of BABAR with a conventional

cylindrical design; the dimensions of this detector are being re-optimized with respect to BABAR since in SuperB the supports connecting the machine elements between SVT and DCH will be removed and the possibility to add a PID device between the DCH and forward/backward calorimeter is being considered.

While the inner radius of the DCH is not determined (it will be as small as possible), the outer radius is constrained to 809 mm by the DIRC (see next paragraph) quartz bars; this detector will be composed by 10000 cell sustaining wire load with carbon-fibre resin composite, offering superior performances respect to BABAR drift chamber (aluminum-alloys).

The baseline design for the drift chamber employs rectangular cells arranged in concentric layers about the axis of the chamber, approximately aligned with the beam direction. The cells, whose dimensions are still to be determined, are expected to have a side between 10 and 20 mm, so these will be ∼40 layers as in BABAR. The cells will be grouped radially into superlayers with the inner and outer superlayers parallel to the chamber axis. Each cell will have one 20 μm diameter gold coated sense wire surrounded by a rectangular grid of eight field wires, all dipped into a gas mixture (80% He - 20%iC_4H_{10}), with an expected gas gain of 5×10^4, that requires a voltage of 2 kV applied to the sense wires. The gas mixture for SuperB should satisfy some requirements: low density, small diffusion coefficient and Lorentz angle, low sensitivity to photons with E $\sim$ 10 keV; in particular it could be useful to choose a mixture with high drift velocity in order to reduce ion collection times and so the probability of hits overlapping from unrelated events.

The SuperB drift chamber is expected to provide momentum measurements with the same precision as BABAR (approximately 0.4% for tracks with a transverse momentum $p_T \sim 1$ GeV/c).

Some studies are still in progress, in particular: precision measurements of fundamental parameters (drift velocity, diffusion coefficient and Lorentz angle) of gas mixtures; study the properties of different gas mixtures an cell layouts with small drift chamber prototypes and simulations; verify the potential and feasibility of the new options *cluster counting*, or a gas with low drift velocity and primary ionization.

The *cluster counting* option can improve the dE/dx resolution by a factor two with respect to the BABAR resolution of 7.5%. This technique involves counting individual clusters of electrons released in the gas ionization process, doing this the sensitivity of the specific energy loss measurement to fluctuations, which significantly limit the intrinsic resolution of dE/dx, in the numbers of electrons produced in each cluster are removed. *Cluster counting* has never been employed in previous experiments, so it requires further investigation. Fig. 2.12 shows the resolution of track momentum for different drift

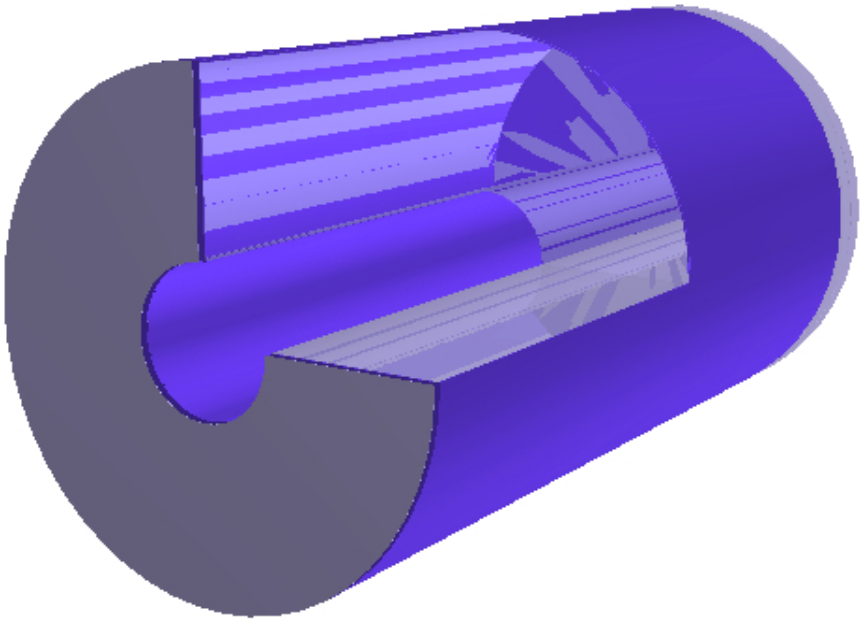

Figure 2.11: *Section of SuperB drift chamber geometry.*

chamber inner radii.

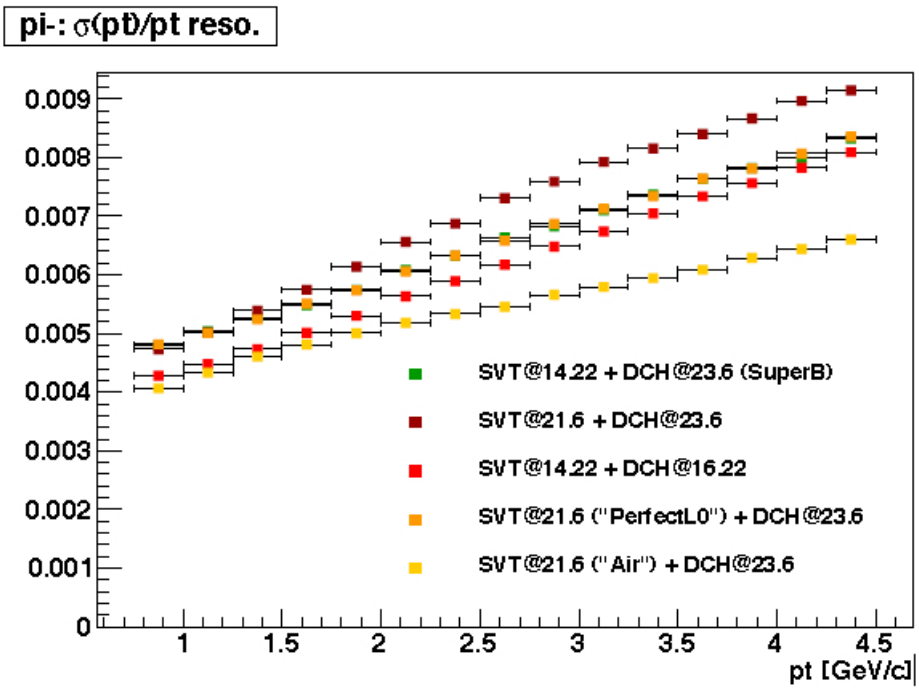

Figure 2.12: *Track momentum resolution for different values of the drift chamber inner radius.*

Concerning the background, the dominant source for the drift chamber will be radiative Bhabha scattering. Photons radiated collinearly to the initial e^+ or e^- direction can bring

the beams off orbit and ultimately produce showers on the machine optic elements. This process can happen meters away from the IP and it can produce hits uniformly distributed in the whole DCH (see Fig. 2.13 for the background photon energy distribution in the drift chamber): using results from simulations an average occupancy of 3.5% is expected (5% in the inner layers) in a 1 μs time window at the nominal luminosity of 10^{36} cm^{2}s^{-1}.

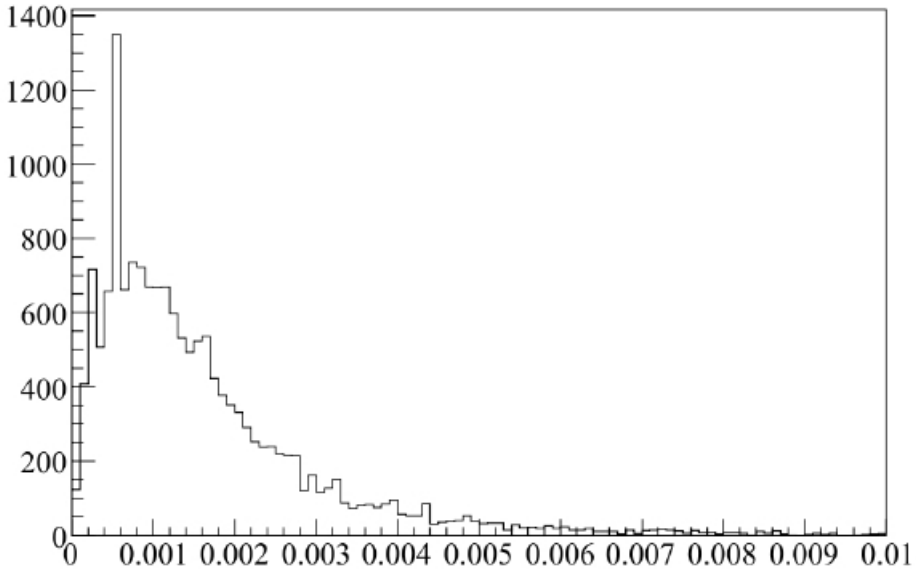

Figure 2.13: *Energy of background photons entering the drift chamber (MeV).*

2.2.3 Detection of Internally Reflected Cherenkov light

The DIRC (Detection of Internally Reflected Cherenkov light) is a system that provides particle identification (PID) and this has to be thin and uniform in terms of radiation lengths, for minimizing the degradation of the calorimeter energy resolution. Given the high luminosity, the PID system needs fast signal response and has to be able to tolerate high backgrounds. The SuperB Cherenkov detector is based on that used in BABAR, but the aim is to improve the performances gaining a factor 100 in background rejection.

The DIRC is based on the principle that the value of the Cherenkov angles are conserved upon reflection from a flat surface; in particular one particle passing trough a material with velocity higher than light velocity in same material, emits a radiation with conic opening angle. The relation between the opening angle, refraction index and the velocity of particle is:

$$\cos\theta_c = \frac{1}{n\beta} \tag{2.9}$$

where θ_c is the Cherenkov angle, n is the refraction index and β=v/c.

The material used for DIRC is fused silica, with n=1.473, in the form of long thin bars and with rectangular section. These bars are also light pipes for that portion of Cherenkov radiation light trapped in the radiator by total internal reflection. The Cherenkov photons are detected by an array of densely packed photomultiplier tubes (PMTs), each surrounded by reflecting light-catcher cones to capture light at a distance of about 1.2 m from the bar end. The expected Cherenkov light pattern at this surface is essentially a conic section, where the cone opening angle is the Cherenkov production angle modified by refraction index at the exit from the fused silica window (see Fig. 2.15(a)).

The photons produced in a bar are then focused onto the phototube detection surface via a "pinhole" defined by the exit aperture of the bar and for associating the photon signals with a passage of a track, the vector pointing from the center of the bar end to the center of each PMT is taken as a measure of the photon propagation angle. Since the track position and angles are known from the tracking system, the three angles can be used to determine the two components of the Cherenkov angles.

For particles with high momenta (above 0.7 GeV/c for pions and hadrons, above 1.3 GeV/c for protons), the DIRC will perform the π/K separation. The basic strategy is to make a detector smaller and faster, than the BABAR DIRC, but maintaining, or better improving, the main performances:

- measured time resolution of about 1.7 ns, close to the PMT transit time spread of 1.5 ns;
- single photon Cherenkov angle resolution of 9.6 mrad for dimuon events;
- Cherenkov angle resolution per track of 2.5 mrad in dimuon events;
- K/π separation above 2.5 σ for the pion Cherenkov threshold up to 4.2 GeV/c.

With respect to the BABAR, the reduced volume of the new chamber and the use of fused silica for coupling to the bar boxes can reduce the sensitivity to the background by an order of magnitude. The very fast timing PMT's provide additional improvements: better Cherenkov resolution, a measure of the chromatic dispersion in the radiator[87, 28, 29], separation of ambiguous solutions in the folded optical system and another order of magnitude background rejection.

The focusing DIRC (FDIRC) consists of two parts: a focusing block (FBLOCK) with cylindrical and flat mirror surfaces and new wedge, which rotates rays with large transverse angles (in the focusing plane) before they merge into the focusing structure. The crucial point is that the cylindrical mirror is appropriately rotated to make sure that all rays

Figure 2.14: *DIRC detector.*

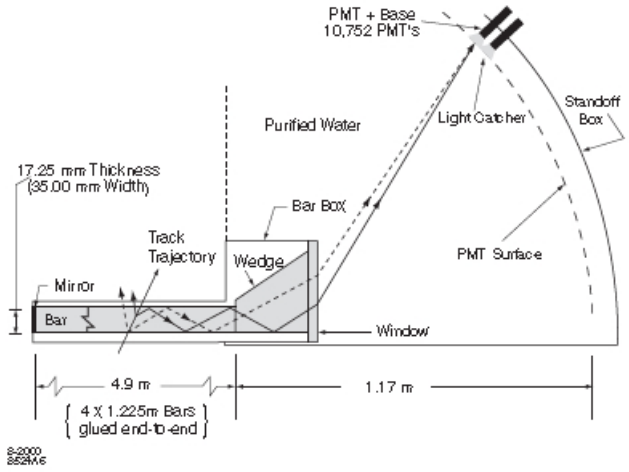

(a) Schematic of the DIRC fused silica radiator bar and imaging region.

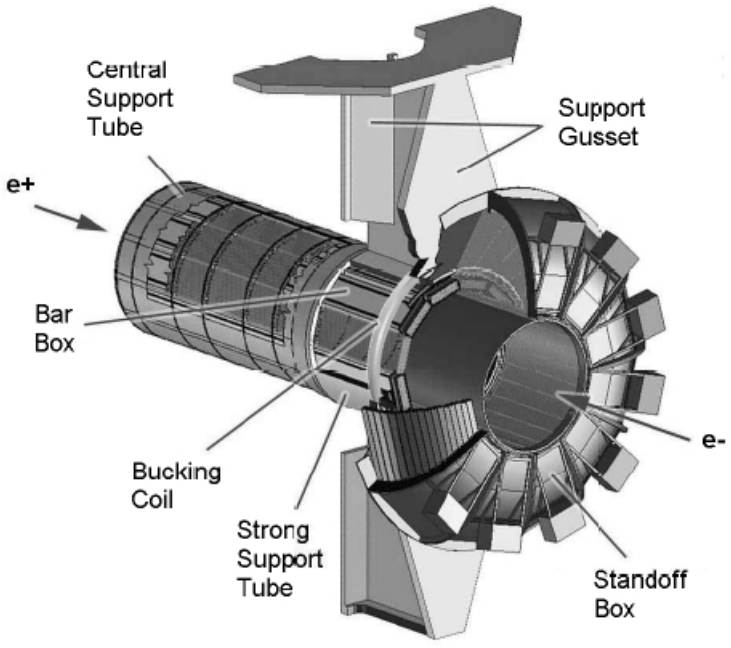

(b) Schematic view of the SuperB DIRC.

reflect onto the FBLOCK flat mirror (this reflects rays onto the detector focal plane with an incidence angle of almost 90°), preventing reflections back into the bar box itself.

Figure 2.15: *GEANT4 DIRC detector.*

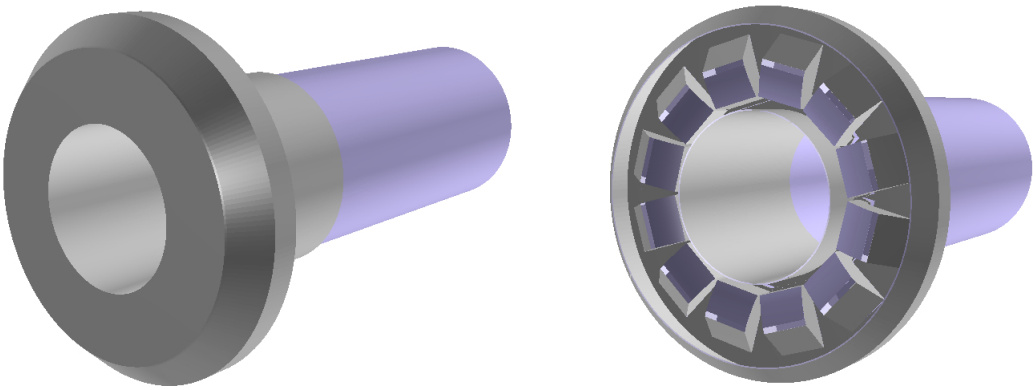

(a) GEANT4 DIRC detector view.

(b) Detail of fused silica in GEANT4 DIRC description.

Forward Particle Identification

Through the FDIRC detector combined with the dE/dx from the drift chamber, it will be possible to have a good π/K separation up to 4 GeV/c; hadron identification in the forward and backward regions will be limited unless a dedicated PID detector is foreseen. This device needs to cover the π/K ambiguity region for the dE/dx near 1 GeV/c, and should provide a high momentum π/K separation where the dE/dx separation is rather poor.

This detector is under study and the possible options are: DIRC-like time of flight, a "pixelated" time of light and a Focusing Aerogel RICH (FARICH).

DIRC-like time of flight: charged tracks cross a thin layer of quartz in which Cherenkov photons are emitted along the particle trajectories, so they are transported through internal reflections to PMTs. This device must be very precise, it can be fit without problems into the available space between the DCH and electromagnetic calorimeter (EMC).

"pixelated" time of flight: in this option Cherenkov light is also produced in a quartz radiator[88], made of quartz cubes which couple directly onto matching pixelated photodetectors that cover the entire detector surface: the reconstruction is much easier because a given track will produce light in a particular pixel (whose location would be predicted by the tracking algorithms). The advantages of this options are the low sensitivity to background and the insensitivity to chromatic time broadening.

FARICH: uses a 3-layer aerogel radiator, with focusing effect for high momentum separation, and a water radiator, for low momentum region[84]; this type of detector has the best PID performance at high momentum.

2.2.4 Electromagnetic calorimeter

The SuperB electromagnetic calorimeter provides energy and direction measurement of photons and electrons, being an important component in the identification of electrons versus the charged particles. This detector (see Fig. 2.16) is a cylindrical array of scintillating crystals, divided in three parts:

- **Barrel calorimeter:** will be reused from BABAR, it consists of 5760 CsI(Tl) crystals and covers 2π in azimuth and polar angles from 28° to 141.8° in the lab. There will be 48 rings of crystals in polar angles, with 120 crystals in each azimuthal ring.

- **Forward endcap calorimeter:** this one will replace the forward endcap of the BABAR forward calorimeter, with coverage starting from the end of barrel and extending down to 270 mrad ($\cos\theta$=0.965) in the laboratory. The increased background level needs to have a faster and more radiation hard material, so the forward calorimeter will use pure CsI or LYSO(Lutetium Yttrium Orthosilicate). The advantage of the latter is the much shorter time scintillating constant (40 ns with respect to 680 ns of CsI) and a smaller Molière radius (2.1 cm compared to 3.6 cm of CsI).

  The forward calorimeter will consist of 20 rings of crystals arranged in four groups of 5 layers each; each crystal is up to 2.5 × 2.5 cm^2 at the back end, with a projective taper to the front; the length of the crystals is approximately 20 cm.

- **Backward calorimeter:** the backward calorimeter is a new device with the principal aim of improving the hermeticity, with a modest cost. A multi-layer lead-scintillator sandwich has been proposed with a stack longitudinal segmentation providing a capability to select π/e. In order to provide transverse spatial shower measurement, each layer of scintillator is segmented into strips among three different patterns for different layers: right-handed logarithmic spiral, left-handed logarithmic spiral and radial wedge; this set of patterns is repeated eight times to make a total of 24 layers. The backward calorimeter covers the region from 150° to 167°.

For BABAR the energy resolution was:

$$\frac{\sigma_E}{E} = \frac{2.30\%}{\sqrt[4]{E(GeV)}} \oplus 1.35\% \qquad \sigma_\theta = \frac{4mrad}{\sqrt{E(GeV)}} \tag{2.10}$$

which can be improved with new type of electromagnetic calorimeter in SuperB detector.

Calorimeter background, arising from beam and luminosity effects, impacts calorimeter performance in several ways. The crucial effect is the deposition of energy into the crystals which exceeds the effective threshold for reconstruction a cluster, or for the inclusion of the crystal energy into an adjacent cluster arising from physics sources.

In the first case a production of spurious neutral clusters results, which degrade the resolution of energy reconstruction; in the second case, the increased occupancy degrades the cluster energy resolution and can negatively impact the cluster reconstruction performance.

Concerning the radiation damage, the CsI(Tl) can create color centers in the crystals, resulting in a degradation of response uniformity and light yield. Pure CsI and LYSO are more radiation hard and the dominant contribution to the dose arises from luminosity and single-beam background sources and neutrons. Further studies are needed to estimate the background rate and the possibility to shield electromagnetic calorimeter.

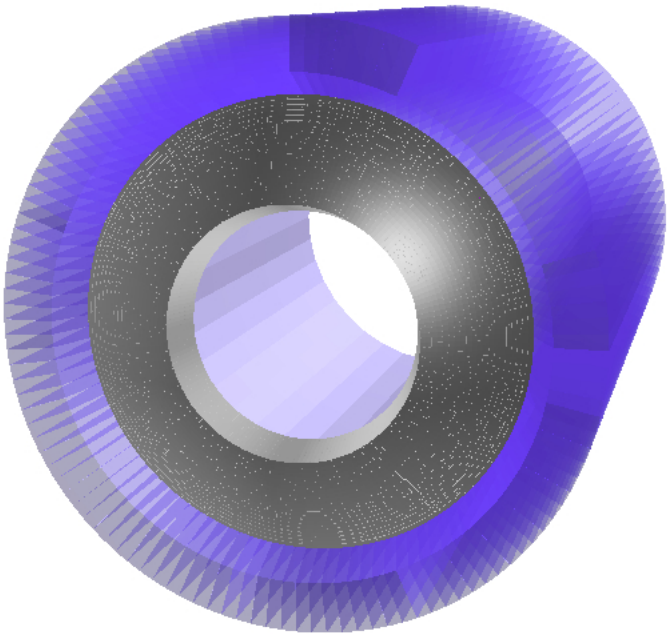

Figure 2.16: *GEANT4 geometry description of the EMC, in grey the forward calorimeter.*

2.2.5 Instrumented Flux Return

A muon identification system must have high efficiency for selecting penetrating particles as muons but, at same time, it must to reject charged hadrons, such as pions and kaons. Since the development of the muon detector is the subject of this thesis, it will be discussed in detail in the next dedicated chapter.

Chapter 3

The Instrumented Flux Return project

The Instrumented Flux Return (IFR) is designed primarily to identify muons, and, in conjunction with the electromagnetic calorimeter, to identify neutral hadrons, such as K_L^0. This chapter describes the performance requirements and a baseline design for the IFR.

The iron yoke of the detector magnet provides the large amount of material needed to absorb hadrons. The yoke, as in the BABAR detector, is segmented in depth, with large area particle detectors inserted in the gaps between segments, allowing the depth of penetration to be measured. In the SuperB environment, the critical regions for the backgrounds are the small polar angle sections of the endcaps and the edges of the barrel internal layers, where we estimate that in the hottest regions the rate is a few 100 Hz/cm^2. These rates are too high for gaseous detectors. While the BABAR experience with both RPC's and LST's has been, in the end, positive, detectors with high rate characteristics are required in the high background regions of SuperB. A scintillator-based system provides much higher rate capability than the gaseous detectors: for this reason, the baseline technology choice for the SuperB detector is extruded plastic scintillator using Wave Length Shifter (WLS) fibre read out with avalanche photodiode pixels operated in Geiger mode.

The IFR system must have high efficiency for selecting penetrating particles such as muons, while at the same time rejecting charged hadrons (mostly pions and kaons). Such a system is critical in separating signal events in $b \to sl^+l^-$ and $b \to l^+l^-$ processes from background events originating from random combinations of the much more copious hadrons. Positive identification of muons with high efficiency is also important in decays such as $B \to \tau\nu_\tau(\gamma)$, $B \to \mu\nu_\mu(\gamma)$ and $B_d(B_s) \to \mu^+\mu^-$ and in search for lepton flavour-violating processes such as $\tau \to \mu\gamma$. Background suppression in reconstruction of final states with missing energy carried by neutrinos (as in $B \to \mu\nu_\mu\gamma$) can profit from vetoing

the presence of energy carried by neutral hadrons. In the BABAR detector, about 45% of relatively high momentum K_L^0's interacted only in the IFR system. A K_L^0 identification capability is therefore required.

3.1 Structure of the detector

The IFR detector is composed by three main sections:

- **barrel**, with cylindrical symmetry around the beam pipe;
- **forward endcap**, the forward detector;
- **backward endcap**, the backward detector.

Figure 3.1: *Views of IFR system*

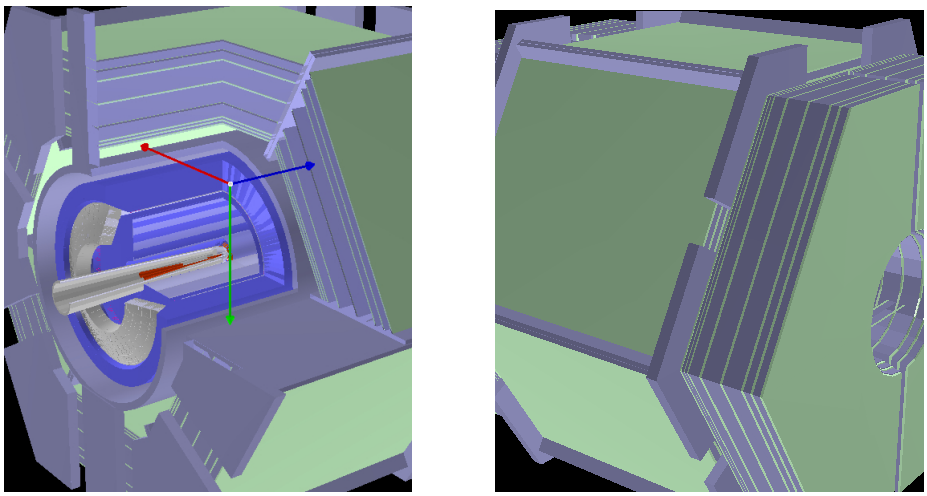

(a) View of internal detectors and IFR iron segmentation.

(b) View of barrel and endcap section.

This system is the outer region of the SuperB project and is dipped into a magnetic field with an intensity of 1.5 T, and all the IFR is closed into a hexagonal iron yoke. While endcaps are divided into two parts (left and right), the barrel is subdivided into six different sections called sextants. The geometry configuration of the barrel region and the endcaps region is the same: 8 active layers of scintillator with 7 iron gaps of different thickness. The IFR system is a sequence of a scintillator layers (thickness 2 cm), gap of air (0.5 cm) and iron layer of different thickness. One possible segmentation of the iron is shown in Fig. 3.2.

Table 3.1: *Detailed longitudinal segmentation of one sextant.*

Number of gap	Material	thickness
1	scintillator	2cm
	air	0.5cm
	iron	2 cm
2	scintillator	2cm
	air	0.5cm
	iron	2cm
3	scintillator	2cm
	air	0.5cm
	iron	16cm
4	scintillator	2cm
	air	0.5cm
	iron	26cm
5	scintillator	2cm
	air	0.5cm
	iron	26cm
6	scintillator	2cm
	air	0.5cm
	iron	10cm
7	scintillator	2cm
	air	0.5cm
	iron	10cm
8	scintillator	2cm

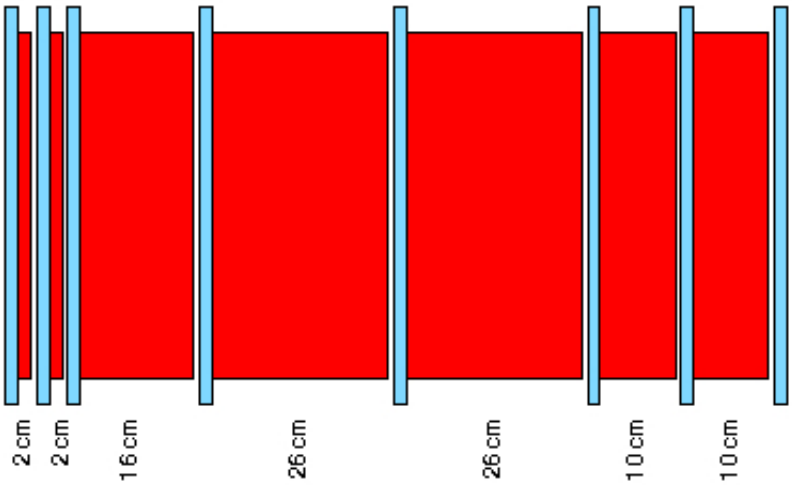

Figure 3.2: *Longitudinal segmentation of the iron absorber (red) and in the baseline configuration. The active detectors are in light blue, the innermost at left and the outermost at right.*

This stratigraphy (Tab. 3.1) is a longitudinal segmentation of each sextants and endcaps; in the baseline geometry description the total amount of iron is 920 mm (in the next chapters other geometry configurations will be shown) .

3.1.1 Physics and geometry requirements

Muons are identified by measuring their penetration depth in the iron of the return yoke of the solenoid magnet. Hadrons shower in the iron, which has a hadronic interaction length $\lambda_I = 16.5$ cm[55]. So the survival probability to a depth d scales as e^{-d/λ_I}.

One of the aims of this detector is to avoid the misidentification between muons and hadrons (in particular pions) decay in flight. To identify muons with momenta below 1 GeV/c is difficult, due to ranging out of the charged track in the absorber. Moreover, only muons with high transverse momenta can penetrate in the IFR system to sufficient depth for the identification.

On the other side, neutral hadrons interact in the electromagnetic calorimeter as well as in the flux return; the K_L^0 tends to interact in the inner section of absorber, so its identification depends on the energy deposited in the inner active layers, hence the segmentation needed at the beginning of iron stack.

The best performance can be obtained combining the shower in the electromagnetic calorimeter with the rear part in the inner portion of the IFR.

In BABAR the total amount of material in the flux return (about 5 interaction lengths at normal incidence in the barrel region including the inner detectors) is suboptimal for μ identification[56].

Adding iron with respect to the BABAR flux return for the upgrade to the SuperB detector can produce an increase in the pion rejection rate at a given muon identification efficiency. One of the goals of the simulation studies is to understand if the BABAR iron structure can be upgraded to match the SuperB muon detector requirements. Fig. 3.2 represents the baseline geometry configuration, but the final steel segmentation will be chosen on the basis of Monte Carlo simulations on muon penetration and charged/neutral hadron interactions.

3.1.2 R&D

The R&D involves different aspects of a detector. For what concerns the IFR system, there are three principal details to implement:

- scintillators;
- fibres;
- photodetectors.

In the previous paragraphs it has been showed that the choice to use a scintillator was made due to the fact that the background rate is high. In the iron gap of the IFR system there will be placed three fibres within a scintillator for the signal to the photodetectors (Fig. 3.3).

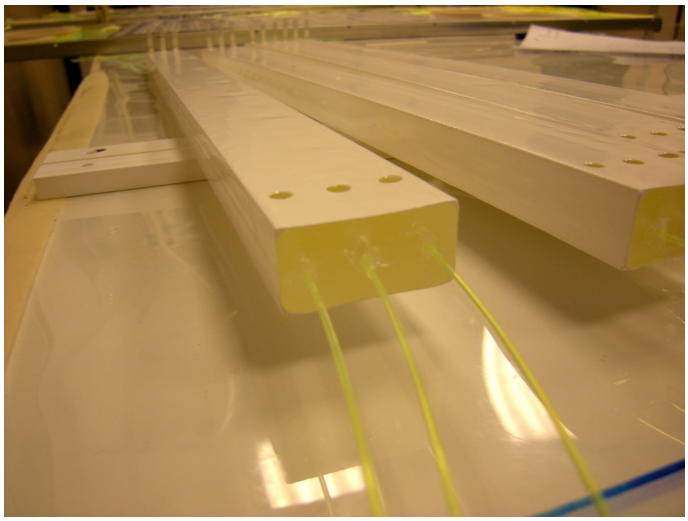

Figure 3.3: *Prototype layout for a scintillator*

In the next sections each part of the active layers system for reconstructing an event will be described.

Scintillators

Main requirements for the scintillator are a good light yield and a fast response. Both these requirements depend on the scintillator material characteristics and on the geometry adopted for the bar layout. Since more than 20 Metric Tons of scintillator will be used in the final detector, another major constraint is the cost that should be minimized. We found the extruded scintillator produced by the FNAL-NICADD facility (used also in the MINOS experiment [44]) suitable for our detector. Given the foreseen space constraints, (the gaps between two iron absorbers are roughly 25 mm), the bar thickness shouldn't exceed 20 mm. The bar width is 4 cm and the fibres are placed in 3 holes extruded with the scintillator. We have two possible layouts for the bar:

1. 1 cm thick, to put inside a gap two separate detection layers.

2. 2 cm thick, in this case the gap is filled with only one bigger active layer.

The two scintillator layouts have been used to study two different readout options: a Time readout and a Binary readout (Fig. 3.4).

Figure 3.4: *Scintillator layouts*

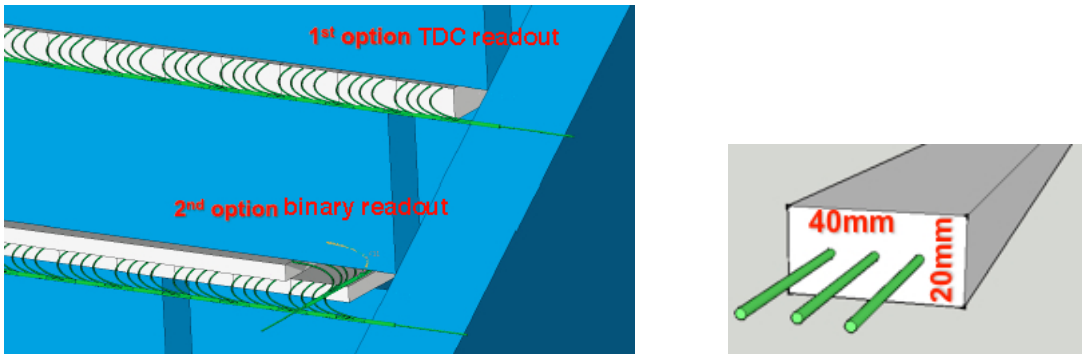

(a) The two different readout options

(b) Scintillators model.

In the Time readout, one coordinate is determined by the scintillator position and the other by arrival time of the signal read with a TDC. In this case both coordinates will be measured by the same scintillator bar (that is 2 cm thick) so there is no ambiguity in case of multiple tracks, but the resolution of one coordinate is limited by the time resolution of our system that is about 1 ns.

In the Binary readout option, the track is detected by two orthogonal 1-cm-thick scintillator bars. The spatial resolution is driven by the width of the bars (that is 4 cm as for the Time readout), but in case of multiple tracks a combinatorial association of the hits must be done.

Wave Length Shifter fibres

As shown in the introduction, the fibres need to have a good light yield, in order to ensure a high detection efficiency and a time response fast enough to allow a $\simeq$ 1 ns time resolution. WLS (wave length shifter) fibres from Saint-Gobain (BCF92) and from Kuraray have been tested [49, 71].

Both companies produce multi-clad fibres with a good attenuation length ($\lambda \simeq 3.5$ m) and trapping efficiency ($\epsilon \simeq 5\%$) but Kuraray fibres have a higher light yield while Saint-Gobain have a faster response ($\tau = 2.7$ ns, while the Kuraray $\tau = 9.0$ ns).

Tab. 3.2 shows the comparison between the two types of fibres.

Table 3.2: *Comparison Kuraray and Bicron fibres*

Physics parameter	Kuraray Y11-175 ϕ=1.2mm	Bicron BCF-92 ϕ=1mm and 1.2mm
Trapping efficiency	5.4%	5.6%
Attenuation length	∼3.5m	∼ 3.5m
Emission peak	476nm	492nm
Decay time	∼10ns	∼2.7ns

While the Kuraray fibre has a better light yield, worste time resolution and is good for binary readout, the Bicron one has a better time resolution, a worste light yield and is good for Time to Digital Converter (TDC) readout.

Photodetectors

Recently developed devices, called Geiger Mode APDs[1], suit rather well our needs of converting the light signal in a tight space and high magnetic field environment. These devices have high gain ($\simeq 10^5$), fast response ($\simeq$ 200 ps) and a good detection efficiency ($\approx$ 30%). The peculiarity of these is the small dimension and the capability to be insensitive to magnetic fields. On the other hand, they have a high dark count rate (= 1 MHz/mm^2@1.5 p.e) and are sensible to radiation.

Two of this devices, one produced by IRST-FBK[53] (SiPM (Silicon Photo Multipliers) 1×1 mm^2) and MPPC by Hamamatsu[48] respectively, have been tested. The comparison between SiPMs and MPPCs showed a lower detection efficiency of the former but also a faster response and a less critical dependence from temperature and bias voltage. For

[1] Avalanche photodiode (APD) is a highly sensitive semiconductor device that exploits the photoelectric effect to convert light to electricity. This device can be thought of as a photodetectors that provide a built-in first stage of gain through avalanche multiplication. APDs that works in high gain range (10^5 to 10^6) are operating in regime called Geiger mode.

coupling one photodetector with four fibres with ϕ =1.0 mm, FBK SiPM 2×2 mm^2 and Hamamatsu 3×3 mm^2, have been tested but the last was too noisy for our purpose, so as baseline we are considering the SiPM.

Figure 3.5: *SiPM layouts*

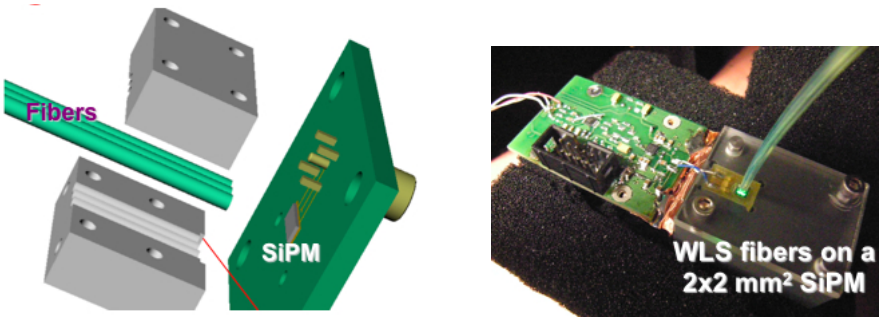

(a) View of possible connection between fibres and SiPM.

(b) Example of SiPM-fibre connection.

3.1.3 Tests and results

R&D studies were performed using cosmic rays, with all the setup inside a "dark box", 4 m long, for keeping scintillators, fibres and photodetectors in a lighttight volume. Because the SiPM are sensitive to radiation, the possibility to keep them outside the detector, in a low radiation area and bringing the light signal to the photodetectors through 10m of clear fibres, has been studied.

For recovering the lost light, we tried to use more than one fibre per scintillator bar: in Fig. 3.6 there is the comparison between the collected charge with 1,2 and 3 WLS fibres using a SiPM 2×2 mm^2.

Obviously with 3 fibres there is a recovery of charge with a factor 1.65, with 4 fibres there is only an increment of 10%, not enough for our purposes. The light loss is too high to bring the photodetector out of the iron therefore we have to couple the SiPM to the WLS fibres inside the detector, at the end of the scintillator bars and to shield them properly.

A systematic study has then been performed with the photodetectors directly coupled to the WLS fibres. The detection efficiency ϵ and the time resolution σ_T have been measured in critical points. The goal is to have a detection efficiency $\epsilon > 95\%$ and, for the Time readout only, a time resolution $\sigma_T \simeq 1$ ns (this is equivalent to have a spatial resolution along the longitudinal coordinate $\sigma_Z \simeq 20$ cm). Tab. 3.3 shows results collected for each readout solution, and for options with 2 or 3 fibres; in order to have a safety margin, is convenient to place at minimum of 3 fibres into the scintillator bar.

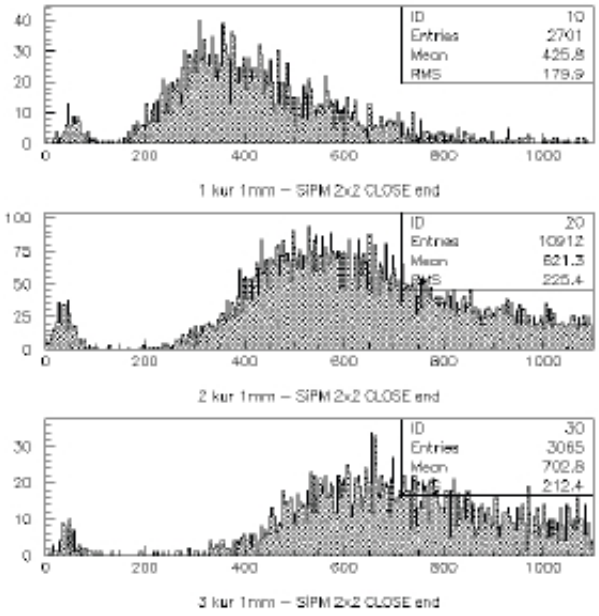

Figure 3.6: *Charge collected with 1,2 and 3 WLS fibres.*

Table 3.3: *Summary of measurements with Time and Binary readout.*

Time Readout						
	Time resolution (ns)			Detection efficiency (%)		
2 fibres	1.5 p.e	2.5 p.e	3.5 p.e	1.5 p.e	2.5 p.e	3.5 p.e
0.3 m	0.91	0.95	-	95.4	98.6	-
2.2 m	1.38	1.44	-	95.9	96.5	-
3 fibres	1.5 p.e	2.5 p.e	3.5 p.e	1.5 p.e	2.5 p.e	3.5 p.e
0.3 m	0.89	0.91	0.97	94.2	98.9	99.4
2.2 m	1.16	1.17	1.26	95.9	99.1	99.1
Binary Readout						
	Time resolution (ns)			Detection efficiency (%)		
2 fibres	1.5 p.e	2.5 p.e	3.5 p.e	1.5 p.e	2.5 p.e	3.5 p.e
2.4 m	1.87	2.16	2.14	98.8	97.4	91.6
3 fibres	1.5 p.e	2.5 p.e	3.5 p.e	1.5 p.e	2.5 p.e	3.5 p.e
2.4 m	1.60	1.65	1.76	98.7	99.2	98.5

An important test with radiation has been conducted with the neutron facility of ENEA in Frascati. First results show that radiation effects start from an integrated dose of 10^8 neutrons/cm^2 and remain rather stable up to a dose $\simeq 7\times10^{10}$ neutrons/cm^2; in this range, the irradiated SiPMs continue to work with lower efficiency and higher dark rate.

3.2 The prototype idea and baseline detector design

The prototype is composed by a full stack of iron with segmentation that allows the study of different geometry configurations. Within the gaps of iron there will be placed scintillators (the active area is 60×60 cm^2) with their WLS fibres and photodetectors, enclosed by light-tightened boxes.

Figure 3.7: *Prototype's mechanics*

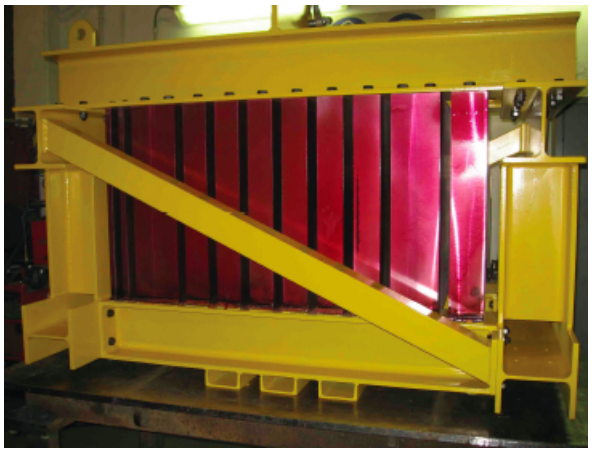

(a) View of prototype's mechanics.

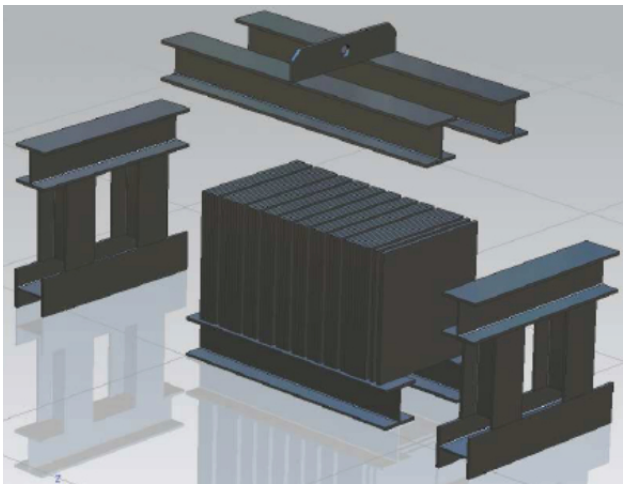

(b) Mechanics design.

The mechanics of the prototype (Fig. 6.1) allows the possibility to study different amounts of iron thickness and different placements of scintillators layers. The segmentation of the prototype (Tab. 3.4) allows to test easily some interesting different configurations:

- with more or less iron;
- with more active layers (useful for K_L^0 identification) ;
- with different spacings between layers;
- changing the granularity.

The idea is to test the prototype with 8 active layers, 4 having Binary readout and 4 with Time readout, with muons/pions beam with momentum between 0.5 GeV/c and 5 GeV/c produced at Fermilab. In addition to measuring the muon identification capability with different geometry configurations, the aim of the test is to estimate the detections efficiency and spatial resolution too.

Table 3.4: *Detailed longitudinal segmentation of prototype.*

Number of gap	iron thickness
1	2 cm
2	2 cm
3	16 cm
4	8 cm
5	8 cm
6	8 cm
7	8 cm
8	8 cm
9	8 cm
10	14 cm
11	10 cm

3.2.1 Baseline design detector

The final detector design will take into account different constraints from R&D studies, simulation results and the experience with BABAR detector. Two configurations of readout have pros and cons from performance point of view but both match with SuperB

requirements, the Binary readout installation will be more complicated, due to the limited access to the gaps.

The main idea is to instrument the barrel region with time readout, reading the scintillator bars with photodetectors at both ends, and endcaps with binary readout reading the bars only on one side. On the other hand, it is important to note that the endcaps region at low radii will be subjected to high radiation, and it is not a suitable place for photodetectors.

For what concerns the flux return, the baseline idea is to reuse the BABAR flux return with some mechanical modifications. In BABAR the primary thickness was 650 mm in the barrel region and 600 mm in the endcaps, but for improving the muon identification the thickness was then increased up to 780 mm in the Barrel and up to 840 mm in forward endcap, replacing some active layers with brass.

For the SuperB baseline design the total thickness of iron is 920 mm, corresponding to 5.5 interaction lengths. This can be achieved both by filling more gaps with metal plates or by recovering a 100 mm steel thickness in the barrel which is not used in BABAR. One important change with respect to the BABAR IFR is the increased weight of active layers, that involves a general reinforcement of the support elements.

3.3 Detector studies: the full simulation

The full simulation is very essential for background studies, detector optimization and for extracting parameters for fast simulation. While the fast simulation has a description of detector simplified, the full one has a detailed description of the detector and gives us informations about physics processes during the passage of particles.

After having studied a background rate at the subdetectors, it is possible to modify the design of the detector for obtaining optimal performance. Results from full simulation can be used to improve results of the fast simulation: the design of the interaction region (IR) has a deep influence on the background rates, so simulating a complex design of the IR is beyond the purpose of fast simulation. On the other hand full simulation might be too slow to have high statistics needed for signal events.

For full simulation a tool based on GEANT4, called Bruno, has been developed with some important features:

Geometry description For reusing the previous geometry description of BABAR, the Geometry Description Markup Language (GDML) has been chosen due to the availability of native interfaces in GEANT4 and ROOT and the ease of human inspection and editing provided by the XML-based structure.

Inputs: event generators Bruno can be interfaced to an event generator in two ways: either by direct embedding of the generator code or by using an intermediate exchange format.

Outputs: hits and Monte Carlo Truth Hits from different detectors, which represent the simulated events, are saved in the output (ROOT) file for further processing. Also the MonteCarlo Truth (MCTruth), intended as a summary of the event as seen by the simulation engine itself, i.e. with full detail, is saved and can be exploited in Bruno in several useful ways, the most important being the estimation of the particle fluxes at sub-detector boundaries by means of full snapshots taken at different scoring volumes.

Staged simulation In particular in the design phase, a very frequent use-case will be the one in which a detector modifies its layout and wants to use full simulation to better evaluate the effect of the change. This would normally trigger the need of productions of large set of events which, with all sub-detectors working in parallel, may lead to a large and inefficient use of computing resources. In Bruno this potential risk is mitigated by the implementation of staged simulation, where snapshots of particles taken at a specific detector boundaries, can be read back and used to start a new simulation process without the need of retracking particles through sub-detectors that sit at inner positions.

Starting from the Bruno tool, some different studies, are been conducted for evaluating the performance of the SuperB Instrumented Flux Return. It is possible to classify these studies into two different branches:

1. background studies: neutrons, gammas and electron/positron.

2. optimization studies: efficiency, geometry configurations, muon selection, physics list, hadronic showers and noise on detector;

The first ones are very important for understanding the background rate of different particles in the IFR system, in particular the neutron rate: this is crucial for evaluating the damage on photodetectors that are very sensible to the impact of neutrons. More attention has been dedicated to study the neutron rate distribution in the IFR detector, for searching the hot regions and understanding where to place photodetectors.

Studies on optimization of detector, are key for determining the best geometry configurations for having best detector performace. For example the iron thickness has been

modified for evaluating the influence on the muons identification and pions rejection, different physics lists have been studied for studying repercussions on physics quantities and so on.

All these studies will be discussed in next chapters.

Chapter 4

Background studies on the IFR

Considerations regarding background influence several aspects of the detector design: readout segmentation, electronic shaping time, data transmission rate, triggering and radiation hardness. With a correct collider design, a first source of background is the beam-beam interaction, radiative Bhabha production and Touschek scattering; photons from synchrotron radiation and lost beam particles give smaller contributions. These sources give rise to primary particles that can either hit the detector directly, or generate secondary particles shooting the detector.

In the next paragraph we will examine the different background sources, but for IFR detectors we will concentrate out attention to the neutron background. This is vital for evaluating the life-time of photodetectors placed at both ends of scintillator bars.

4.1 Types of background

As seen, there are several sources of background that can produce noise all the detector. In this section a brief description of the different sources will be done.

Beam-beam interaction The *SuperB* design produces its high luminosity by employing a reduced beam size having a high bunch charge density. There is thus a strong beam-beam interaction and the intrabeam scattering too, which, in the SuperB environment, are the dominant background sources. The first one is studied by using the Guinea Pig package [83]. The photon emission is parameterized as an interaction between $e^{\pm}$ and the collective beam-beam field, plus a component of photon emission in the collision of individual particles [90]. The e^+e^- pair production is determined not only by a low-energy electron and positron co-moving with the beams and strongly deflected by the beam-beam field, but also trough the second.order

QED process of pair creation during the collision. This effect, at the SuperB energy, is essentially a mixture of an incoherent amplitude given by the interaction of individual particles [74] and a coherent process in which the emitted photon interacts with the collective field of the oncoming bunch [78]. These processes are generated in Guinea Pig and the photons and charged particles produced in the interaction are then passed to a GEANT4 simulation to model the detector response. The expected hit rates from this type of background are expected to be small in all subdetectors except the silicon tracker.

Radiative Bhabhas The effect of particles scattered in radiative Bhabha processes is studied starting from the BB-BREM generator[69], a MonteCarlo program which simulates $e^+e^- \rightarrow e^+e^-\gamma$, in the very forward direction. An experimental cut is imposed on the energy loss by the primary lepton, the secondaries are then propagated trough the GEANT4 detector simulation, and the hit rates are studied. Due to the dynamics of the process, the impact of this background source is present in all detectors.

Touschek Scattering The Touschek scattering rate scales with the bunch charge density, hence it is expected to be way higher than in present B factories. Simulation studies for background due to Touschek scattering have been performed for the LER. The expected loss rate without collimators or any other adjustment of the ring mechanical apertures is 2.3 MHz within 4 m from the interaction point (IP) for a single LER bunch (I =1.3 mA.)

Introducing three horizontal collimators far away from the detector at z = -117 m, z = -65 m and z = -40 m, the Touschek losses inside the detector are reduced by a factor 25. The remaining Touschek loss rate inside the detector is 90 KHz per single LER bunch; these particles are principally scattered at z$\approx$ -31m eventually hitting the beam pipe near the IP and producing high multiplicity electromagnetic showers.

For reducing these effects a study of several final focus parameters is needed: the phase advance between positions where Touschek scattering occurs and the IP, the mechanical aperture of the vacuum chambers upstream of the IP, the insertion of additional collimators and masks near the final doublet.

Other sources Lost beam particles are a source of background proportional to single beam currents. Electrons or positrons circulating in the beam pipe lose momentum through Coulomb or bremsstrahlung interactions with residual gas molecules. These

interactions are more serious in regions of the ring far from the interaction region, where the pressure is high; so these particles can reach the interaction region, where they can be bent by the final focus elements hitting the detector.

An estimate of these lost particles background has been done extrapolating data from studies made at BABAR [36], where this is one of the dominant sources of background. For what concerns PEP-II, the rate of lost beam particles hitting the detectors was estimated to be less than 1 MHz/cm^2 for currents of 1.2 A on 2.8 A. Scaling this value to SuperB currents, the rate is expected to be 2-5 MHz in the high luminosity regime. This extrapolation is likely pessimistic, since the permanent dipoles in the final focus of PEP-II are eliminated in the SuperB design. Nevertheless, the rate found for SuperB is negligible with respect to the other sources of background. Synchrotron radiation is another source of background proportional to single beam currents. Starting from the fact that the interaction region has been designed to reduce as much as possible the bending with beam trajectories in the incoming beamline, some photons can still hit the beampipe. This would result in additional background in the detector and can give rise to outgassing due to heating, degrading local vacuum. The rate of photons, with energy about 10 keV, hitting the beampipe is expected to be $\approx 1500\gamma$ per bunch crossing.

4.2 Studies on neutron background

The principal reason why the neutron background studies are so important, is to estimate the neutron rate for understanding the best region to place the photodetectors. As seen in previous chapters, the photodetectors have a sensitive area made of silicon, whose damage is a function that has a strong dependance on the energy spectrum, as shown in Fig. 4.1. To obtain useful rate estimation we need to scale the doses, obtained from our studies, to 1 MeV, according to ASTM-E722, 93[58].

In the Instrumented Flux Return, it is possible to examine some regions (see Fig. 4.2) defined hot concerning neutron background:

- inner layers in the forward endcap and small radii (red color);
- innermost layers of barrel (blue color);
- inner layers in the backward endcap and small radii (orange color);
- outer layers in the forward endcap (violet color);

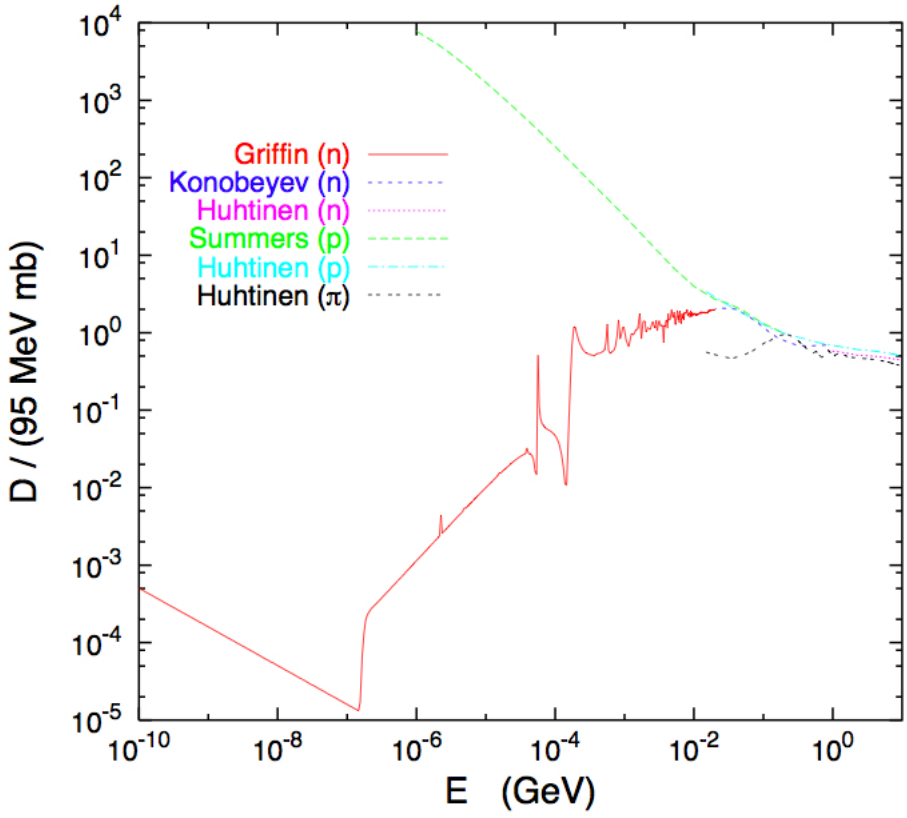

Figure 4.1: *Silicon damage function: the X axis represents the kinetic energy of neutron while the Y axis the silicon damage function.*

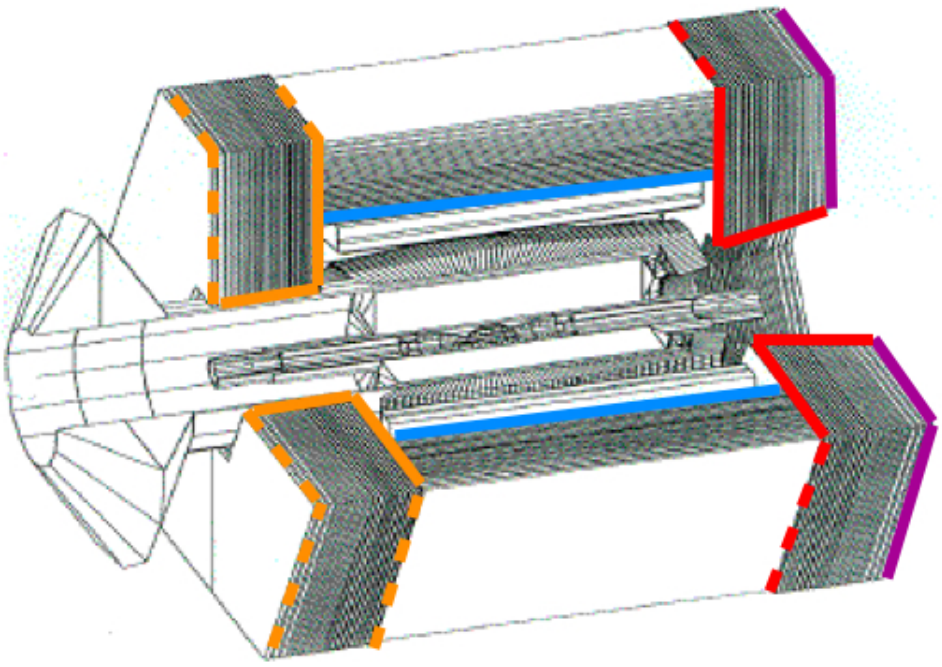

Figure 4.2: *Hot background regions for the IFR.*

In the next paragraphs results on this study will be shown and a preliminary neutron rate will be calculated, starting from full simulation data.

4.2.1 Rate studies

For studying neutron rate background we started from radiative Bhabha data simulated with full simulation tool and we studied the energy distribution, with different physics list and the neutron rate distribution in several layers of the IFR. The neutrons generated in radiative Bhabhas can cross the same layer more than once: for example a neutron is generated in the final focus with an energy around 1 MeV; then the neutron travels through the inner detectors and enters the forward endcap with a kinetic energy of 70 keV. The neutron can exit and re-enter the endcap surface 4.3 more than one time, this will be counted three times in the boundary survey and it will also hit the layer with three different energies. This is right for studying the neutron rate and for evaluating the silicon damage.

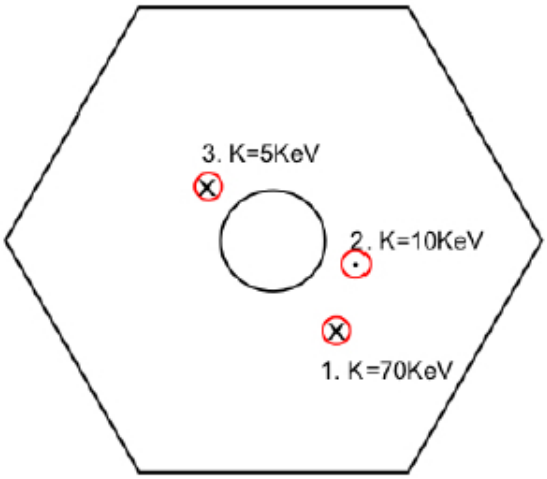

Figure 4.3: *Example of neutron path in the endcap.*

The data generated from full simulation contain different parameters than can be changed:

cuts on photon minimum energy We study three different cuts on the photon energy of the radiating beam : 10%, 2% and 0.5%. In particular we concentrate our attention in the barrel region and forward region, that are hotter sections more where the rate can be overestimated.

In Fig. 4.4 we plot the $\log E_{kinetic}(GeV)/\log 10$ distribution for the barrel(a) and forward region(b): it can be seem that the distribution is independent of photon energy cuts.

Figure 4.4: $\log[E_{kinetic}(GeV)]/\log(10)$ *distribution for different cuts on energy photon.*

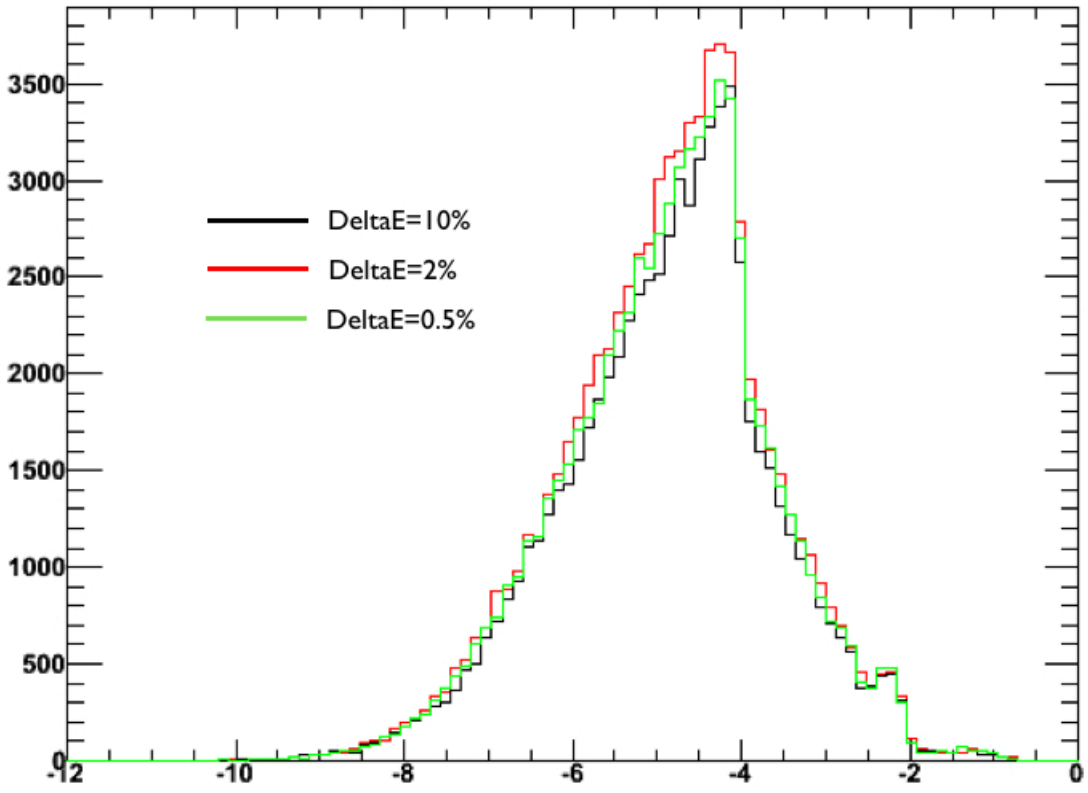

(a) Barrel region

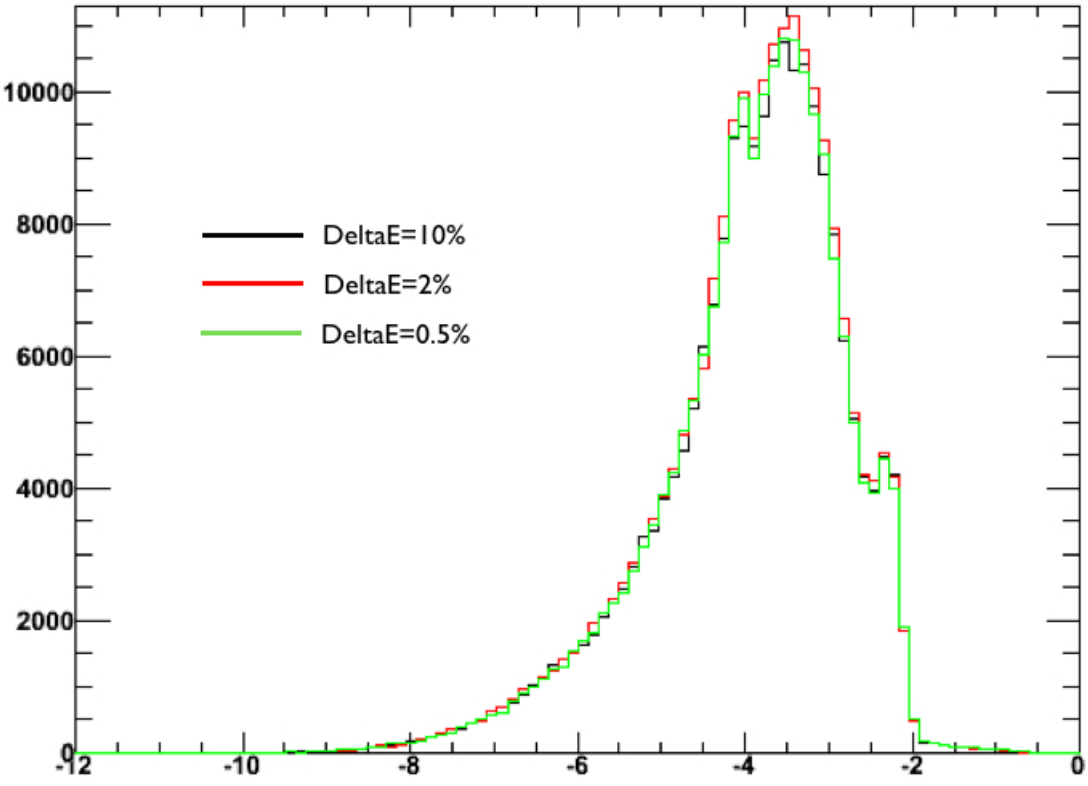

(b) Forward region

physics list, used for simulating Bhabha events During the generation of data it is possible to select which physics list[85] to use, in specific we used three:

1. **QGSP(Quark-Gluon String Precompound) model:** built from several component models which handle various parts of a high energy collision. The quark-gluon string (QGS) part handles the formation of strings in the initial collision of a hadron with a nucleon in the nucleus. String fragmentation into hadrons is handled by the Quark-Gluon String fragmentation model. The precompound part handles the de-excitation of the remnant nucleus. This list is valid for $\pi^+, \pi^-, p, n, K^+, K^-, K^0_L, K^0_S$ and in the energy range [12 GeV, 100 TeV].
2. **QGSP_BERT:** like QGSP, but using Geant4 Bertini[30] cascade for primary protons, neutrons, pions and Kaons below ∼10 GeV. In comparison to experimental data we find improved agreement to data compared to QGSP which uses the low energy parametrized (LEP) model for all particles at these energies. The Bertini model produces more secondary neutrons and protons than the LEP model, yielding a better agreement to experimental data. The QGSP_BERT are less CPU performant as QGSP.
3. **QGSP_BERT_HP:** this list is similar to QGSP_BERT and in addition uses the data driven high precision neutron package (NeutronHP) to transport neutrons below 20 MeV down to thermal energies.

Naturally some differences between physics lists will occur (Fig. 4.5). In fact the best physics list for neutrons is the last one, **QGSP_BERT_HP**, due the fact that the precision is better.

geometry configuration of subdetectors During the optimization of a detector it is possible to change the geometry of one subdetector. For screening the Silicon Vertex Tracker from electrons and photons, a shield of wolframium has been inserted around the final focus, producing a higher rate of neutrons (Fig. 4.6) in the IFR system, so this shield is very powerful for the SVT detector but is also a good neutron generator.

It has been shown that there are some parameters it is possible to change, influencing the result on neutron rate studies. Now we want to concentrate our attention to the neutron rate distribution in each layer of the IFR barrel and in the endcaps, especially in hot regions (see Fig. 4.2). In the following plots only the shield geometry configuration has been considered for understanding the distribution in several layers; this rate

Figure 4.5: $\log\left[E_{kinetic}(GeV)\right]/\log\left(10\right)$ *distribution for different physics lists.*

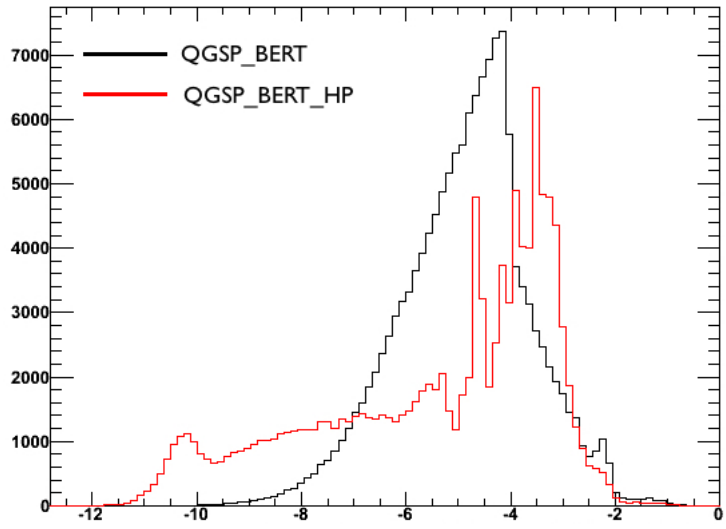

(a) Barrel region

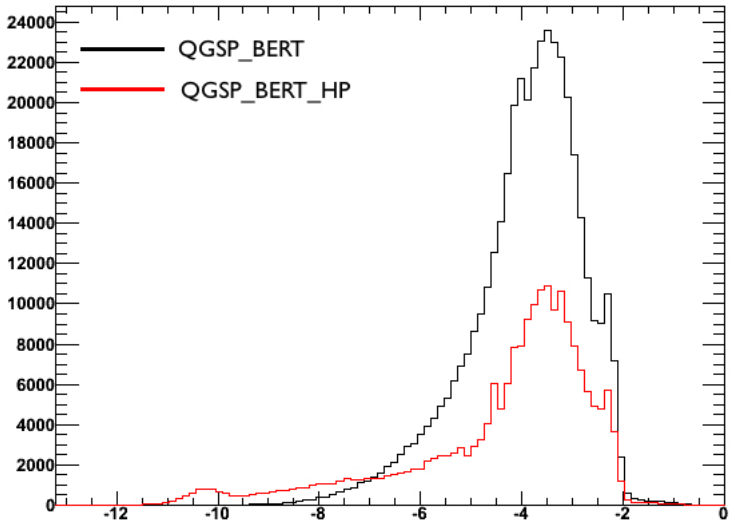

(b) Forward region

Figure 4.6: *Neutron energy distribution with shield and unshield configuration.*

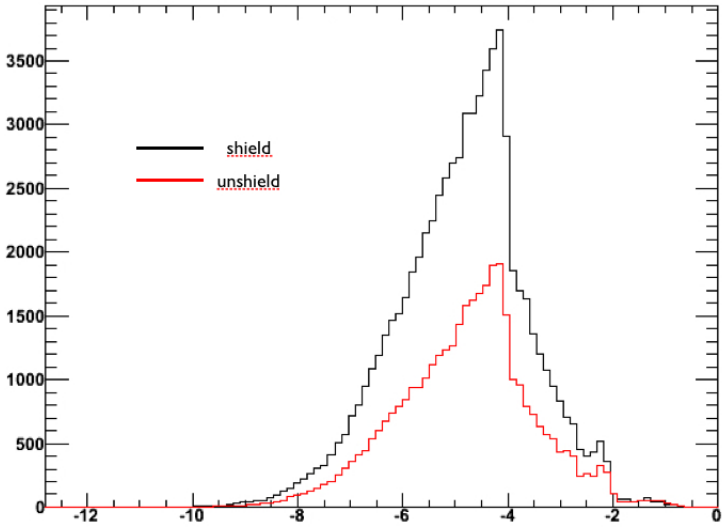

(a) Barrel region

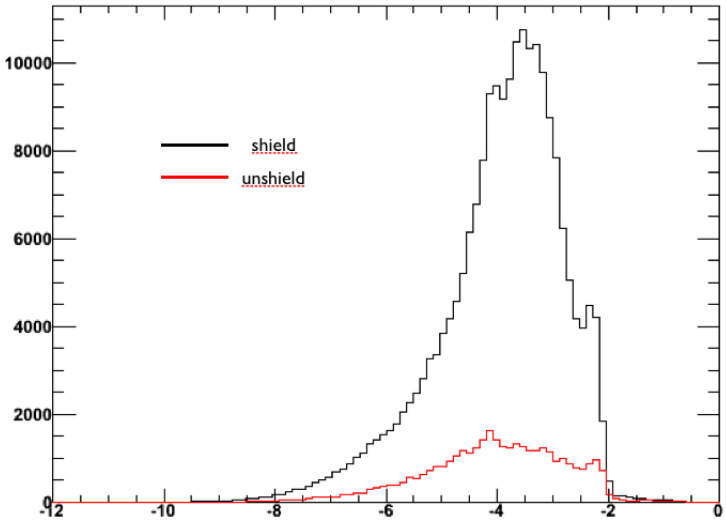

(b) Forward region

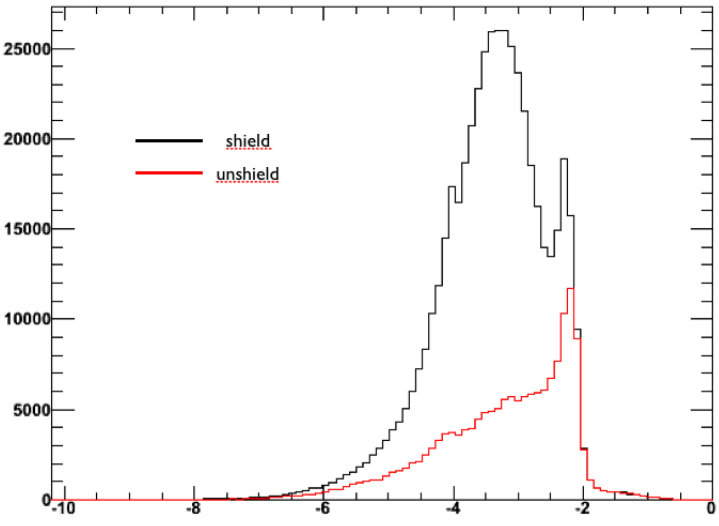

(c) Final focus region

is overestimated because, as seen previously, the shield configuration produces a lot of neutrons.

It is important to estimate the rate with different physics list too, in particular the following neutron rate plots (4.7) are obtained using the QGSP_BERT physics list and considering the wolframium shield around the SVT. In the Fig. 4.8 the maximum neutron rate occurs in the Forward Endcap, about $1.8 \cdot 10^2$ Hz/cm^2, so during a one Snowmass year [1] the neutron rate is equivalent to $2.7 \cdot 10^9$ neutron for cm^2 (in next paragraph is will be shown that this value is high).

If we consider the case without the wolframium shielding the neutron rate decreases (Fig. 4.9), because, as seen previously, the tungsten is useful for electrons and photons but not for neutrons.

In fact it is possible to note that now, without the shielding, the maximum rate observed, in one Snowmass year, is $6 \cdot 10^8$ neutron for cm^2. This rate is one order of magnitude lower with the tungsten shield. The option without the shield has been discarded by the collaboration, so the IFR team has to provide a solution for screening the IFR system from neutrons.

One solution proposed is to insert, between the solenoid magnet and the barrel, a polyethylene shield 10 cm thick, represented in Fig. 4.11, and study the neutron rate with this solution. Theoretically the neutron rate should decrease by a factor 10 and a comparison between the solutions without and with the neutron shield using the QGSP_BERT_HP, the most precise, will be given in the next plots.

Fig. 4.12 shows the reduction of neutron rate, in fact the layer is hit more times without the shield. Obviously the effect of this polyethylene shield in the backward and forward region, is to remove the halo around the beam pipe without affecting the neutron rate. In particular Fig. 4.14 shows that the decrease of one order of magnitude occurs in the barrel region, as foreseen, but not in the forward and backward endcaps.

This reduction is important for our studies because to put into the detector a polyethylene shield it is a plausible way to avoid a high neutron rate that causes a silicon damage as we will see in the next paragraph.

4.2.2 Studies on silicon damage

Some tests has been performed at the Frascati Neutron Generator on Silicon Photo-Multipliers[13], a semiconductor photon detectors built from a square matrix of avalanche photodiodes on a silicon substrate. Several samples from different manufactury have been

[1] This is equivalent to one year of run machine, $1.5 \cdot 10^7$ s

Figure 4.7: *Neutron rate distribution Hz/cm^2 with the wolframium shield around SVT, using the QGSP_BERT physics list.*

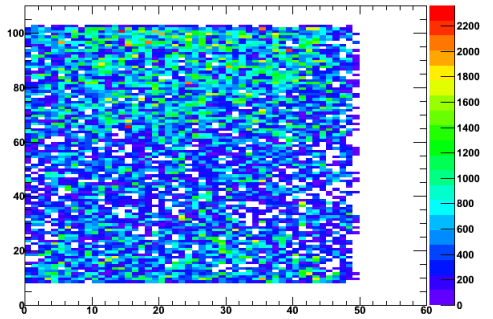

(a) Sextant 1

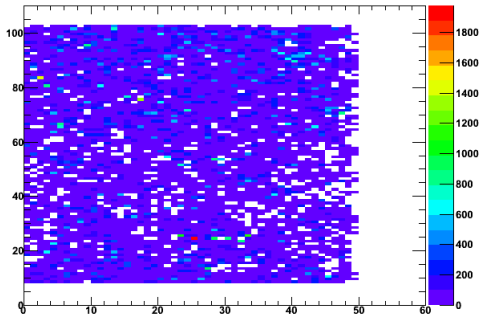

(b) Sextant 1 normalized to 1 MeV

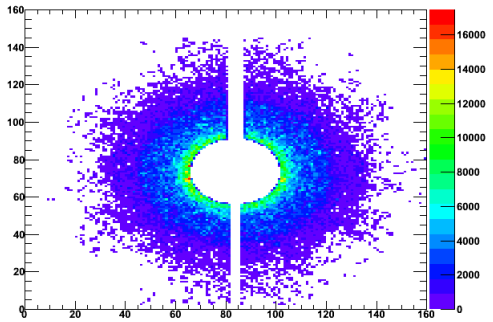

(c) Forward endcap distribution

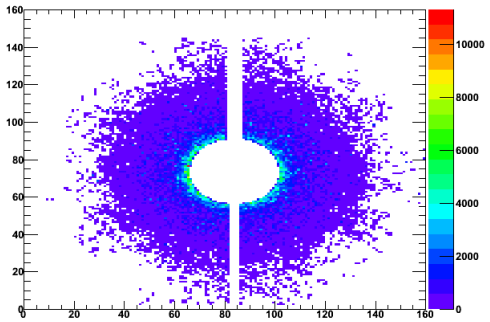

(d) Forward endcap distribution normalized to 1 MeV

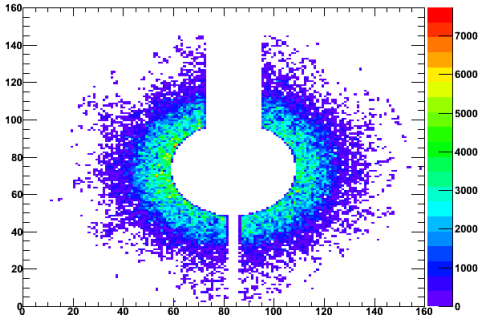

(e) Backward endcap distribution

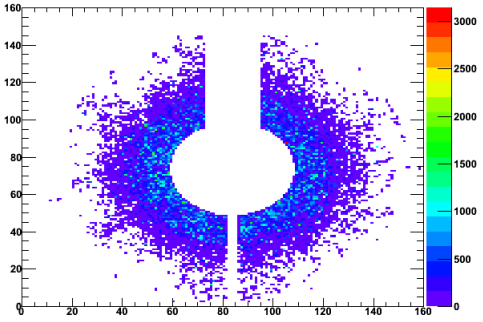

(f) Backward endcap distribution normalized to 1 MeV

Figure 4.8: *Average neutron rate distribution normalized to 1 MeV for each layer with the wolframium shield around SVT, using the QGSP_BERT physics list*

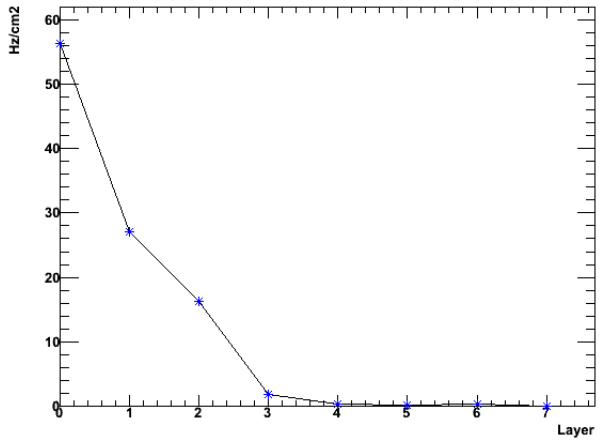

(a) Sextant 1

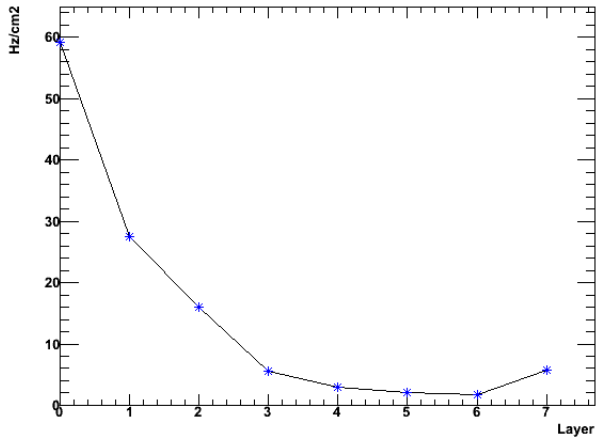

(b) Backward endcap

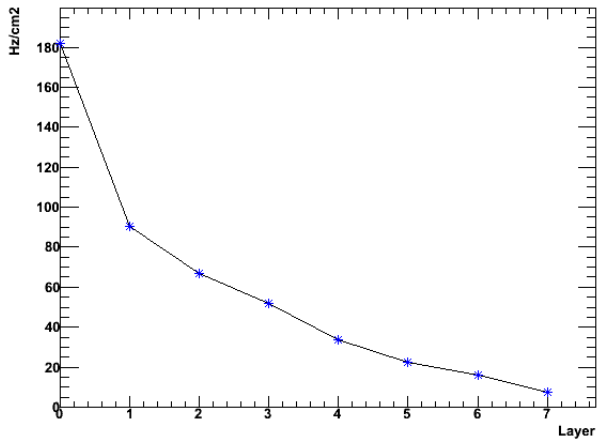

(c) Forward endcap

Figure 4.9: *Neutron rate distribution Hz/cm^2 without the wolframium shield around SVT, using the QGSP_BERT physics list.*

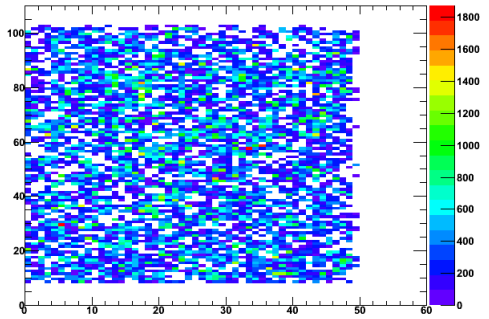

(a) Sextant 1

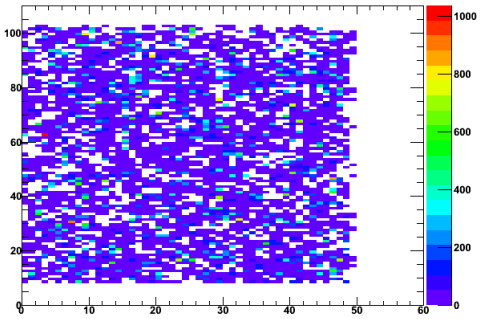

(b) Sextant 0 normalized to 1 MeV

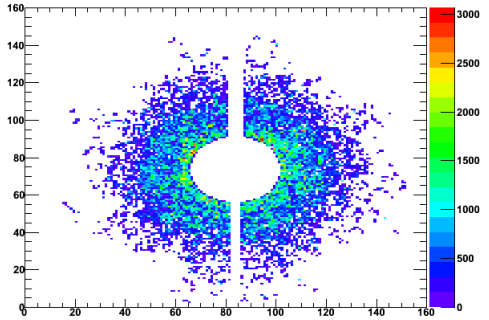

(c) Forward endcap distribution

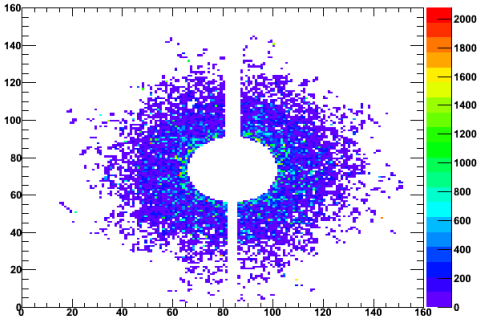

(d) Forward endcap distribution normalized to 1 MeV

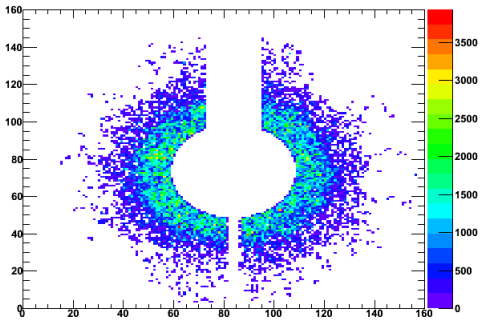

(e) Backward endcap distribution

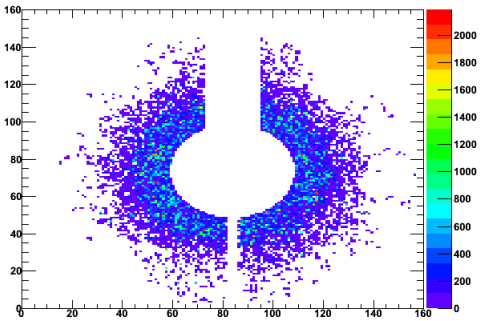

(f) Backward endcap distribution normalized to 1 MeV

Figure 4.10: *Average neutron rate distribution normalized to 1 MeV for each layer without the wolframium shield around SVT, using the QGSP_BERT physics list*

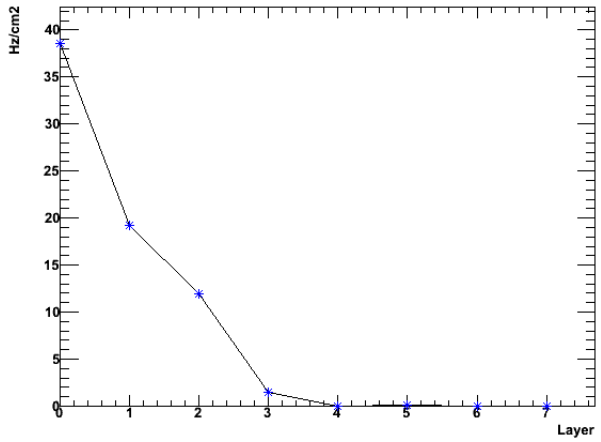

(a) Sextant 1

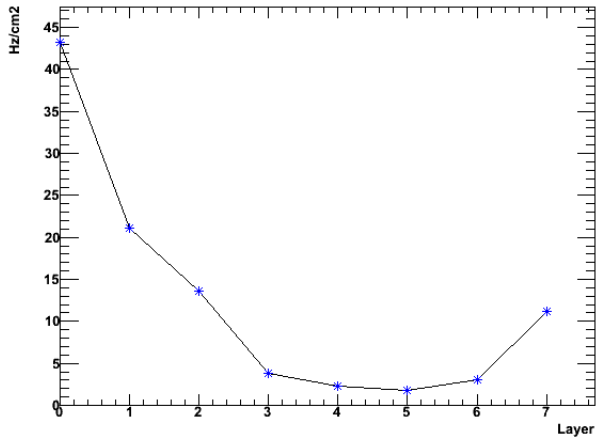

(b) Backward endcap

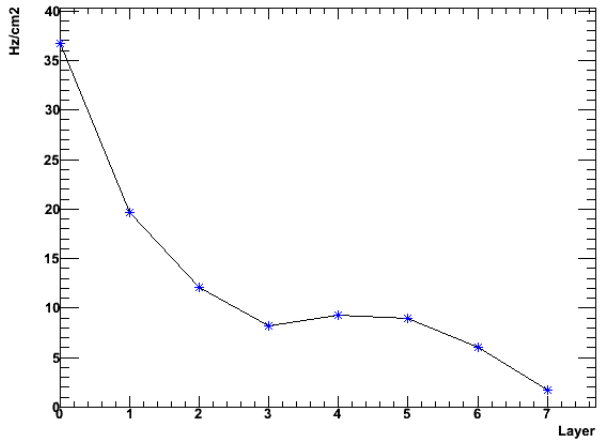

(c) Forward endcap

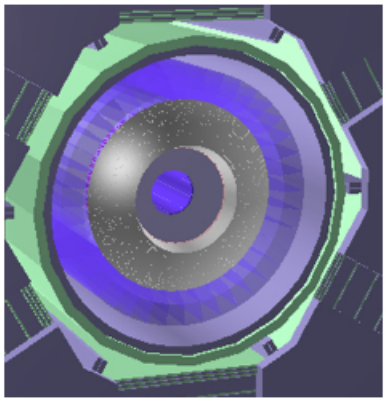

Figure 4.11: *View of the polyethylene shield, the light green one, before the IFR.*

irradiated integrating up to 7× 10^{10} 1 MeV-equivalent neutrons per cm^2, and it has been seen that there is a gradual degradation of photodetector properties after an integrated irradiation of the order of 10^8 1 MeV-equivalent neutrons per cm^2.

The device has been irradiated using a deuteron beam accelerated up to 300 keV impinging on a deuteron target to produce a nearly isotopic 2.5 MeV neutron output via the D(d,n)^{3}He fusion reaction. The position of these and their irradiated fluence are reported in Tab. 4.1.

Table 4.1: *Device positions in a frame centered in the neutron generation point and with the z axis coincident with the deuteron beam axis and the total integrated fluences.*

Devices	x (mm)	y (mm)	z (mm)	tot. int. fluence ($10^{10} n_{eq}/cm^2$)
SiPM #4	5.0	0.0	3.0	1.25
SiPM #6	3.0	1.3	3.0	3.07
SiPM #7	-0.5	0.0	13.0	0.18
SiPM #8	-1.0	0.0	3.0	7.32
MPPC #1	-3.0	0.0	3.0	2.71
MPPC #2	1.0	0.0	3.0	7.32
MPPC #5	-0.5	0.0	2.5	4.26
MPPC #6	0.5	0.0	2.5	4.26
SiPM 2×2	-5.0	0.0	3.0	1.25

During the irradiation the dark current as a function of the irradiation time has been plotted and in Fig. 4.15 we see that after four hours of data-taking some devices worsened by a factor 30, others by a factor 10.

Figure 4.12: *Neutron rate distribution Hz/cm^2 in layer 0 with the wolframium shield around SVT, using the QGSP_BERT_HP physics list.*

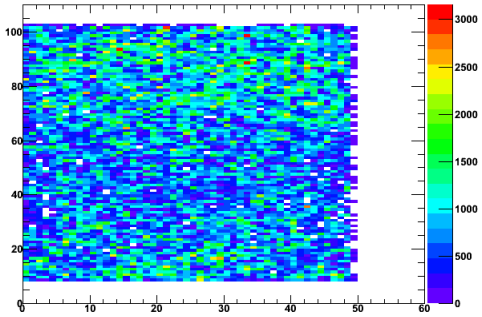

(a) Sextant 1 without the polyethylene shield before the barrel

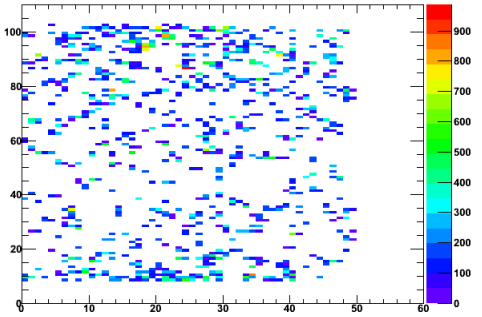

(b) Sextant 1 with the polyethylene shield before the barrel

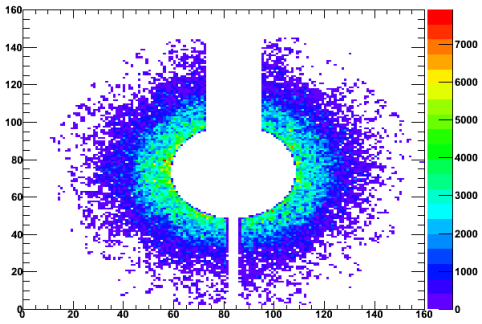

(c) Backward endcap without the polyethylene shield before the barrel

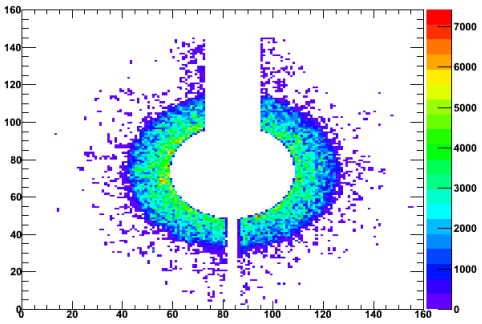

(d) Backward endcap with the polyethylene shield before the barrel

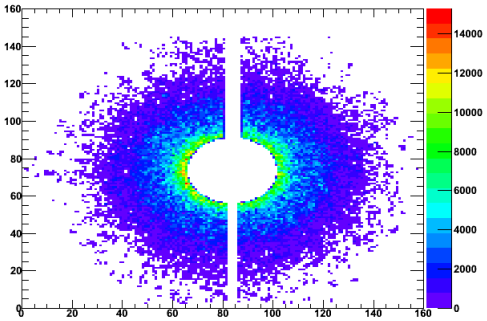

(e) Forward endcap without the polyethylene shield before the barrel

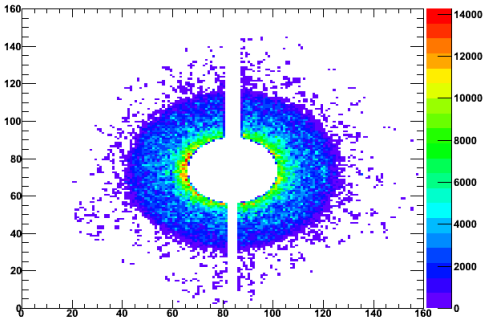

(f) Forward endcap with the polyethylene shield before the barrel

Figure 4.13: *Neutron rate distribution normalized to 1 MeV Hz/cm^2 with the wolframium shield around SVT, using the QGSP_BERT_HP physics list.*

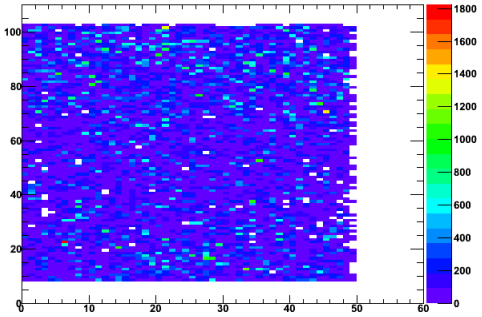

(a) Sextant 1 without the polyethylene shield before the barrel

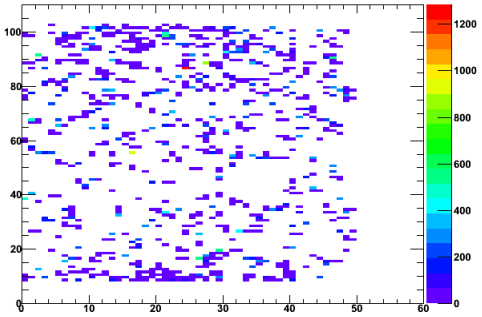

(b) Sextant 1 with the polyethylene shield before the barrel

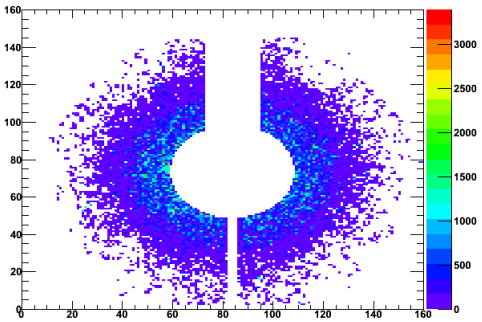

(c) Backward endcap without the polyethylene shield before the barrel

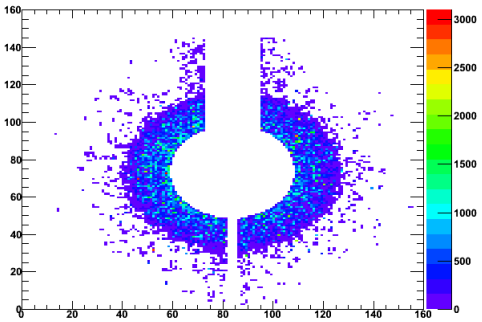

(d) Backward endcap with the polyethylene shield before the barrel

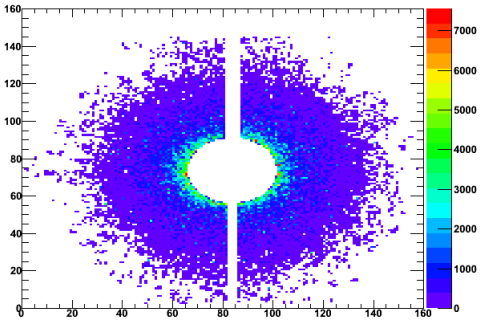

(e) Forward endcap without the polyethylene shield before the barrel

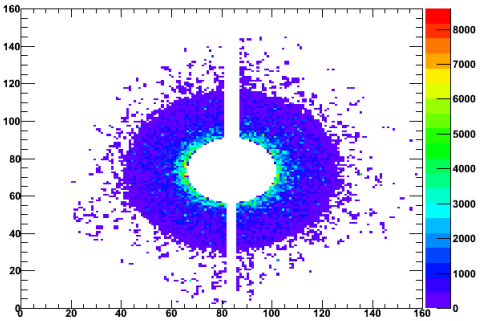

(f) Forward endcap with the polyethylene shield before the barrel

Figure 4.14: *Neutron average rate distribution normalized to 1 MeV Hz/cm^2, using the QGSP_BERT_HP physics list.*

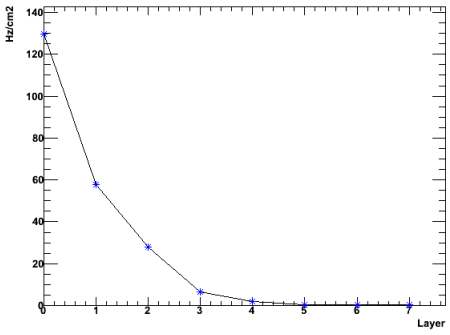

(a) Sextant 1 without the polyethylene shield before the barrel

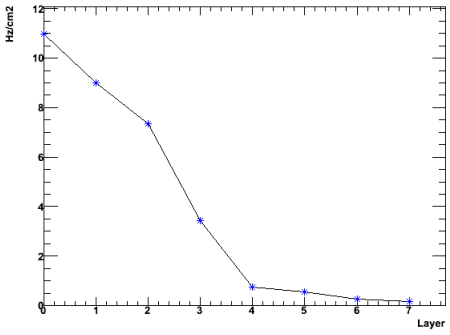

(b) Sextant 1 with the polyethylene shield before the barrel

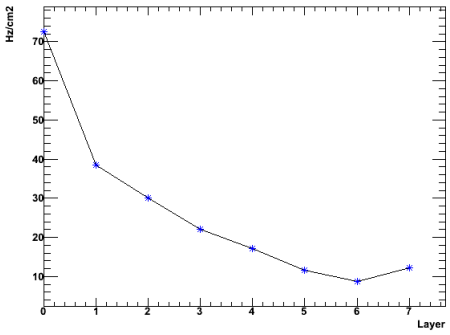

(c) Backward endcap without the polyethylene shield before the barrel

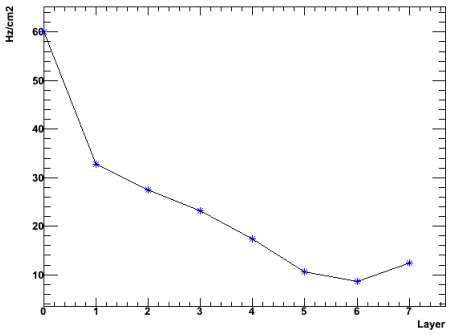

(d) Backward endcap with the polyethylene shield before the barrel

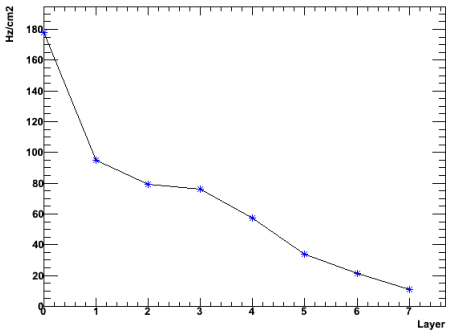

(e) Forward endcap without the polyethylene shield before the barrel

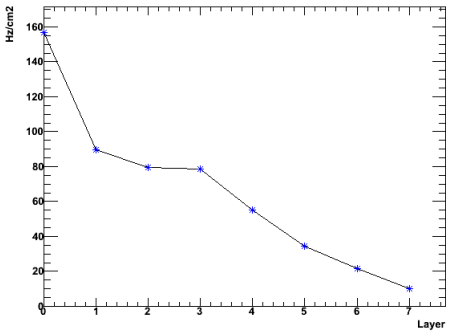

(f) Forward endcap with the polyethylene shield before the barrel

Figure 4.15: *Neutron irradiation on SiPMs*

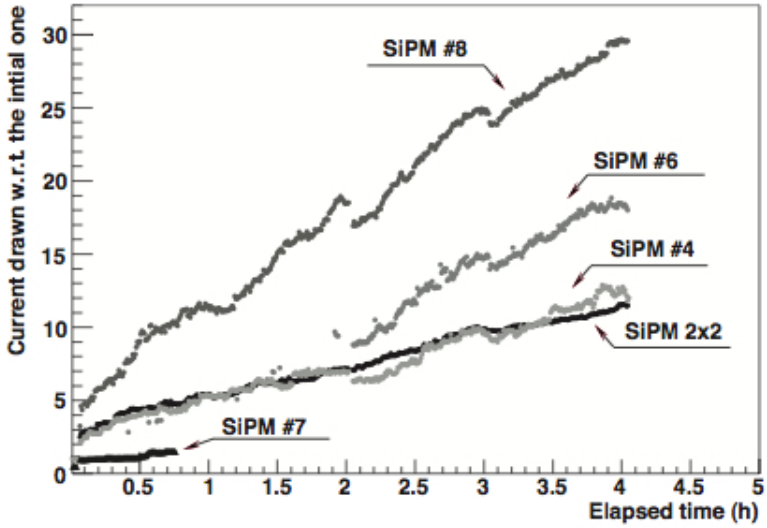

(a) Increase factors of the current drawn by the SiPMs as a function of the irradiation time

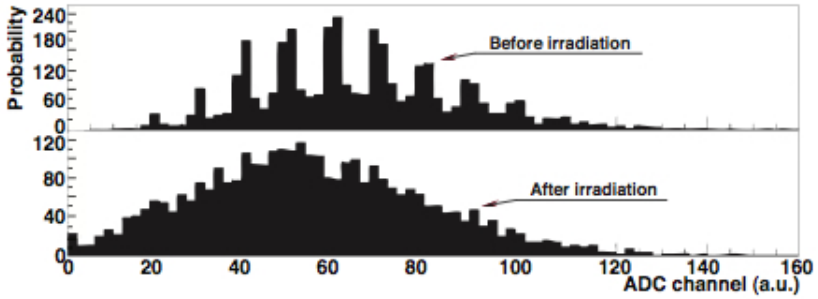

(b) SiPM spectra for a low intensity LED run, before (top) and after (bottom) irradiation

The effects of the irradiation on the gain was studied by testing the response of the photodetectors to a pulsed LED (see Fig. 4.15) yielding a low number of photo-electrons. Measurements show that after the irradiation there is a degradation of the single-photon resolution due the increase of the noise, having a significant reduction of the detection efficiency from more than 95% to 70%.

After these test it has been possible to see an important degradation of silicon after an irradiation of few $10^8 n_{eq}/cm^2$. Using data from full simulation (see previous paragraph) we conclude that the silicon photodetectors will be damaged in $\sim$ 1 year, not considering any safety factor and, surely , the simulation rate is underestimated, due the fact that the beam halo is not completely simulated. In this case a neutron screen is needed between solenoid and the IFR structure or the position where to place photodetectors must be changed.

4.3 Studies on e^+e^- background

In the previous paragraphs we studied two different configurations of the detector: the first one without the wolframium shield around the SVT and the other one with. It has been shown that the presence of this shield affects the neutron rate on the IFR detector. Now it is crucial to evaluate the impact of the shield on e^+ e^- rate in the IFR detector.

This study is only useful to evaluate the effect of the shield on the positrons and electrons rate, noting that this should not disturb the IFR detector in a sensitive manner.

Fig. 4.17 shows the electron and positron energy distribution with and without the the shield: it is clear that the shield has the effect to absorb electrons and positron in order to avoid silicon detectors damage of the SVT caused by the high rate.

Looking at Fig. 4.17 it is essential to point out that the rate decrease is more visible for the IFR,whereas the effect on the final focus is not so evident: in Fig. 4.17(c) the decrease is only clear for low-energy electrons and positrons. So it seems that the first consequence of the shield is to eliminate the electrons with low energies.

The effects of the electrons and positron absorption is visible from the Fig. 4.18 to Fig. 4.20, where the colour scale decreases if we are comparing the shielded configuration with respect to the unshielded one, comparing the plots with the same physics list. It is important to remark also that there are no differences between the intermediate (QGSP_BERT) and the high precision (QGSP_BERT_HP) physics lists. This fact is expected, because from the point of view of physics description, for what concerns the electrons and positrons, there are no differences.

It is crucial to observe, looking at Fig. 4.20 that the rate in the last layer of the back-

ward and forward endcaps is underestimated because the beam pipe has been simulated up to ±3 m from the interaction point, so expanding the beam pipe it is obvious that the rate will have an increase.

Figure 4.16: *log($E_{kinetic}$(GeV))/log(10) for different physics lists.*

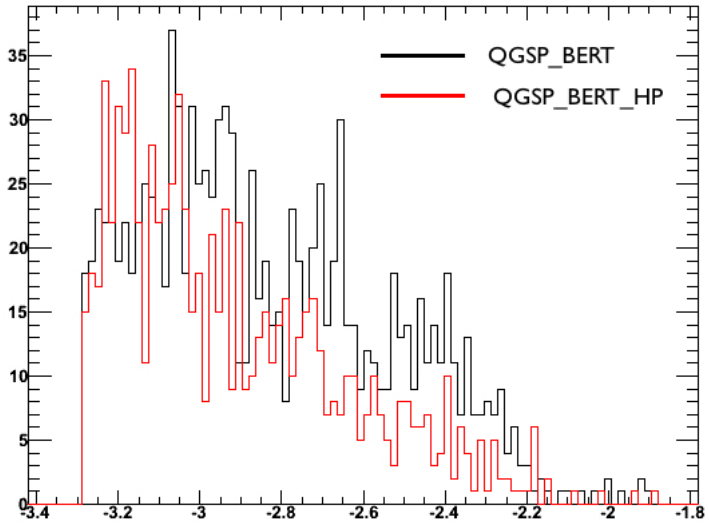

(a) Barrel region

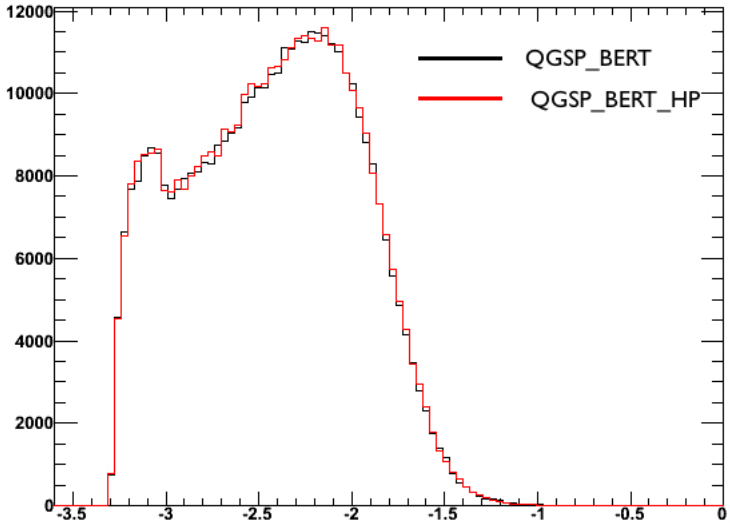

(b) Forward region

4.4 Studies on γ background

The same considerations done for the electrons and positrons apply also to photons. In fact the rate decrease is evident from Fig. 4.23 to Fig. 4.25, always comparing at plots with the same physics list. Fig. 4.22 shows the photons energy distribution with and

Figure 4.17: *log($E_{kinetic}$(GeV))/log(10) electrons/positrons distribution with shielded and unshielded configurations.*

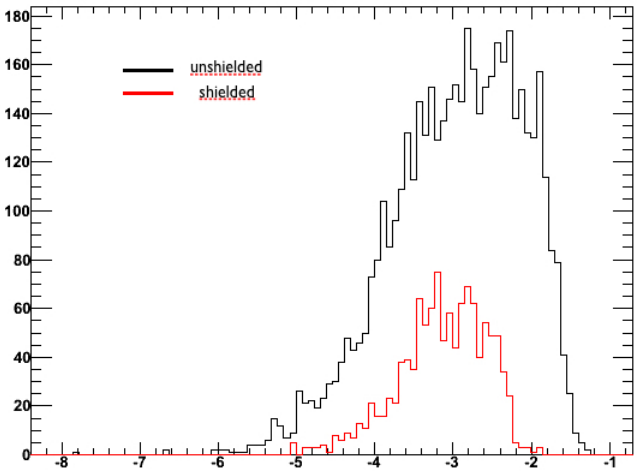

(a) Barrel region

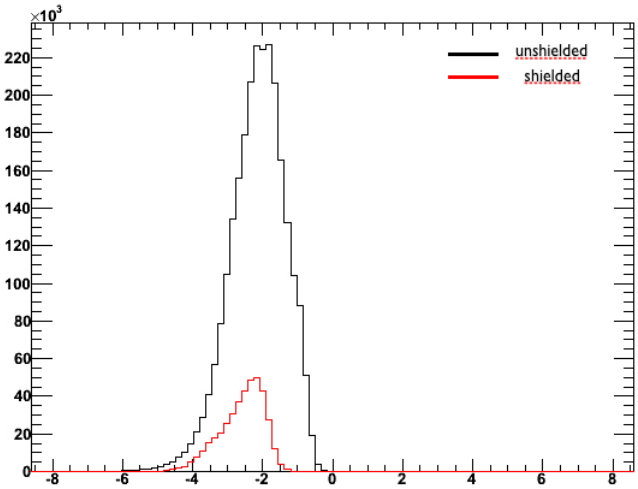

(b) Forward region

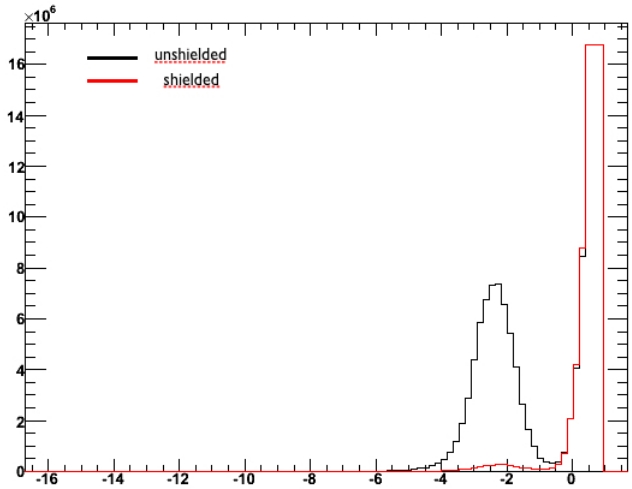

(c) Final focus region

Figure 4.18: *Electrons and positron rate Hz/cm^2 in the IFR detector with the unshielded configuration and physics list QGSP_BERT*

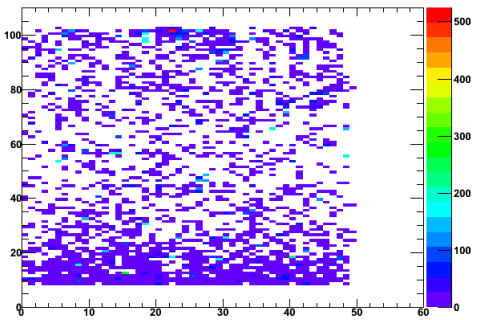

(a) Sextant 1 - Layer 0

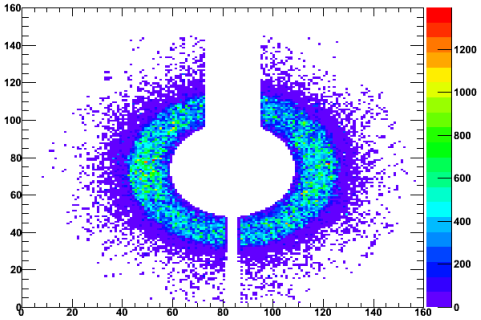

(b) Backward endcap - Layer 0

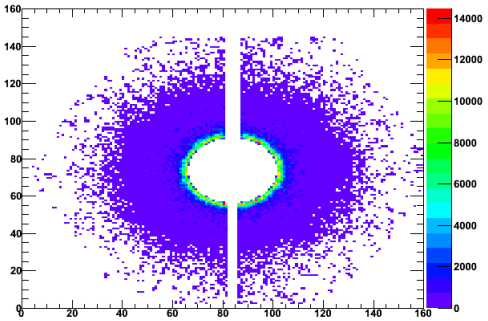

(c) Forward endcap - Layer 0

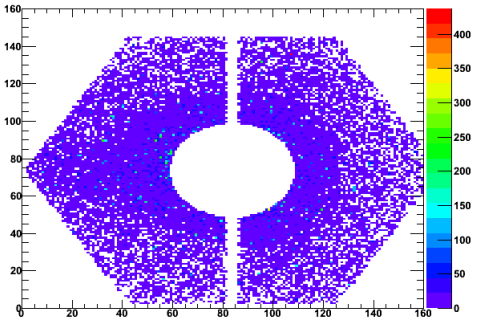

(d) Backward endcap - Layer 7

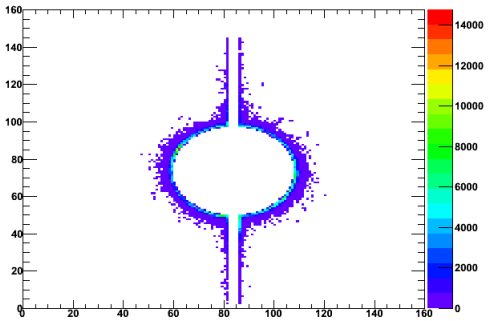

(e) Forward endcap - Layer 7

Figure 4.19: *Electrons and positron rate Hz/cm^2 in the IFR detector with the shielded configuration and physics list QGSP_BERT*

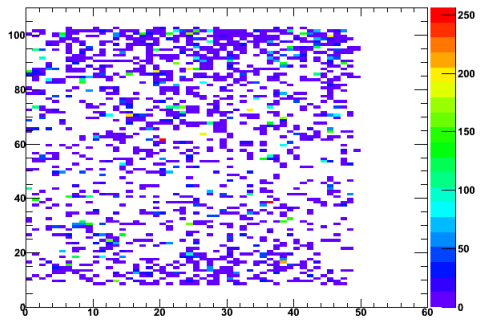

(a) Sextant 1 - Layer 0

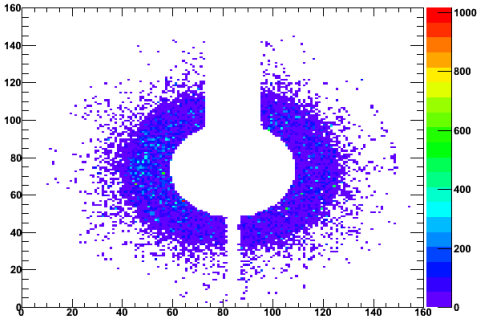

(b) Backward endcap - Layer 0

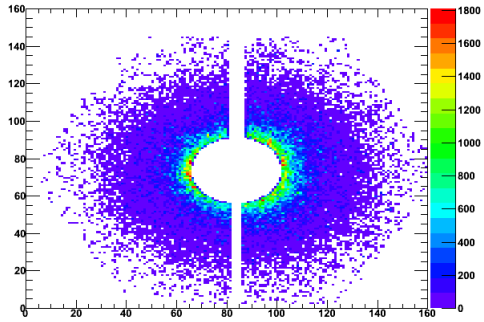

(c) Forward endcap - Layer 0

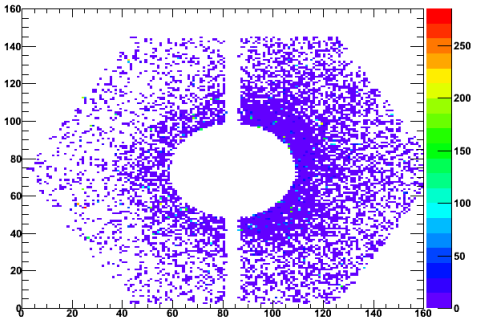

(d) Backward endcap - Layer 7

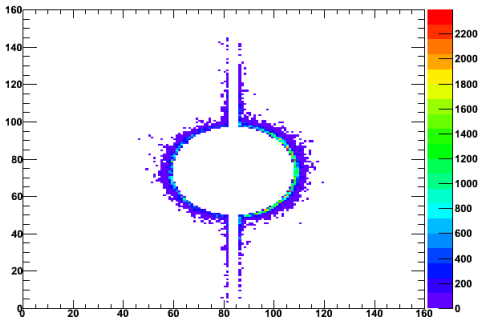

(e) Forward endcap - Layer 7

Figure 4.20: *Electrons and positron rate Hz/cm^2 in the IFR detector with the shielded configuration and physics list QGSP_BERT_HP*

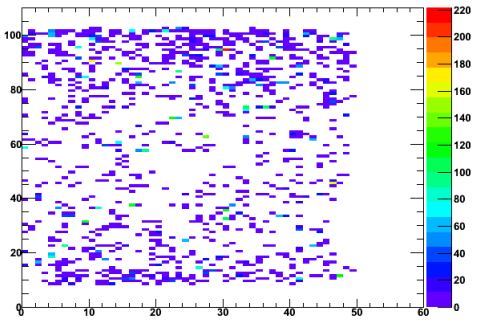

(a) Sextant 1 - Layer 0

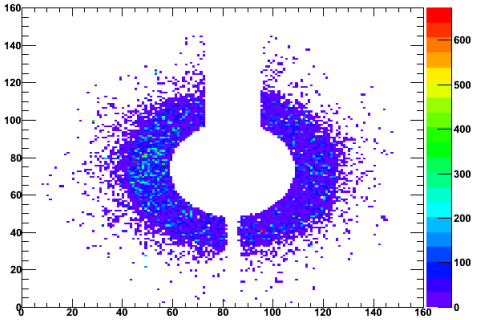

(b) Backward endcap - Layer 0

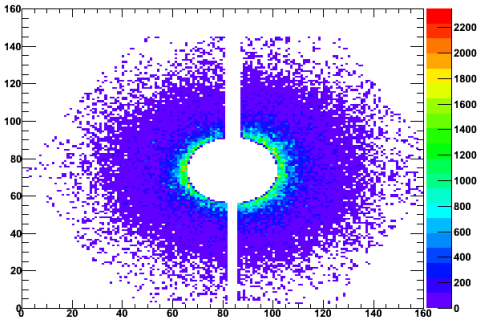

(c) Forward endcap - Layer 0

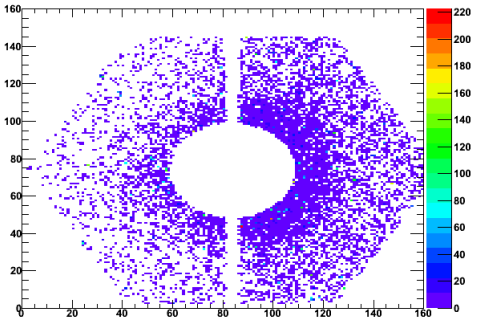

(d) Backward endcap - Layer 7

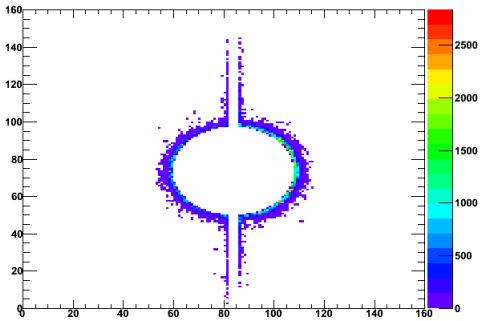

(e) Forward endcap - Layer 7

without the shield in different locations of the SuperB detector: in the barrel region and forward region of the IFR detector and in the final focus, the rate decrease is evident. As shown for the electrons and positrons, there are no differences, as expected, between the two physics lists studied: in fact the physics description for these particles does not change.

Figure 4.21: *log($E_{kinetic}$(GeV))/log(10) for different physics lists.*

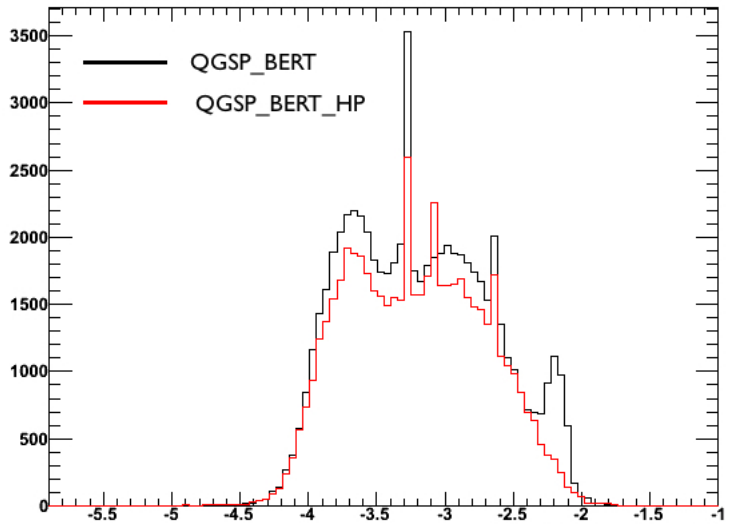

(a) Barrel region

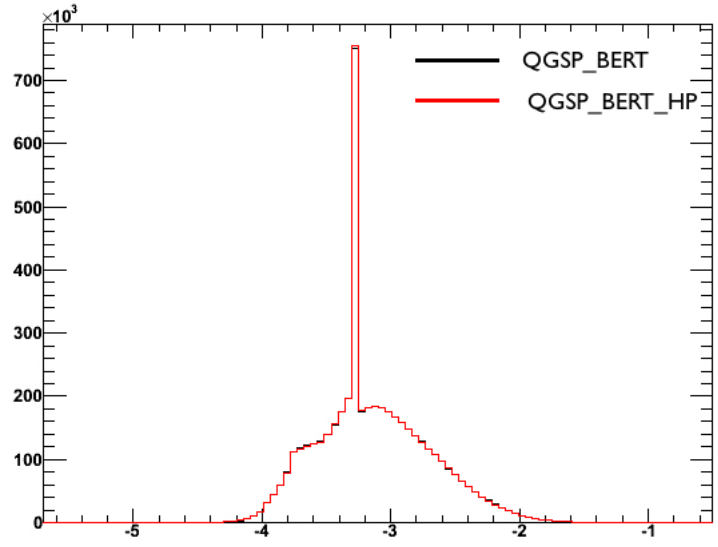

(b) Forward region

Figure 4.22: *log(E(GeV))/log(10) photons distribution with shielded and unshielded configurations.*

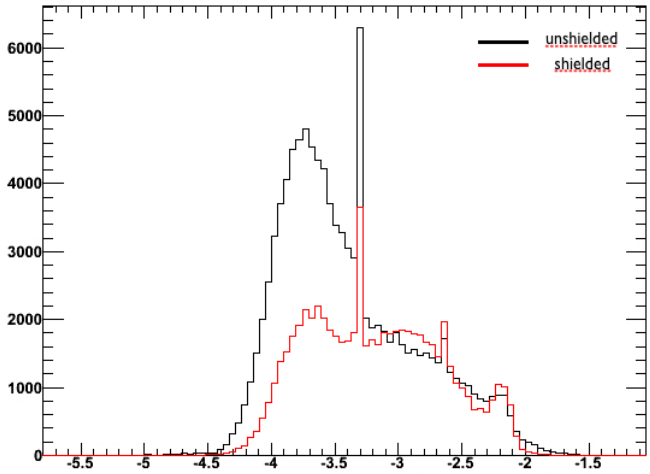

(a) Barrel region

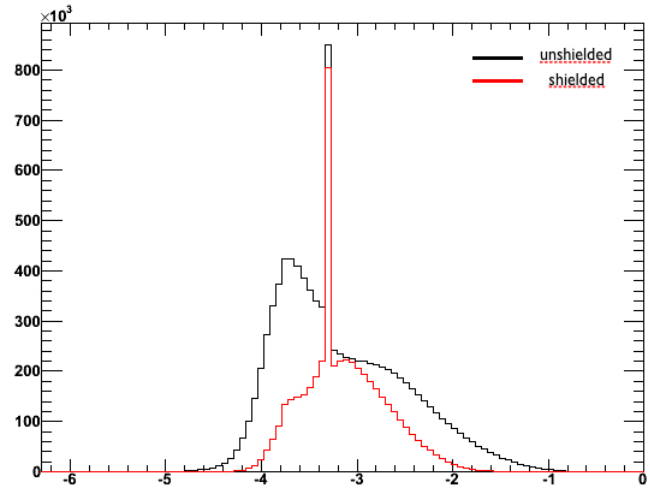

(b) Forward region

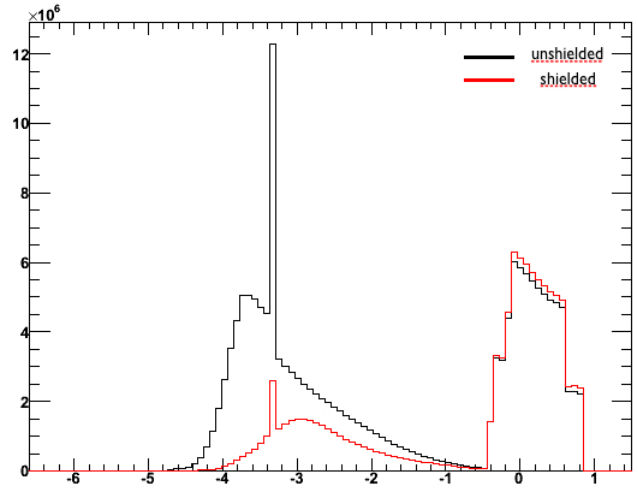

(c) Final focus region

Figure 4.23: *Photons rate in the IFR detector with the unshielded configuration and physics list QGSP_BERT*

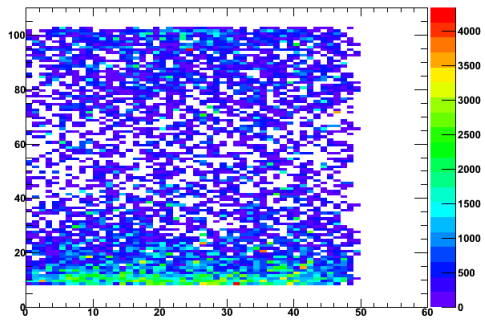

(a) Sextant 1 - Layer 0

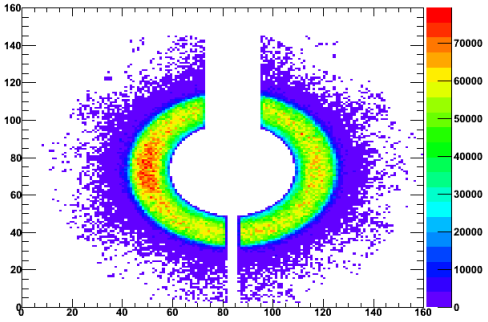

(b) Backward endcap - Layer 0

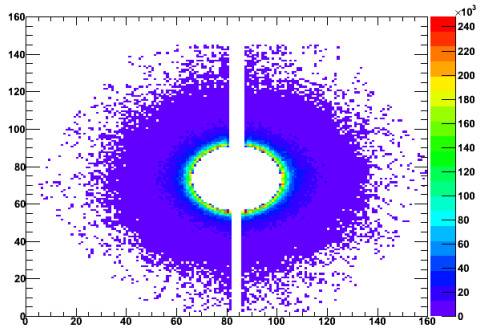

(c) Forward endcap - Layer 0

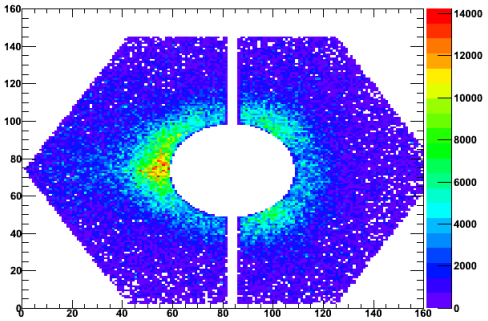

(d) Backward endcap - Layer 7

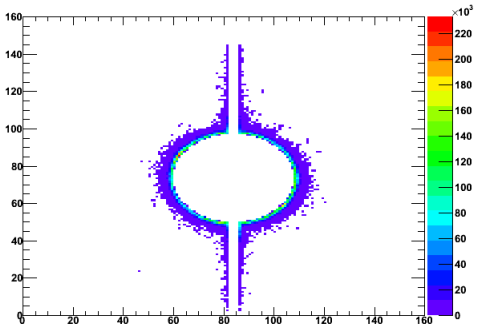

(e) Forward endcap - Layer 7

Figure 4.24: *Photons rate in the IFR detector with the shielded configuration and physics list QGSP_BERT*

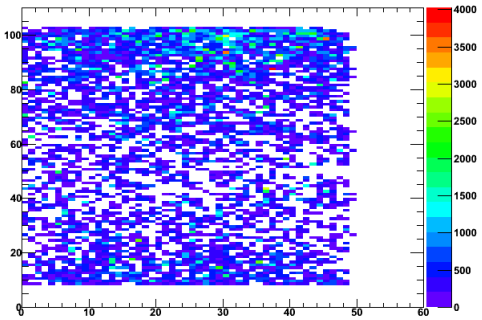

(a) Sextant 1 - Layer 0

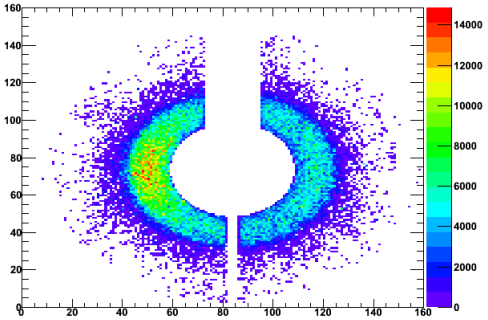

(b) Backward endcap - Layer 0

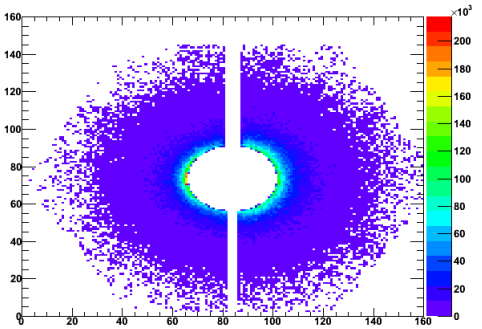

(c) Forward endcap - Layer 0

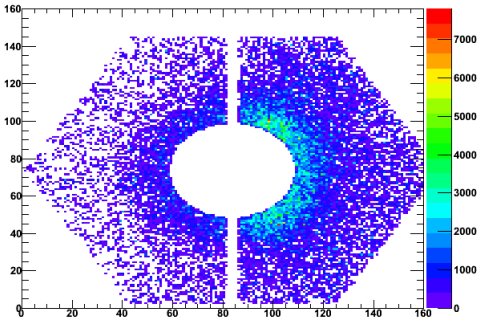

(d) Backward endcap - Layer 7

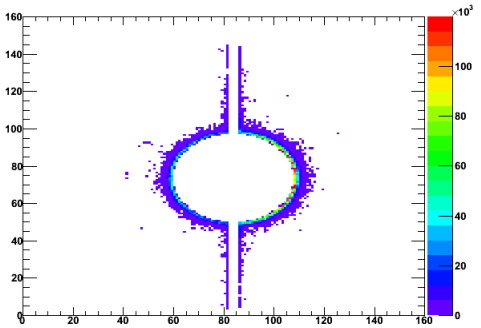

(e) Forward endcap - Layer 7

Figure 4.25: *Photons rate in the IFR detector with the shielded configuration and physics list QGSP_BERT_HP*

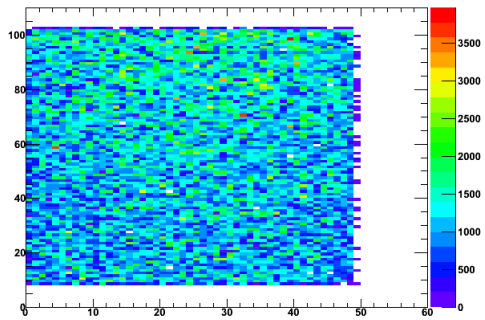

(a) Sextant 1 - Layer 0

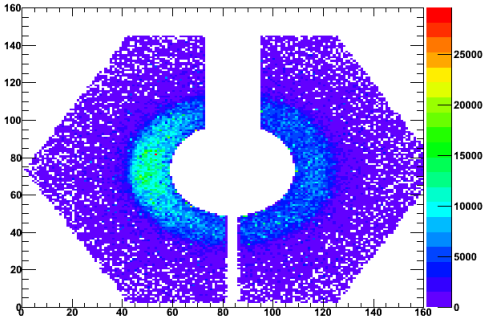

(b) Backward endcap - Layer 0

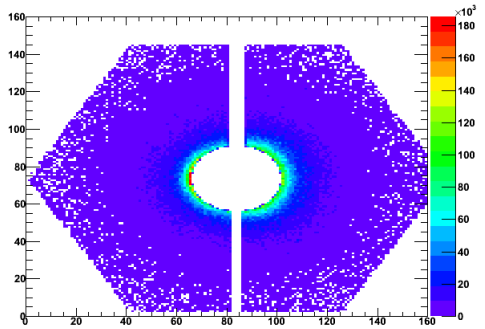

(c) Forward endcap - Layer 0

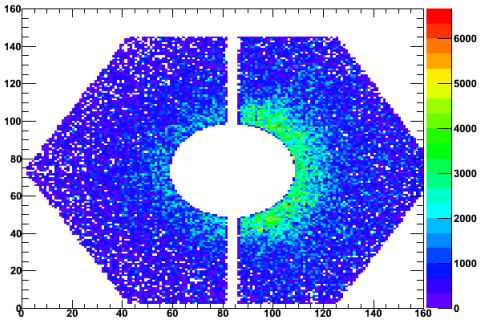

(d) Backward endcap - Layer 7

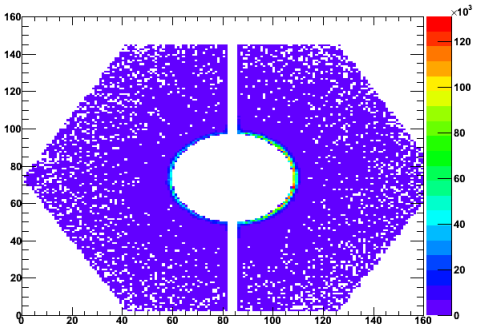

(e) Forward endcap - Layer 7

Chapter 5

Optimization of the IFR detector

The optimization for the IFR detector has been done using two approaches: the fast Simulation and the full Simulation. The former is more simplified: the detector response is parametrized using the results of fine full simulation; the latter is more realistic and there is a detailed description of the whole detector, so starting from the beam pipe a precise description of the SVT, DIRC, DCH, EMC and IFR has been done.

These sections will be dedicated to a brief description of the fast simulation, whereas the full one will be described in detail since it is the main focus of this work.

5.1 Fast simulation

Based on PACRAT (Physics Algorithm Collection of Reconstruction and Analysis Templates), the fast simulation has the main aim to optimize the design of the detector and for this reason it allows to modify quickly the geometry and other detector parameters.

With this type of simulation, it is possible to generate a large number of events in a very brief time with respect the full simulation, the 75% of less time. The fast simulation can be divided into four steps:

1. **Event Generator:** the generation of an event is done in EvtGen[5], a software that contains different models for simulations of B physics. There are modules to describe semileptonic decays, CP violation and consecutive decays.

2. **Simulation of detector material:** the geometry of the detector is parametrized to have a more quick simulation. In particular for the IFR sub-detector, for example, the barrel region is simulated as a cylinder and two endcaps are simulated as an ensemble of planes whose thickness is parametrized, similarly for interaction length and density.

3. **Simulation of detector response:** the description of particle interaction with material and the sequent detector response is one of the more expensive phase of simulation. The fast simulation is a reasonable compromise between precision of results and performances; in particular the interactions are parametrized and can ben grouped into three categories:

   - interactions with charged particles not producing secondary particles, for example with energy loss caused by ionization and direct scattering;
   - electromagnetic interactions, for example Compton process and pair production;
   - hadronic interactions, for example nuclear scattering and hadronic showers.

4. **Simulation of reconstruction into the detector:** from the point of the reconstruction of tracks in the detector, the passage of a particle is represented by a tracking hit with a related efficiency and resolution.

For the IFR detector it is crucial to know that the hadronic interactions are not described exactly in the fast simulation framework and since these are very important, the detector needs to be optimized with full simulation that will treated in the next section.

5.2 Full simulation

The full simulation, as seen before, has a detailed geometry description of the detector for simulating in a correct mode the interaction between the particle and the sensitive detector, so the full simulation is important for three factors:

- it is possible to study background in the detectors;
- it is useful to optimize the detectors;
- it is helpful to extract parameters for fast simulations.

The SuperB collaboration has implemented a code, as described in the last section of chapter 3, called **Bruno**, based on GEANT4, for the simulation of particle track, and on ROOT for the analysis of data.

In particular in the full simulation some main features will be treated in detail:

Geometry Description Markup Language (GDML)[1] : is an application-indipendent geometry description format based on XML. Using this language it is possible to create every geometric solid that permits to describe in a correct mode the detector

and it is possible to specify the chemical composition of the solid. The more precise a geometry description of a detector the more realistic the output of simulation, so the best way to optimize a detector is to have a quite perfect description of the detector. In Fig. 5.1 it is possible to see a first geometric description of the IFR: this description is very similar to BABAR and it has been implemented to satisfy the Conceptual Design Report, the new geometry is shown in the Fig. 5.2.

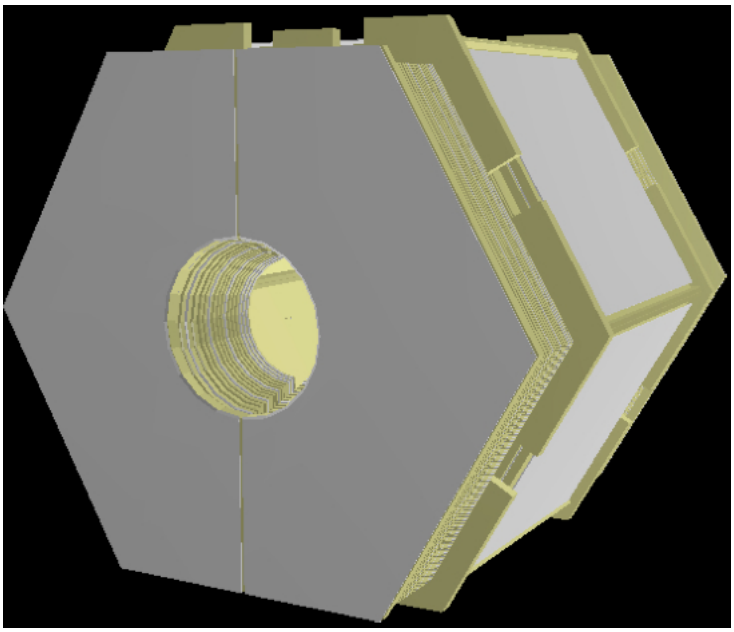

Figure 5.1: *First geometry description of the IFR.*

GEANT4 (GEometry ANd Tracking)[2] : is a toolkit developed in C++ for the simulation of the passage of particles through matter. For the Full Simulation the collaboration has created a framework called Bruno, that is an interface between GEANT4 and ROOT.

GEANT4 permits to specify the geometry of the detector to be studied and the physics processes to simulate, specifying which physics list to utilize which include, for example, electromagnetic processes, hadronic processes and so on. As output of this package used a ROOT file which contains all informations about the interactions between particle and the sensitive detector, for example the deposit of energy, the energy of incident particle, etc.

Naturally the optimization of a detector depends on which physics constraints there are and the optimization of the IFR detector has principally focused on which iron thickness to utilize for having a good muon-ID.

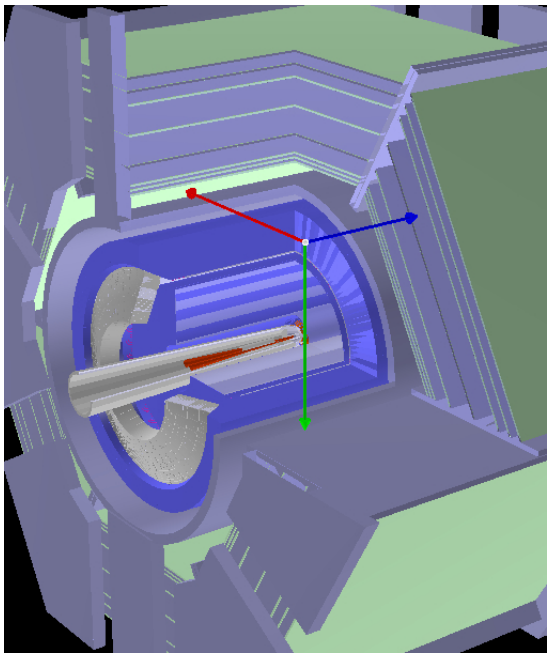

Figure 5.2: *Correct geometry description of the IFR.*

Fig. 5.3 shows a physics process, produced by a muon into the IFR, visible utilizing GEANT4 simulation package.

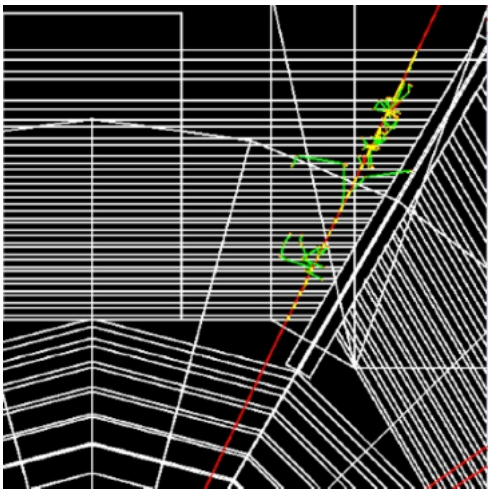

Figure 5.3: *Example of physics process visible with GEANT4 produced by a muon interacting with the IFR.*

ROOT[3] : an object oriented framework for large scale data analysis. Starting from the output of Bruno package the IFR team developed a code, which will be explored in the next section, for extracting physics parameters from simulations useful to optimization of detector and for studying neutron background.

5.2.1 Code structure

The IFR team, as seen previously, has developed a package to analyze all full simulation data for optimizing the detector, in particular to find a good geometry design with a maximum muon-ID and for studying a neutron background rate. Fig. 5.4 shows in detail the structure of this code, starting from Bruno output (Bruno rootple) the data are analyzed in this manner:

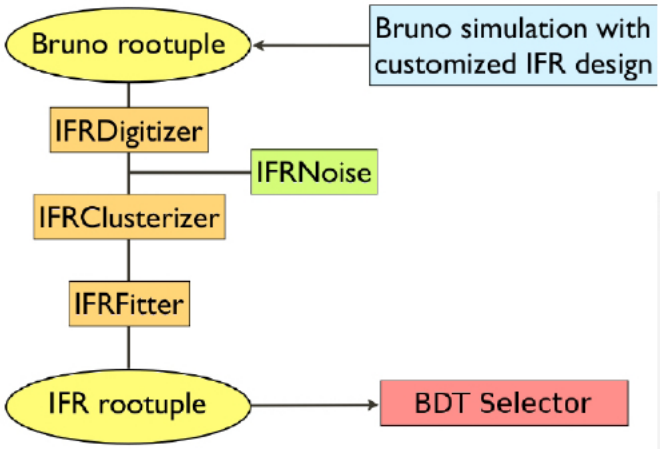

Figure 5.4: *Structure of reconstruction code developed by the IFR team.*

IFRDigitizer: this section of code has the aim to digitize or to collect the GEANT Hits(gHits) with similar features (for example gHits produced by same particle) and to transform these to a new hit that is allocated in the middle of the scintillator bar. In fact to make our simulation more realistic[1], the scintillator layer has been divided into bars 4 cm width, 2 cm height, while the length depends on which layers we consider (if barrel or endcaps). So a Hit represents a signal caused by the passage of a particle due to our detector.

Some conditions to collect gHits must be followed: the layer, the sextant, the layer bar and the type of particle have to be the same, otherwise a new Hit is created.

In Fig. 5.5 it is possible to note the presence of a lot of gHits in a small portion of a scintillator bar, while Fig. 5.6 represents the sextant 1 of barrel not digitized and digitized.

IFRNoise: this code part simulates a random noise in the detector; this must be implemented to simulate more realistic noise.

[1]In our code we have the possibility to set the efficiency of detector, so it is possible that some hits are missed (see Fig. 5.7).

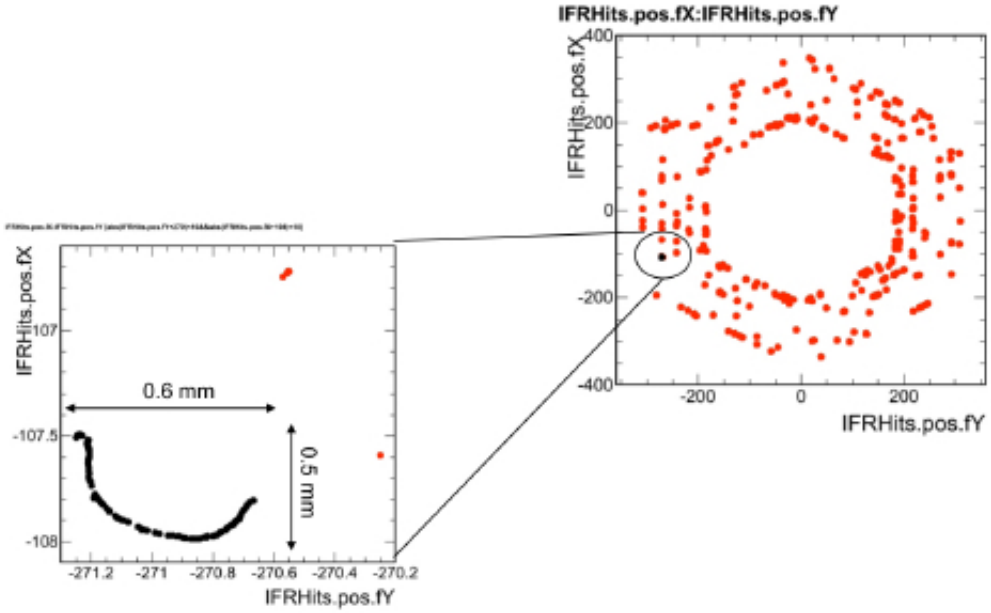

Figure 5.5: *gHits before the digitization.*

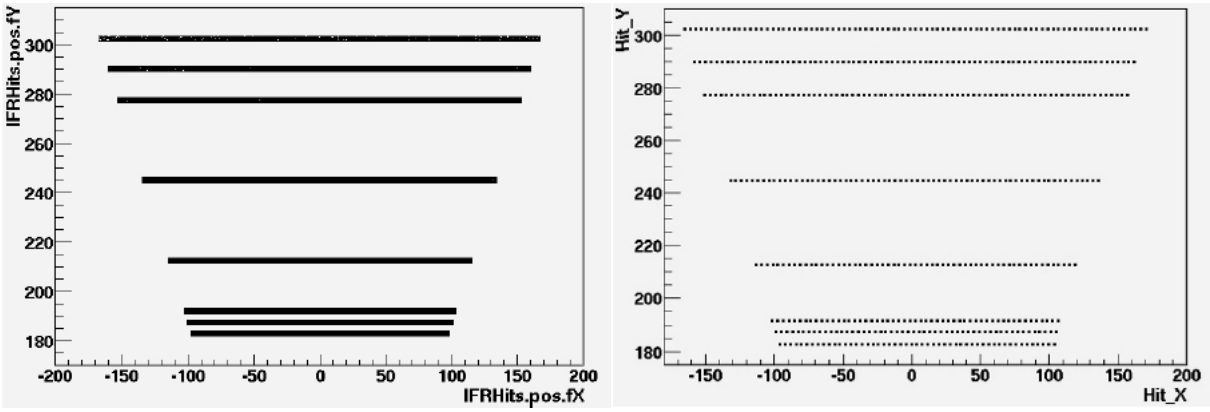

Figure 5.6: *View of sextant 1 not digitized (left) and after the digitization (right).*

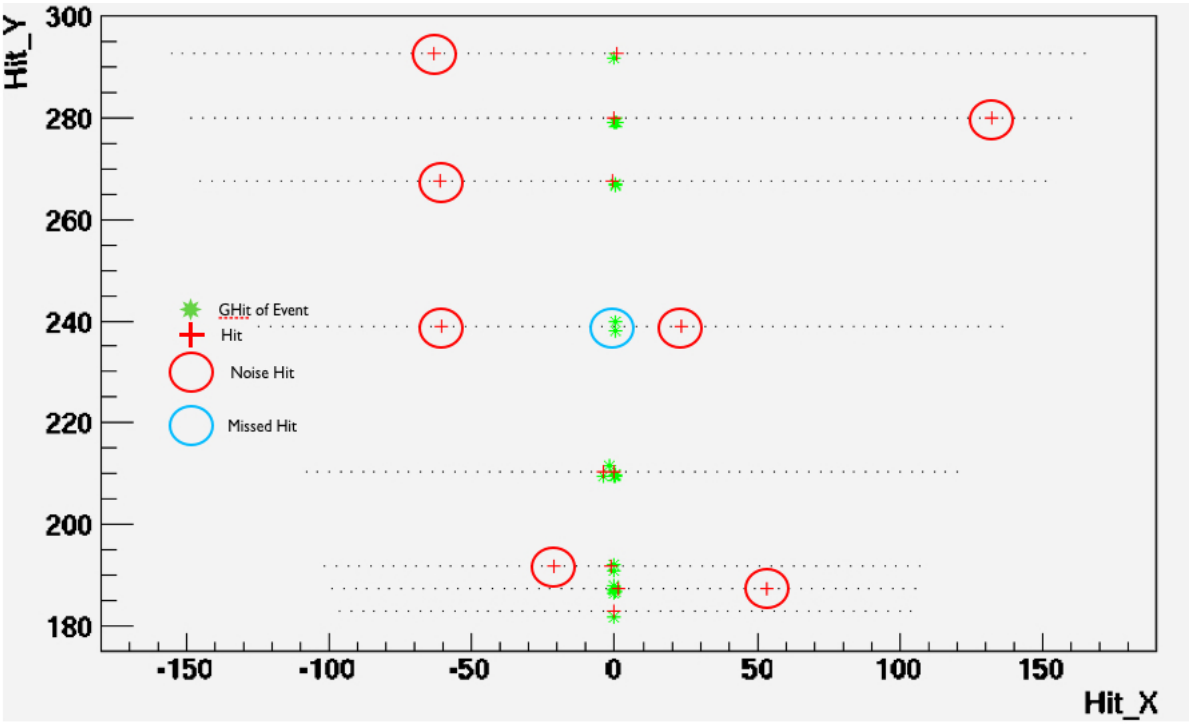

Figure 5.7: *Example of an event not digitized(green) than digitized (red crosses), with some noise hit(red crosses circumscribed) and some missed hits (light blue circumscribed) to simulate detector efficiency.*

IFRClusterizer: this section collects the Hits, in a similar process to digitization, if they are in a same sextant and layer and if the distance along the z axis is less than 34cm ($\sim$ 2ns of resolution). Two or more neighboring Hit are assembled also if the distance along the x axis is less 4cm. Fig. 5.8 illustrates the process of clusterization.

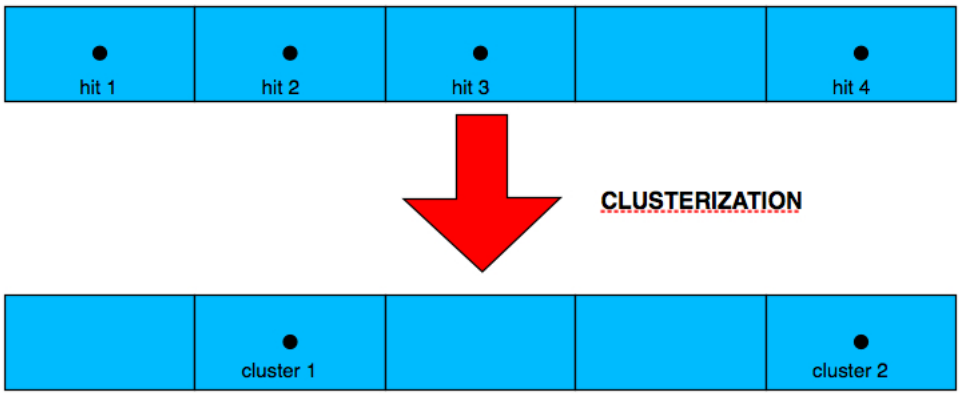

Figure 5.8: *Clusterization process for the IFR detector.*

IFRFitter: this package component fits linearly the track[2], calculating the χ^2 and the

[2]In our description and simulations the magnetic field has been turned off for simplicity.

hits residue distribution. In this step the fit is calculated with respect to the directions given by the MCTruth.

The output of this package is an other ROOT file, which contains all relevant informations about hits, clusters and tracks (see Fig. 5.9), that can be used for muon-ID utilizing a BDT (Boosted Decision Tree, see next sections) selector.

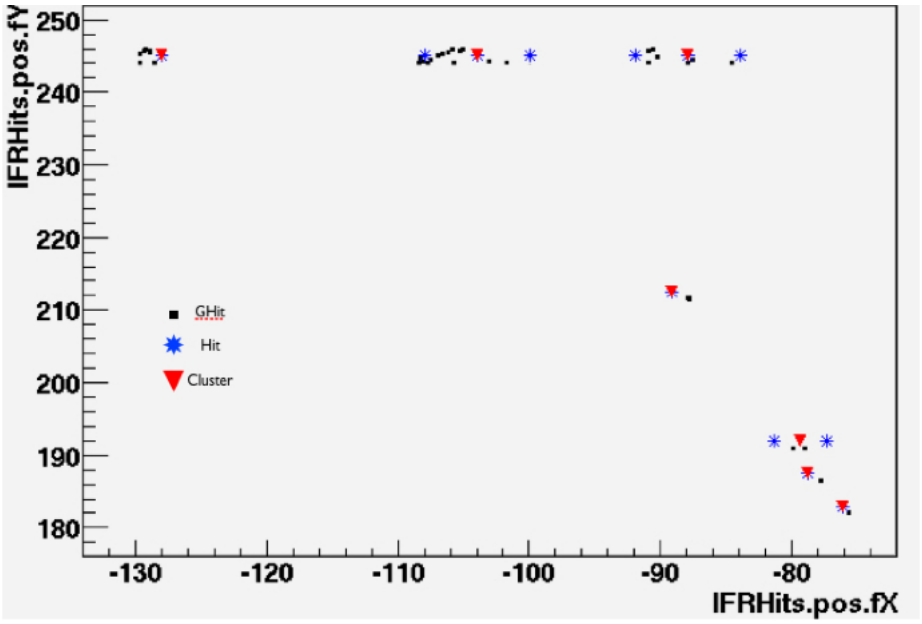

Figure 5.9: *Example of event not digitized (black) than digitized (blue) and clustered (red)*

5.2.2 Studies on hadronic showers

The main subject of this study is to analyze the propagation of an hadron, in particular we will utilize pion, in the IFR detector and to find some different useful physics parameters to have good muon identification with low pion contamination:

- the position where pions are approximately stopped (this is useful for example for studying the muon-ID behaviour if inserting another layer before this position);
- the total iron thickness to contain hadronic shower;
- the dependance of hadronic shower propagation from different physics list;
- the differences between pions and muons, to select helpful variables for muon-ID.

The study of hadronic showers has been optimized using a 500.000 pions events directed to sextant 1 in an energy range 0.5 - 5 GeV. In the reconstruction code, as seen previously, there are some interesting variables useful for this study:

- **InteractionLength** the interaction length[3] of a track: for each track linearly fitted, from first layer to last layer hit we calculate the corresponding interaction length summing the passage through the iron and the scintillator;
- **LastLayer** the last layer of the sextant hit by an event;
- **MoltMean** is the number of hits collected to create a cluster;
- **MoltHitMean** is the number of gHits (GEANT Hits) gathered to produce a hit.

Obviously the pion, and in general all hadron, hitting the IFR detector can create an hadronic shower with a lot of hits in our detector, while muons, whose passage is approximately linear, have fewer hits. This is illustrated in Fig. 5.10, which shows the response of the IFR to a hadronic shower, and Fig. 5.11, which shows the response to a collimated muons.

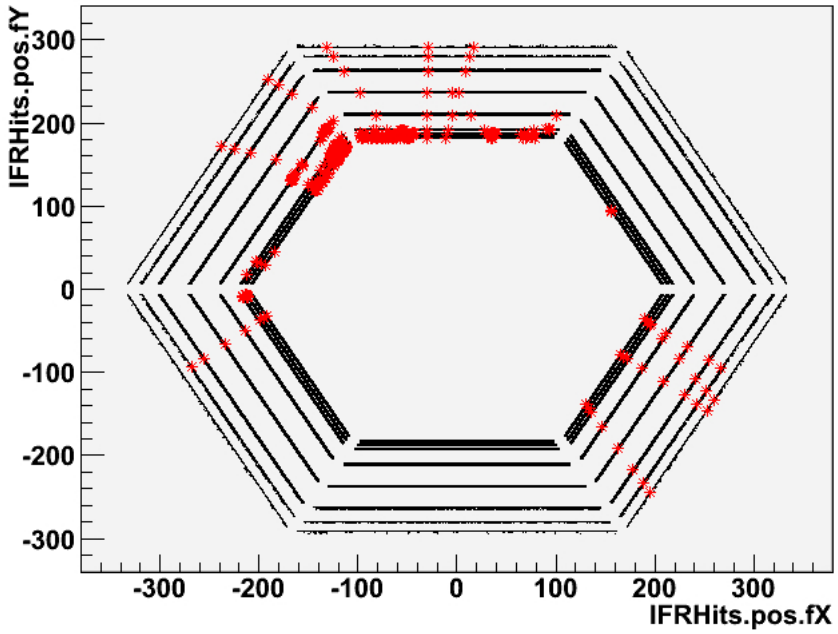

Figure 5.10: *GEANT Hits of 200k pion event (black) collimated to one sextant and GEANT Hits of event # 5 (red).*

One of the main goals of this study is to research the behaviour of hadronic shower with different physics lists, those listed in Paragraph 4.2.1, not in order to find the physics list which gives us the best results but to learn how a chosen physics list can have impact on the results. For simplicity we identify the three physics list (QGSP, QGSP_BERT and QGSP_BERT_HP) as physics list with low precision, intermediate precision and

[3]The mean free path length required to reduce the energy of particle by a factor $1/e$

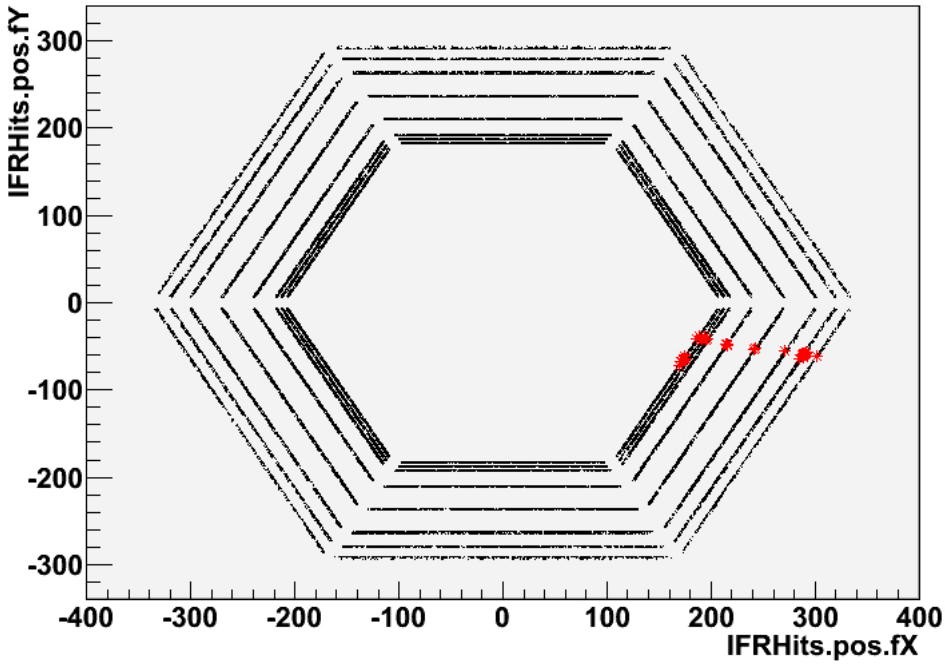

Figure 5.11: *GEANT Hits of 200k muon event (black) collimated to one sextant and GEANT Hits of event # 5 (red).*

high precision respectively. For example Fig. 5.12 shows the normalized distribution of pion interaction length with different physics lists; it is possible to note as increases the precision of list, as the distributions of the interesting variables listed previously have an expected behaviour, with a decrease of the first peaks of distribution and an increase of the last ones. This is the signal that the propagation of hadron into the detector depends on list precision and is crucial, during the optimization of detector, to select which physics list has a good compromise between simulation[4] time and expected results.

Starting from interaction length differences, it is conceivable to study other variables, for example **LastLayer**: seen the behaviour of interaction length augmenting the precision of physics list, we expect the same response in the LastLayer, so increasing the precision have to increase the number of particles hit an high number of layer: this sentence is verified in Fig. 5.13.

From these figures it is obvious to deduce that as the precision of physics list increases the width of the hadronic shower becomes larger. In fact if we plot the **MoltMean**, Fig. 5.14 the distribution of this quantity is wider for intermediate and high precision physics lists. The same behaviour it is possible to be seen in the Fig. 5.15, Fig. 5.16 and Fig. 5.17 where as precise is the physics list as the hadronic shower is more penetrant.

[4]The simulation time depends on precision of physics list, in particular for the QGSP_BERT_HP is high

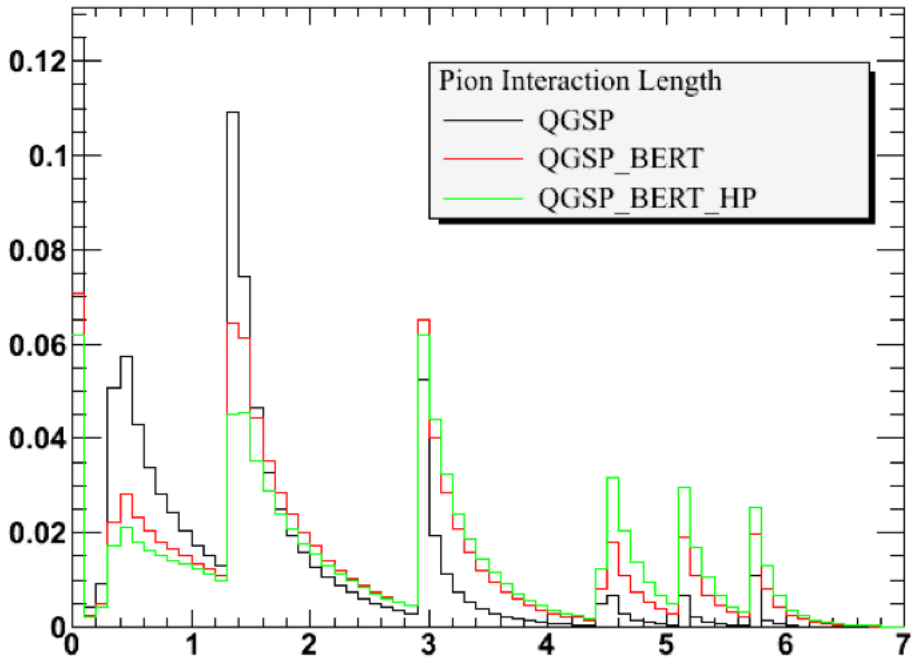

Figure 5.12: *Interaction Length distribution for low (black), intermediate (red) and high (green) precision physics list.*

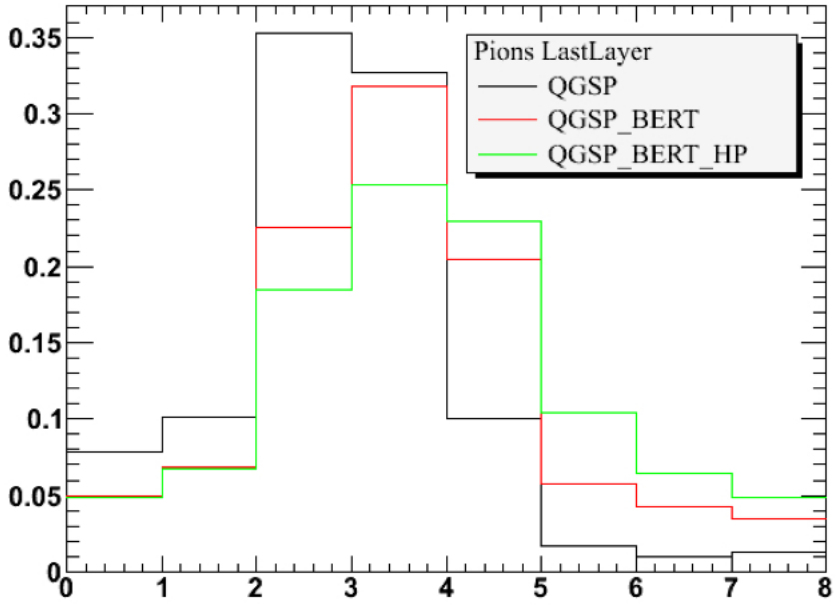

Figure 5.13: *GEANT Hits of 200k muon event (black) collimated to one sextant and GEANT Hits of event # 5 (red).*

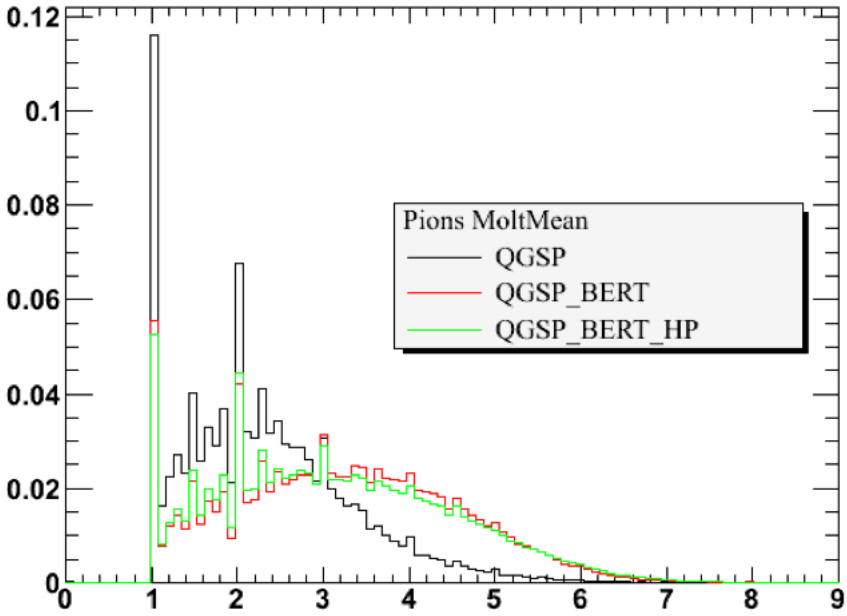

Figure 5.14: *Distribution of number of hit collected to create a cluster (MoltMean) for low (black), intermediate (red) and high (green) precision physics list.*

5.2.3 Muon identification and pion rejection

One of the main focus of this thesis is to study the muon identification and pion rejection of our detector, using different iron thickness to evaluate which thickness of iron gives us the best results. For conducting this study we considered a sample of ∼5M muons and pions[5], using a **Boosted Decistion Tree** analysis technique[6].

This technique is a type of multivariate analysis represented by Fig. 5.18: starting from **root node**, a sequence of divisions is applied using a discriminant variable x_i, which can be the same at each node or can be change in order to distinguish the signal S from background B. The signal and background data samples are divided into two parts: one is used for the training step, where cuts on variables are optimized in order to maximize the signal over the background, and one for testing cuts optimized.

In our study, to calculate the muon-ID, we use muons as signal and pions as background and we utilize, for discriminating muons from pions, some of the variables listed in the previous paragraph. Obviously the behaviour of muons and pions is different, because the pion can create an hadronic shower inside the IFR detector, so we expect, for example, larger distribution of multiplicity of cluster and hit. Looking at Fig. 5.19 and 5.20 we note differences between muons and pions we expect:

[5]In GEANT4 it is possible to choose which particle to shoot to a detector. In our case we launched muons and pions to the IFR detector.

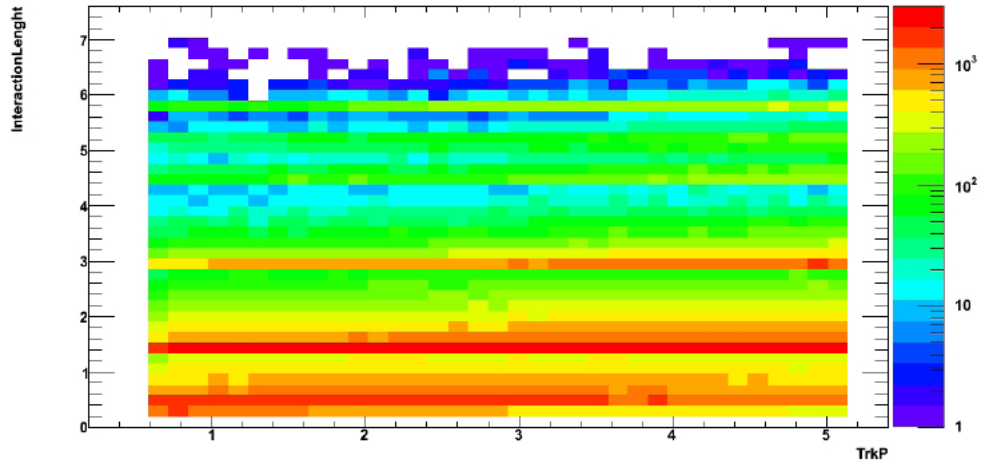

(a) Low precision

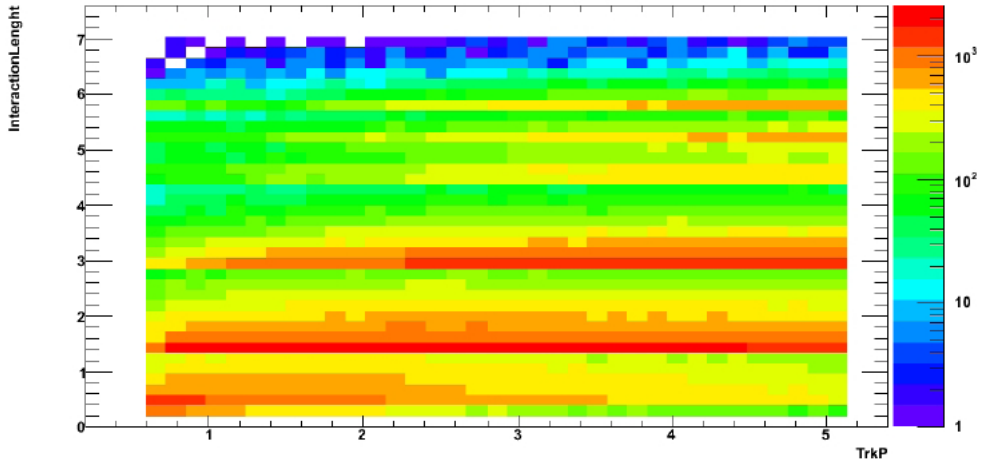

(b) Intermediate precision

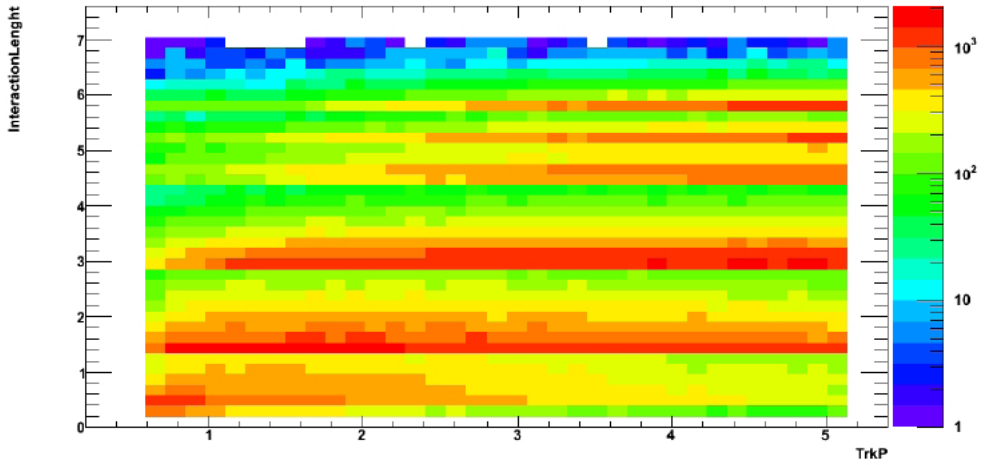

(c) High precision

Figure 5.15: *Dependence of pion interaction length from track momentum.*

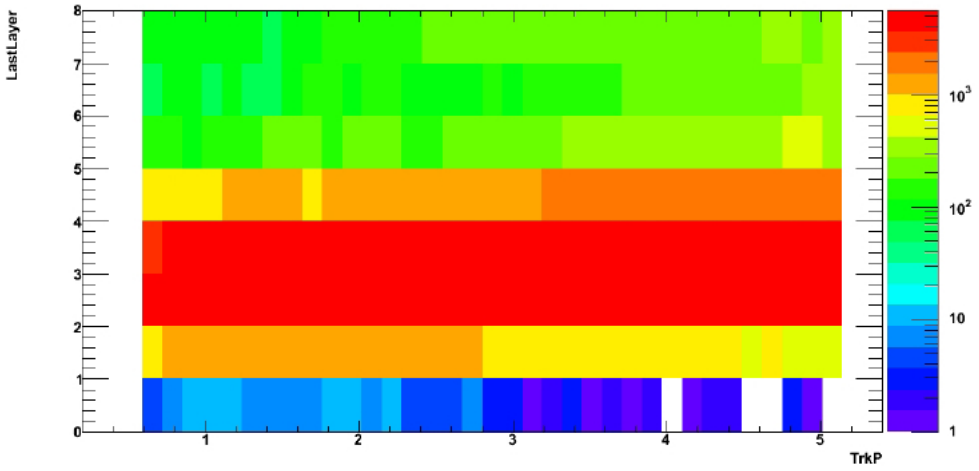

(a) Low precision

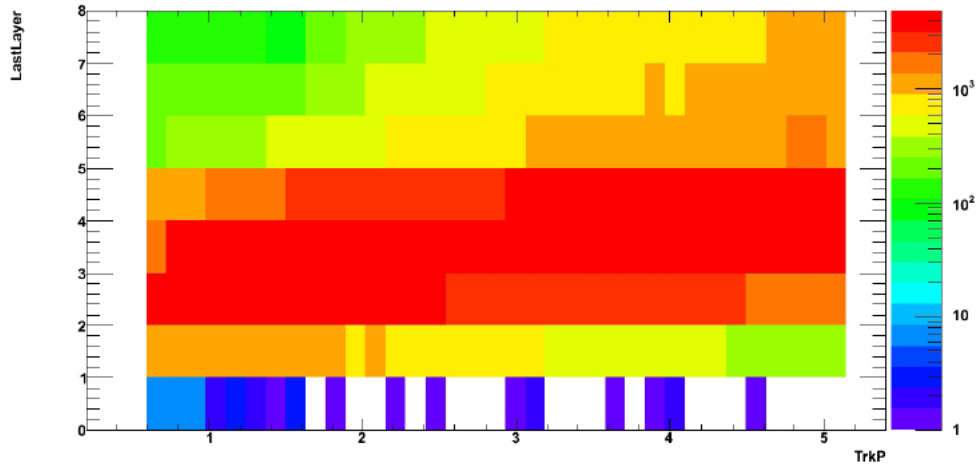

(b) Intermediate precision

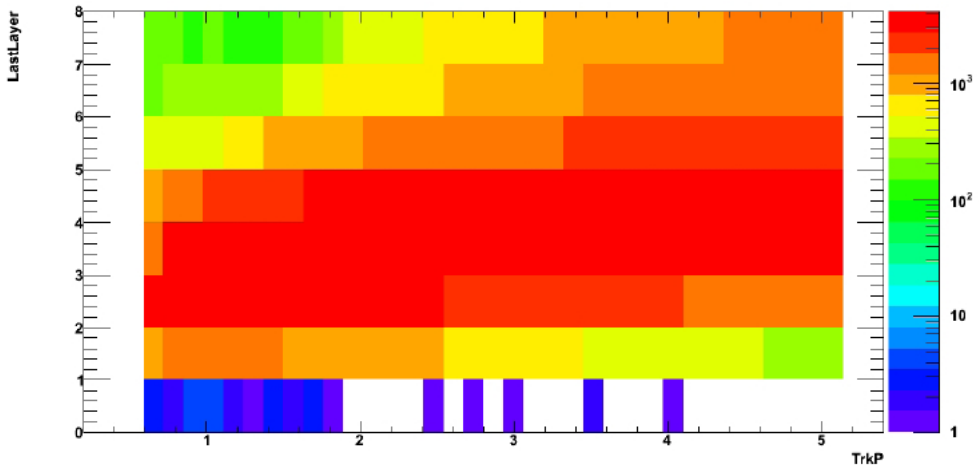

(c) High precision

Figure 5.16: *Dependence of pion last layer hit by a track from track momentum.*

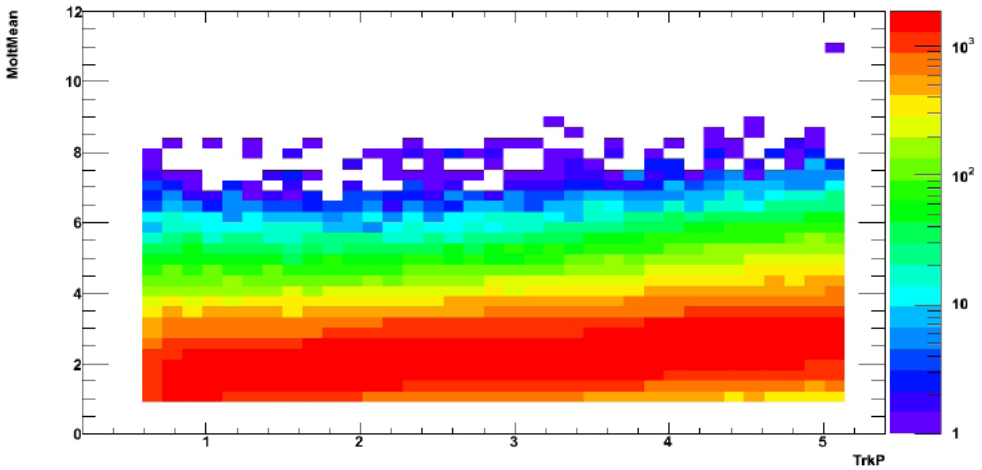

(a) Low precision

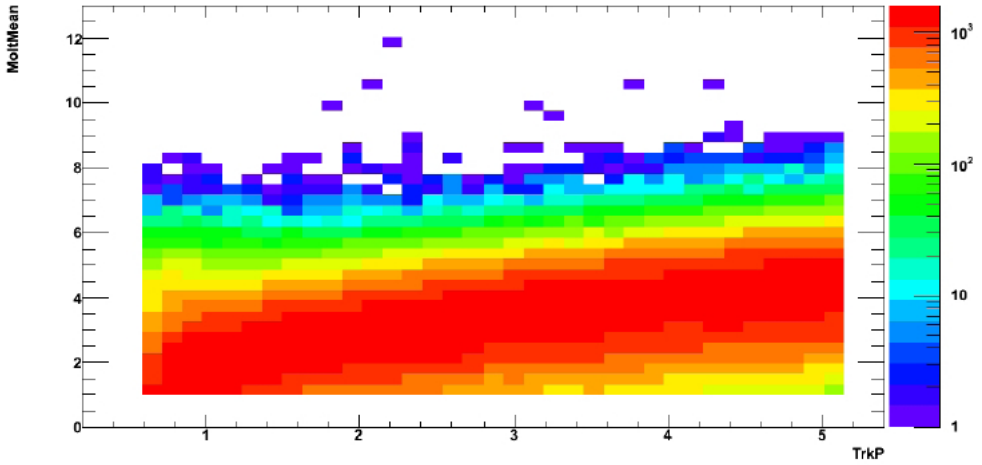

(b) Intermediate precision

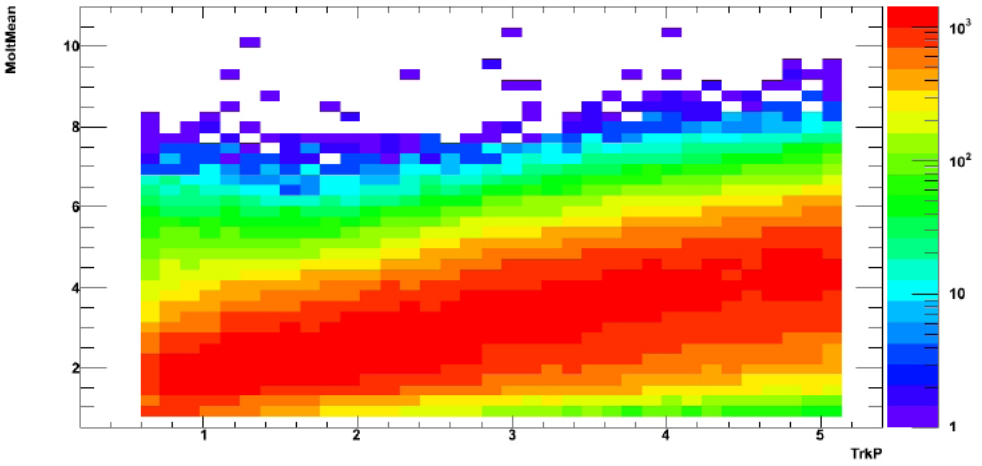

(c) High precision

Figure 5.17: *Dependence of pion cluster multiplicity from track momentum.*

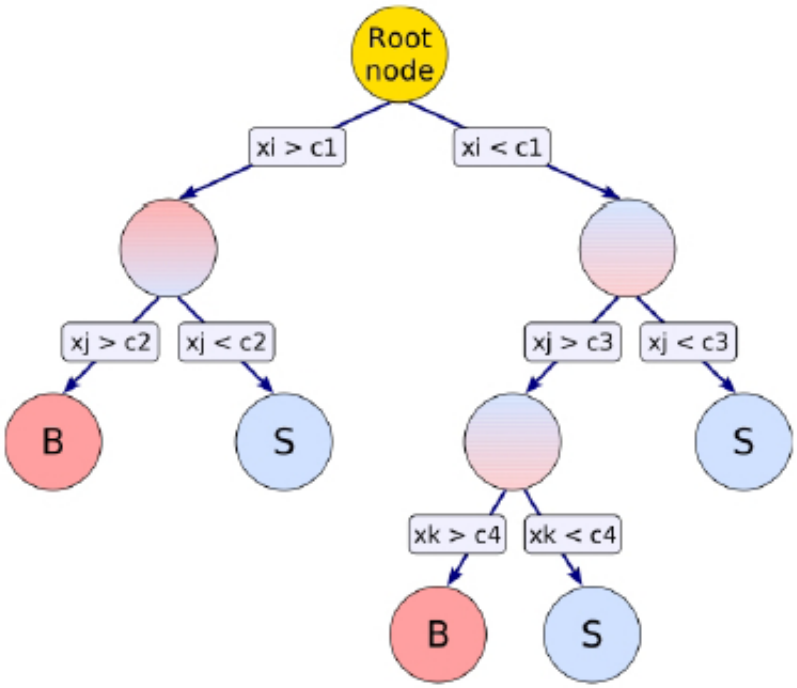

Figure 5.18: *Boosted Decistion Tree scheme.*

- Pions producing hadronic shower can be stopped before the last layer, so the distribution will not be peaked at the allowed higher interaction length; on the other hand muons hit all layers and the interaction length for these particles is peaked at the interaction length permitted by our detector.

- Same behaviour seen for the interaction length occurs analyzing the last layer hit by a track: in fact with the hadronic shower it is possible that the particle is stopped not at the last layer, like muons, but at intermediate layers.

For completeness plots of variables studied for pions(Fig. 5.15,5.16 and 5.17), have been presented here(Fig. 5.21,5.22 and 5.23) and there are only few changes between physics list, in fact it is what we expect because the only difference between physics list, as seen previously, is the precision used to describe the hadron physics.

The distribution of these variables are very different for pions and for muons, therefore they can be used to distinguish muons from pions using the BDT technique.

Different iron thickness

One of the crucials question of the IFR team is what iron thickness could be the best for the muon identification. Starting from the Conceptual Design Report (which shows an IFR iron thickness of 920 mm, Tab. 3.1), other configurations(620mm of iron, 820mm

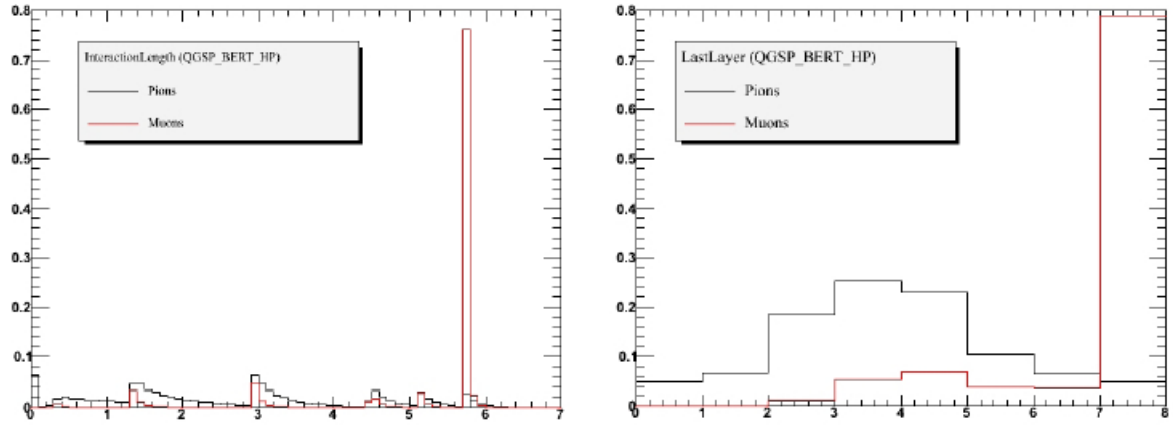

Figure 5.19: *Interaction length(left) and last layer hit(right) distribution for muons(red) and pions(black) for the high precision physics list .*

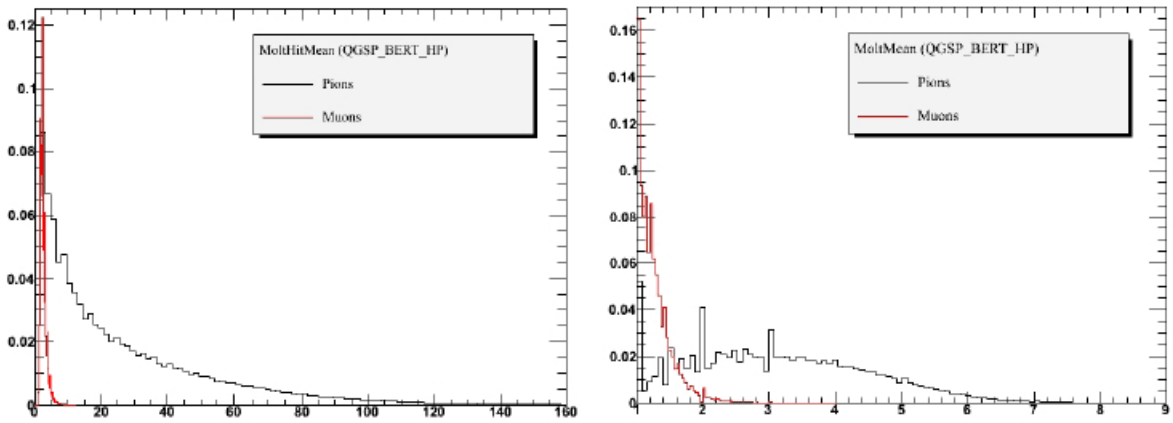

Figure 5.20: *Hit(left) and cluster(right) multiplicity distribution for muons(red) and pions(black) for the high precision physics list.*

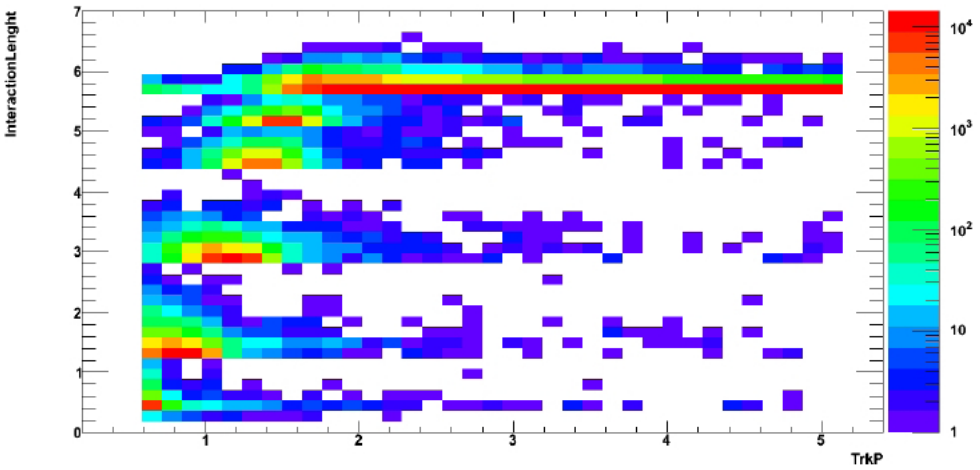

(a) Low precision

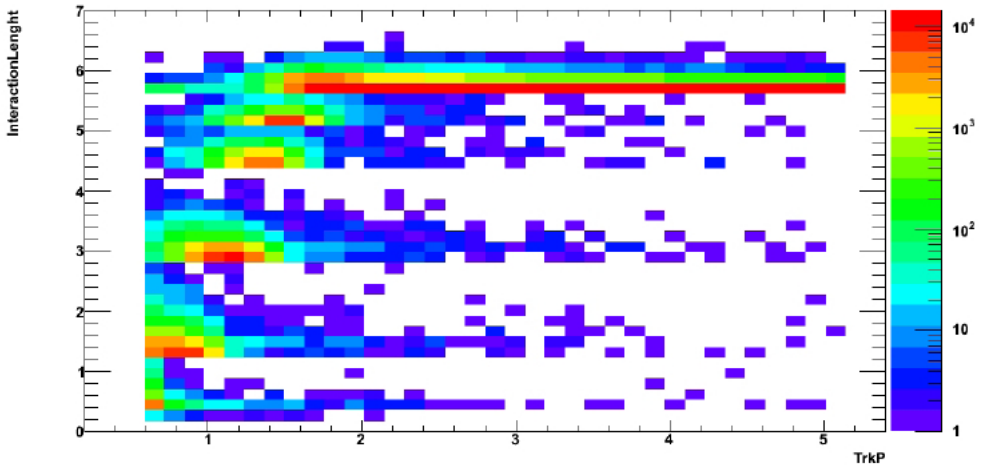

(b) Intermediate precision

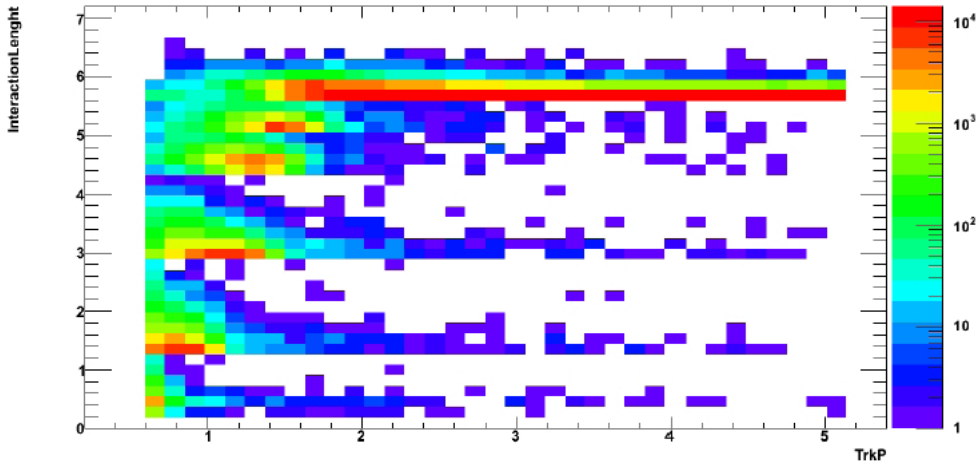

(c) High precision

Figure 5.21: *Dependence of muon interaction length from momentum track.*

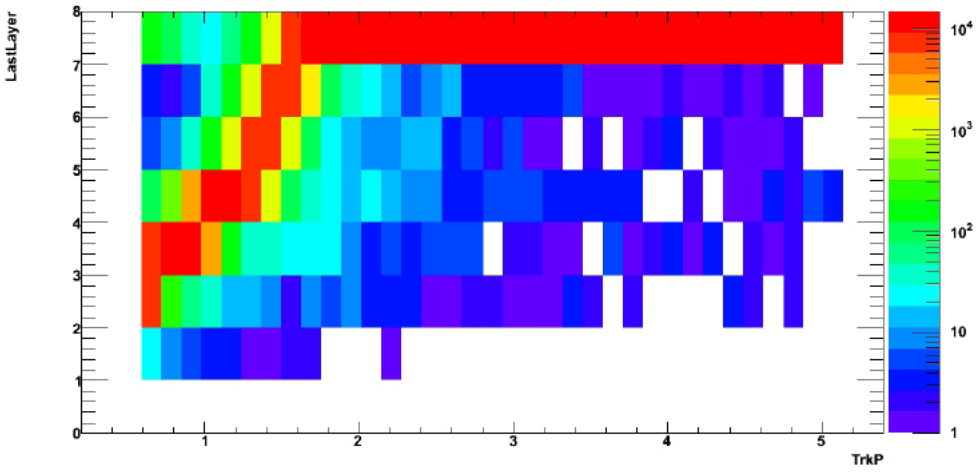

(a) Low precision

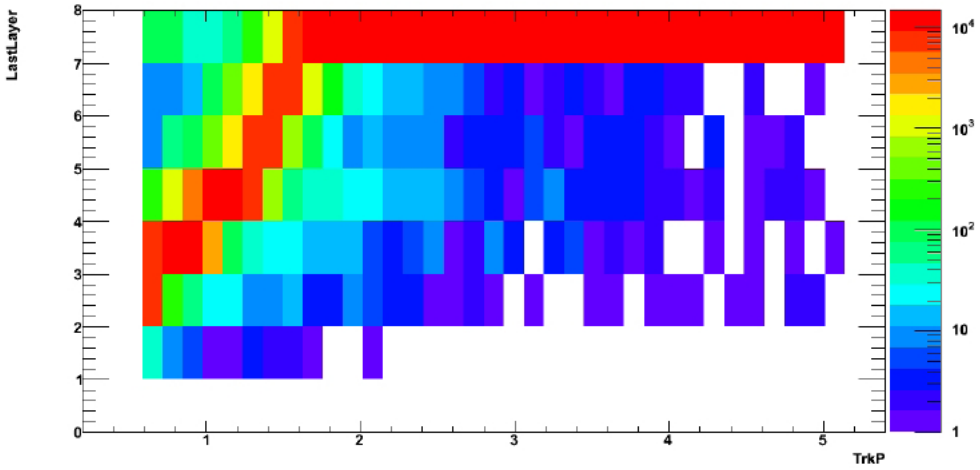

(b) Intermediate precision

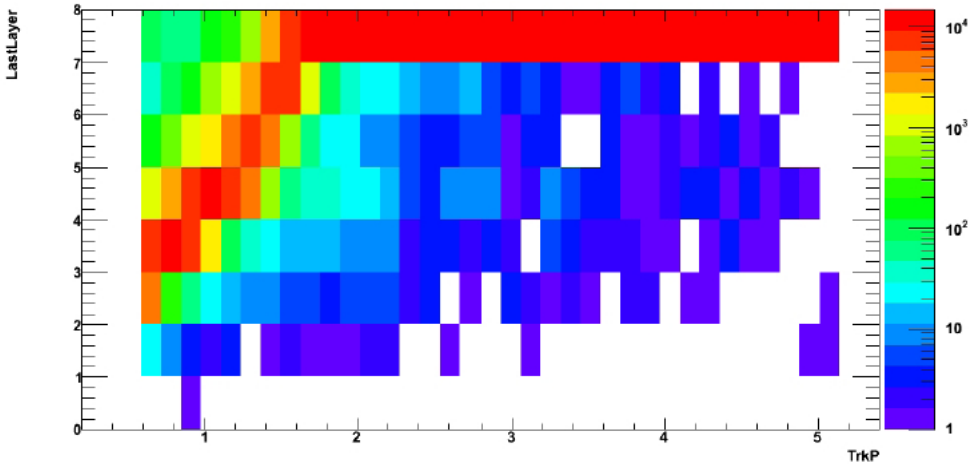

(c) High precision

Figure 5.22: *Dependence of muon last layer hit by a track from momentum.*

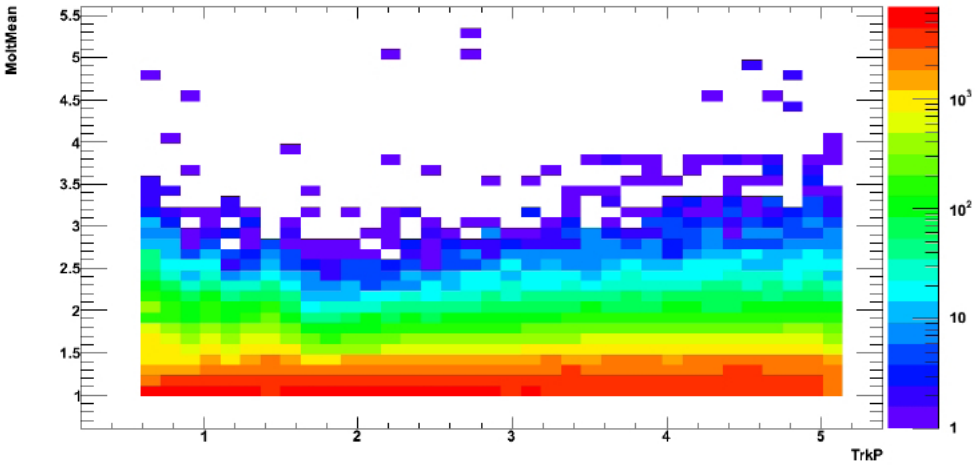

(a) Low precision

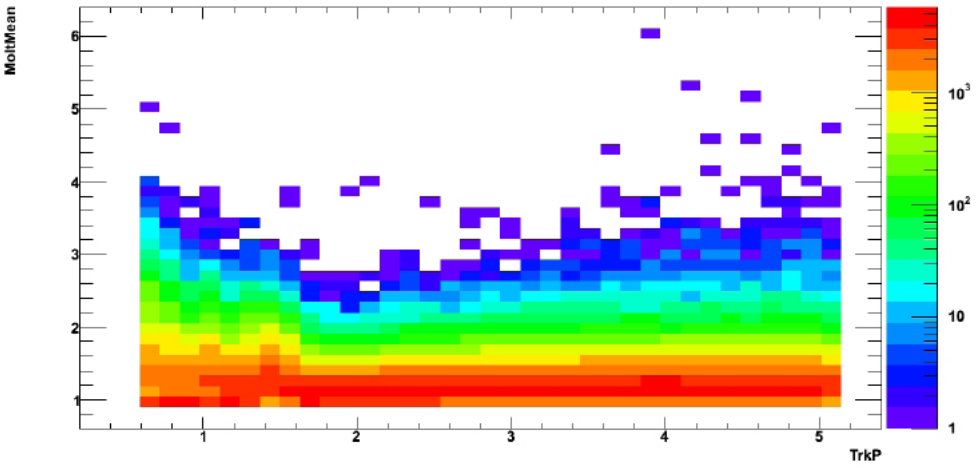

(b) Intermediate precision

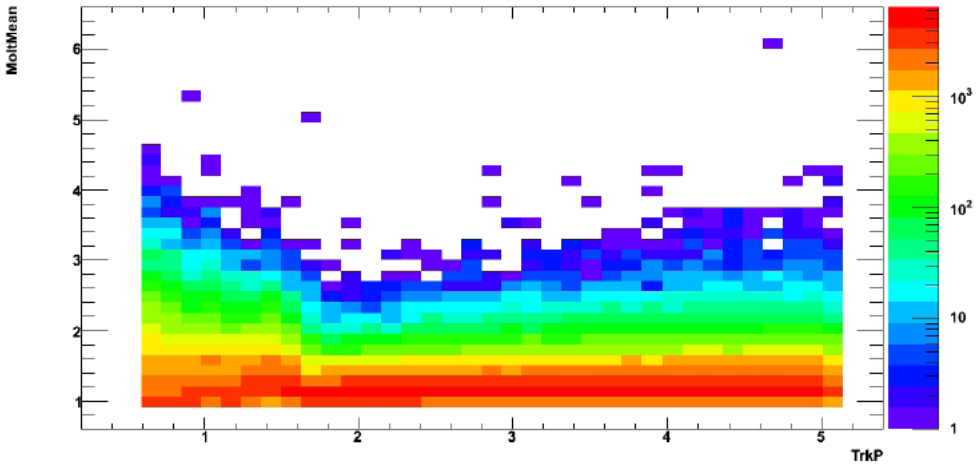

(c) High precision

Figure 5.23: *Dependence of muon cluster multiplicity from momentum track.*

and 920mm with different layer thickness with respect to the CDR one) have been tested to evaluate the detector performances for different thickness:

- **620mm of iron(C14):** the total thickness of iron is 620mm and the stratigraphy of the detector is |-2-|-2-|-12-|-12-|-12-|-12-|-10-|;
- **820mm of iron(C13):** the total thickness of iron is 820mm and the stratigraphy of the detector is |-2-|-2-|-16-|-16-|-16-|-16-|-14-|;
- **920mm of iron(C2'):** the total thickness of iron is 920mm and the stratigraphy of the detector is |-2-|-2-|-16-|-24-|-24-|-14-|-10-|;

where the | means the scintillator layer and -2- the iron thickness of 2cm in this case. Results are shown in Fig. 5.24, where the configuration with 920mm of iron has higher curve, so it is the one that gives a higher muon efficiency at fixed pion contamination. In order to understand if actually this geometry configuration is the best in all momentum ranges, we fix a pion contamination and we evaluate the muon efficiency for different momentum ranges.

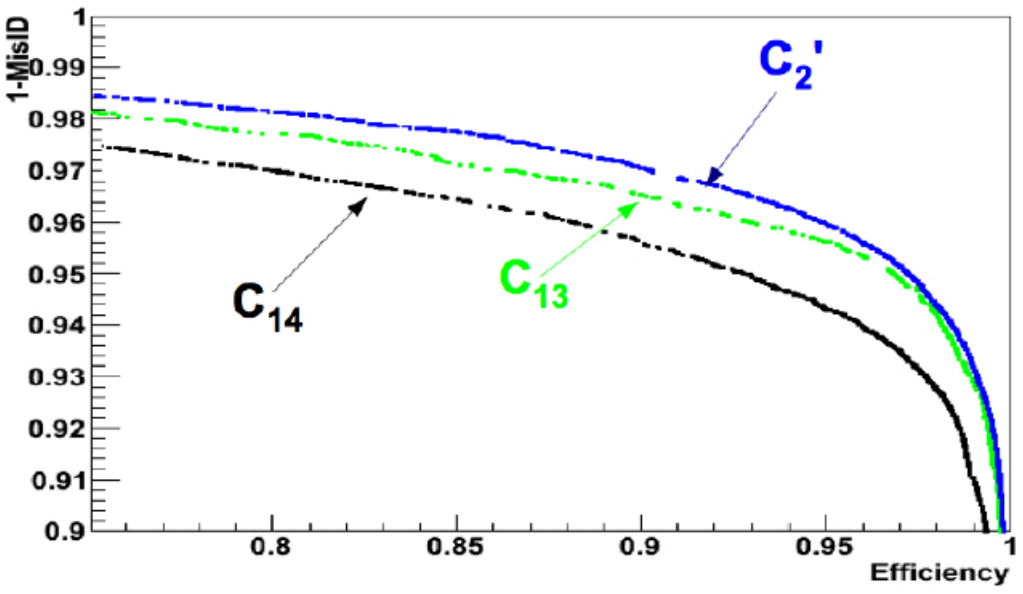

Figure 5.24: *1-MisID versus Efficiency plot for different geometry configurations: C14(620mm), C13(820mm) and C2'(920mm).*

This study is reported in Fig. 5.25, where it is possible to observe the C2' configuration, with 920mm, that has been just considered the best, is not the best: in fact at low momentum (less than 1.5 GeV/c) where the best one is that with 620mm of iron.

Above 1.5 GeV/c C2' is the best configuration, with an efficiency more than 90%: this is a very good result, it means that the geometry design chosen for the Conceptual Design Report has a good efficiency and this is a good starting point.

Furthermore it must be noted that to calculate the muon efficiency only the IFR has been utilized, so probably using all SuperB detectors the muon efficiency in the momentum range below 1.5 GeV/c could be improved.

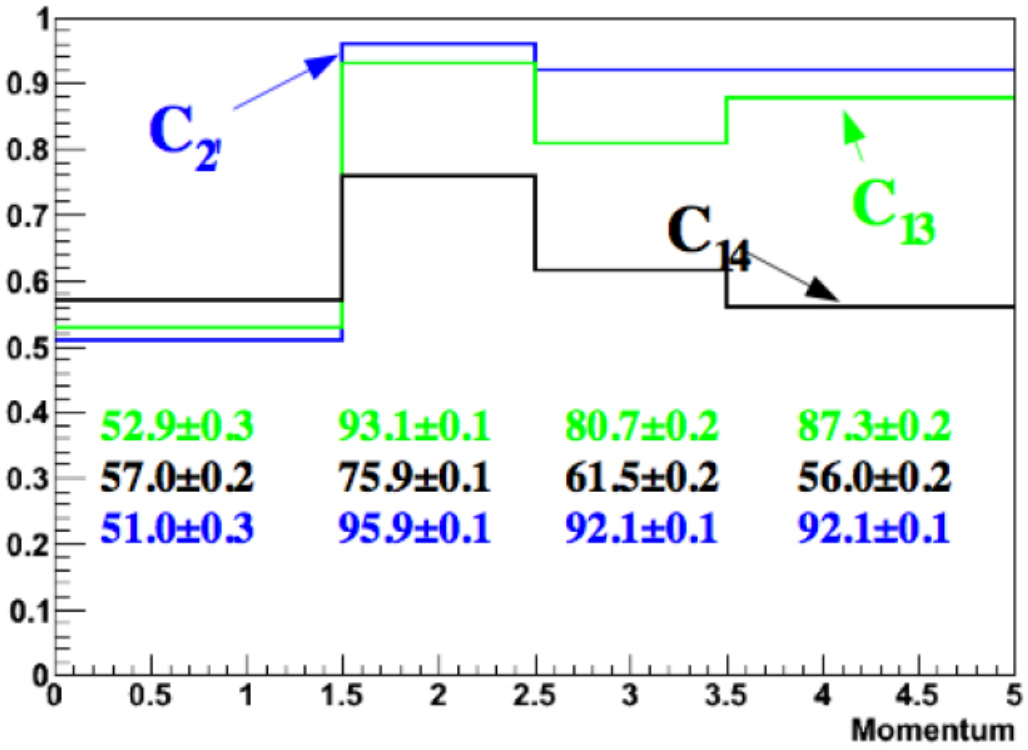

Figure 5.25: *Muon Efficiency as function of momentum (GeV/c) , with fixed pion contamination at 2%, for different iron thickness: C14(620mm), C13(820mm) and C2'(920mm). The numbers in the figure are the muon-identification efficiency for each momentum range.*

An other study done has been to evaluate the muon efficiency with the addition of 1.5% of noise and with a fixed detector efficiency of 95%, in order to understand how the noise affects the efficiency: this noise value and detector efficiency should be the ones expected for the IFR detector.

Naturally the addition of random noise and the decreased detector efficiency affect the muon identification, see Fig. 5.26, at low momenta but for high momenta there are no changes.

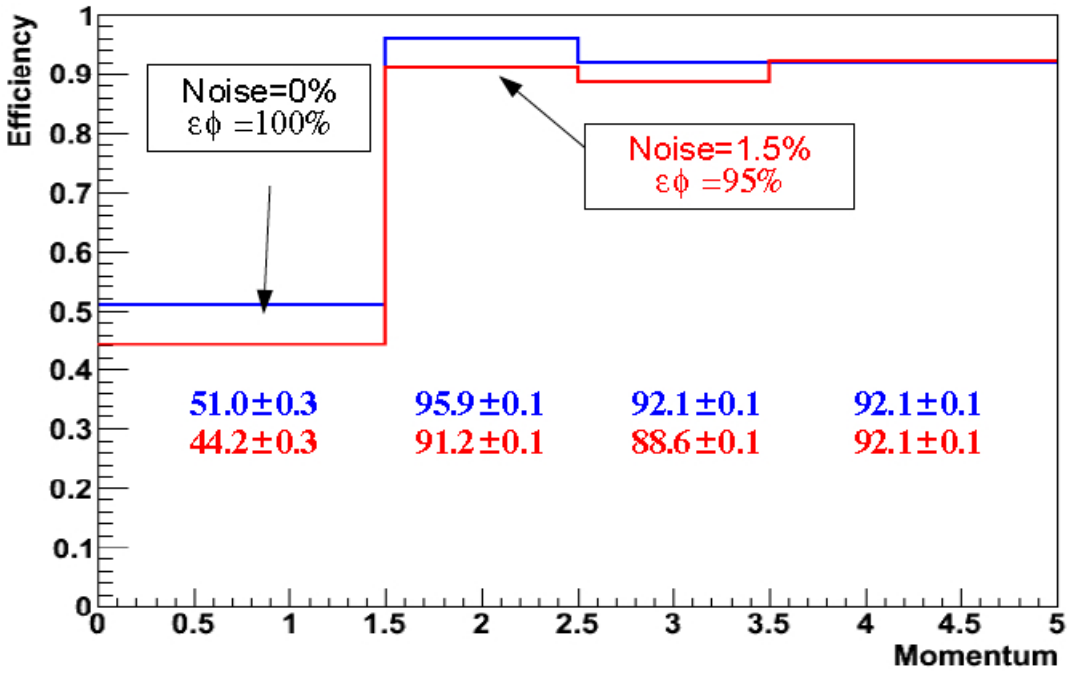

Figure 5.26: *Muon Efficiency as function of momentum (GeV/c) , with fixed pion contamination at 2%: blue line stands for the detector without noise and 100% efficiency, red line represents the detector with 1.5% of noise and 95% of efficiency.*

Addition of another layer: 9 scintillator layers

Another test conducted to evaluate the performances of the IFR detector, has been to verify if the addition of a scintillator layer, so having 9 layers, there are significant improvements on muon identification. With this geometry configuration (|-2-|-2-|-12-|-12-|-16-|-24-|-14-|-10-|), so with 9 layers of scintillators and a total amount of iron thickness equal to 920mm, the results shown in Fig. 5.27 are obtained: no significant improvements we obtained on muon identification. However this configuration might be better for K_L reconstruction.

5.2.4 Physics list studies

With the help of the full simulation, another study has been done to verify the impact of different physics list on muon identification. The subject of this work is not to find the physics list which gives the best muon-ID but to know how a physics list can affect the identification of muons and to find which physics list gives results enough realistic and is, from point of simulation time, reasonably fast.

In this study, using the **BDT** technique, the background rejection versus efficiency curve has been compared, in different momentum ranges (Fig. 5.28).

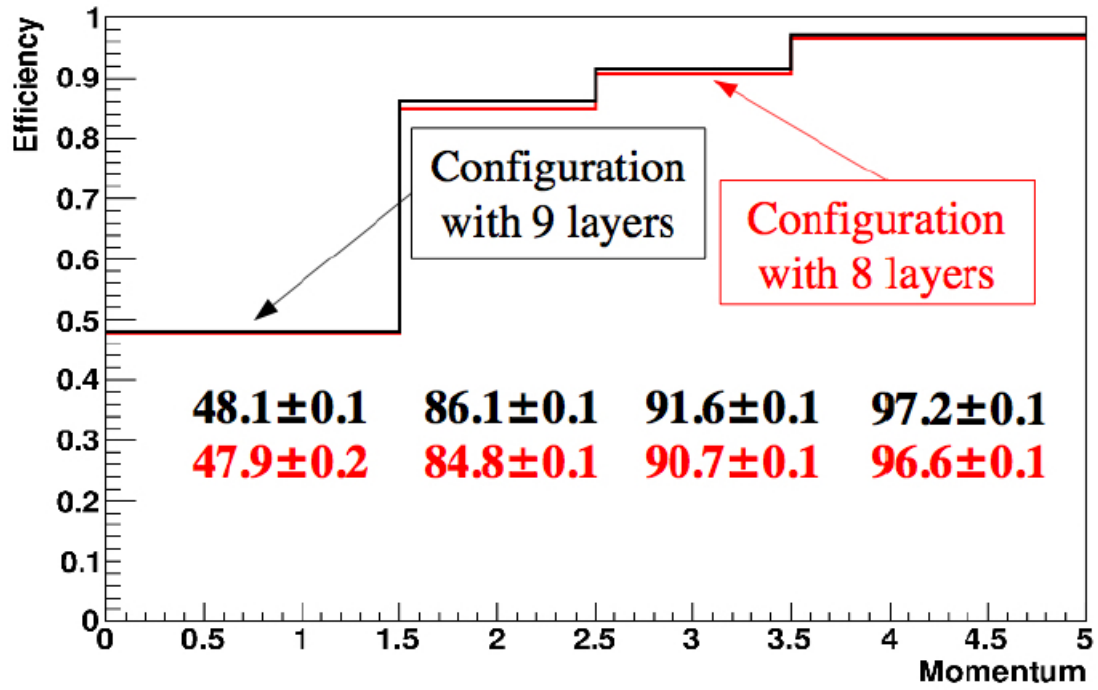

Figure 5.27: *Muon Efficiency as function of momentum (GeV/c) , with fixed pion contamination at 2%: black line represents the 9 scintillator layers geometry configuration while the red one the 8 layers.*

This preliminary study has been conducted analyzing a data sample of 500k muons and pions, using a geometry configuration with 8 layers and 920mm of iron thickness. In order to have more precise results a larger data sample is needed.

Figure 5.28: *Background rejection versus efficiency for different track momentum ranges.*

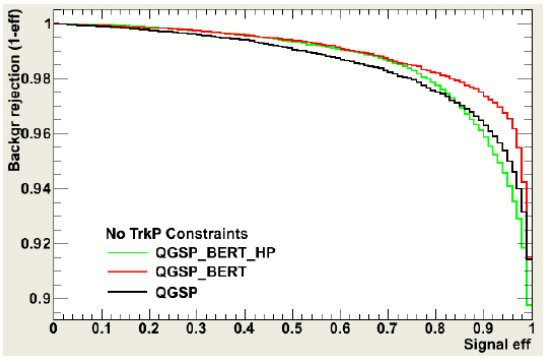

(a) Background rejection versus efficiency for muon identification for different physics list and without momentum constraints.

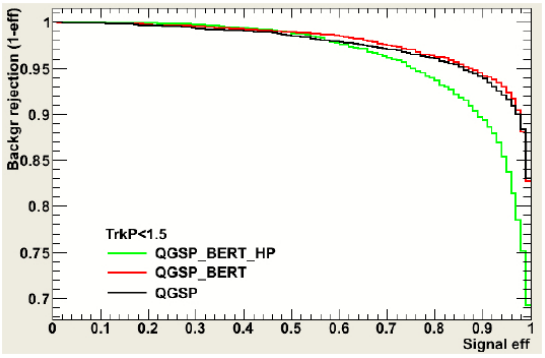

(b) Background rejection versus efficiency for muon identification for different physics list and with momentum less than 1.5 GeV/c.

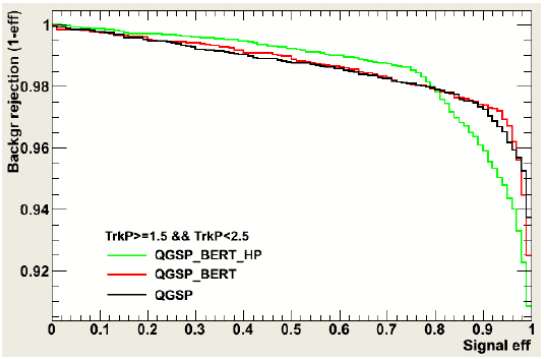

(c) Background rejection versus efficiency for muon identification for different physics list and with momentum track more than 1.5 GeV/c and less than 2.5 GeV/c.

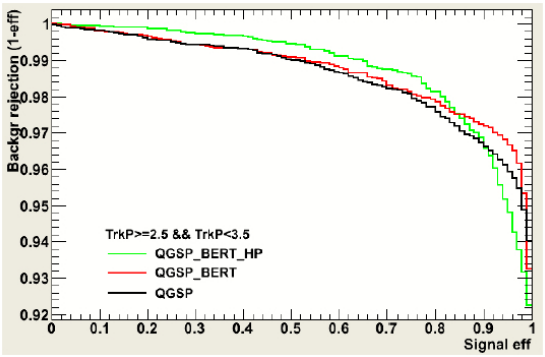

(d) Background rejection versus efficiency for muon identification for different physics list and with momentum track more than 2.5 GeV/c and less than 3.5 GeV/c.

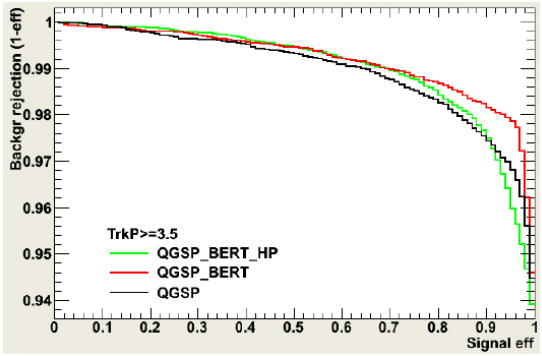

(e) Background rejection versus efficiency for muon identification for different physics list and with momentum track more than 3.5 GeV/c.

Chapter 6

Prototype

The construction of the prototype is one of the principal milestones of an experiment and during there three years, as seen in the previous chapters, an extensive R&D activities have been done and the prototype consists of 8/9 layers of scintillators within an iron structure, with three WLS (Wave Length Shifter) fibres inside the scintillators for carrying out the signal to Silicon Photo Multipliers (see Chapter 3).

Fig. 6.1 shows the prototype iron structure: this consists of 11 iron layers and inside the gaps it is possible to put in the scintillator layers, studying different geometry configurations (different number of layers or distinct iron thickness between sensitive detector).

In next paragraphs a detailed description of prototype will be given and preliminary results from the first test at Fermilab will be shown.

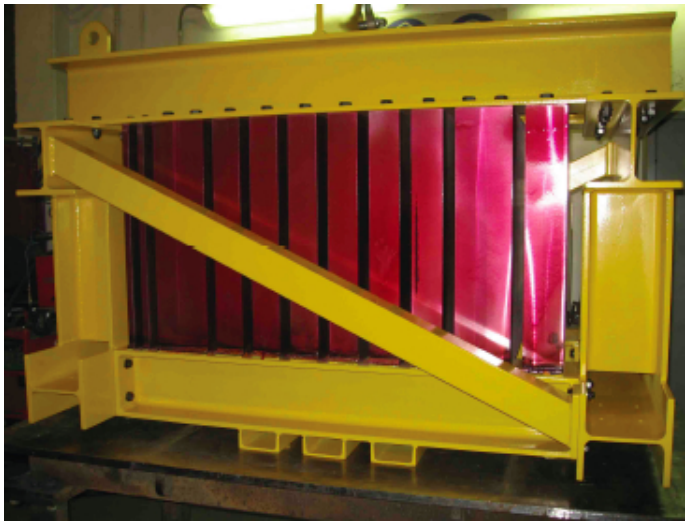

Figure 6.1: *Picture of the prototype iron structure.*

6.1 Prototype features

As seen in Sec. 3.1.2, the prototype consists of a 60×60×92 cm^3 of iron with 3 cm gaps for the active layers and of 9 readout layers of different kinds: 4 with Time readout (TDC) and 5 with Binary readout (BiRo)[1], with a total amount of 112 and 125 channels of electronics respectively.

Active layers are located within light tightened boxes, called Pizza Boxes, made by aluminum, and each scintillator bar has inside 3 optics **WLS** fibres, shown in Fig. 6.5, terminating with a Silicon Photo Multiplier(SiPM) of different geometry (see Fig. 6.3). So each Pizza Box has inside a series of scintillator bars, BiRo has two layers of scintillator bars, which carry out the signal to two SiPM (only one if BiRo), one at left and one at right of the bar.

Fig. 6.2 shows some pizza boxes features, in particular dimensions and the layouts of the two readout methods.

In this prototype different diameters of fibre have been used coupled with different SiPM geometry, in particular:

- 1.2×3.2 mm^2 to be coupled to 1.0 mm fibres;
- 1.4×3.8 mm^2 for 1.2 fibres;
- array of 3 round sensors ϕ =1.4mm, for 1.0 mm and 1.2 mm fibres.

Constructing the prototype, the main idea was to test all reasonable combinations between different SiPMs, different optics fibres and readout type. In particular 12 modules have been assembled with these features:

- **Pizza Box # 1:** TDC-standard (fibers Bicron - 1.0 mm, SiPM 1.2× 3.2 mm^2 - 4020);
- **Pizza Box # 2:** TDC-standard;
- **Pizza Box # 3:** TDC-standard;
- **Pizza Box # 4:** TDC-standard;
- **Pizza Box # 5:** TDC-special (fibers Bicron - 1.2 mm);
- **Pizza Box # 6:** TDC-special (round SiPM - 5550);

[1] Just to remember, while the scintillator bar thickness for time readout is 2 cm, for the binary read our there are two orthogonal scintillator layer 1cm thick, one measuring the x and the other one the y coordinate.

Figure 6.2: *Pizza boxes features.*

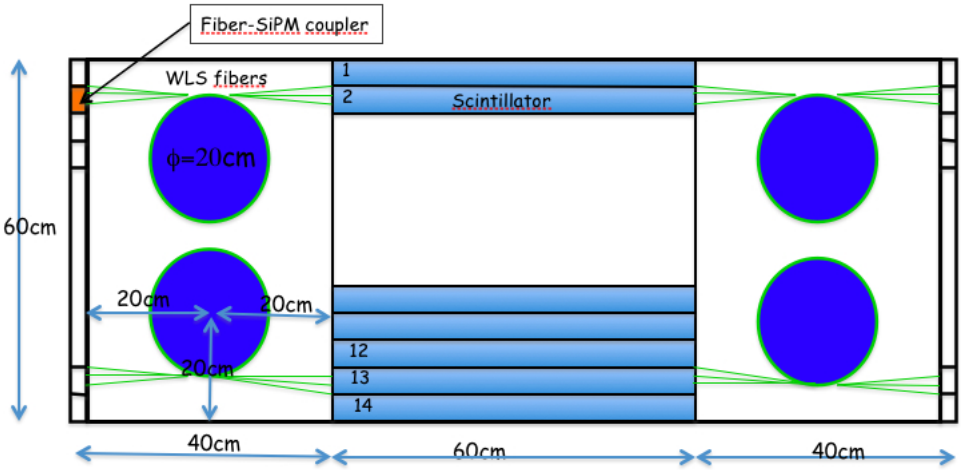

(a) Dimensions of the pizza boxes

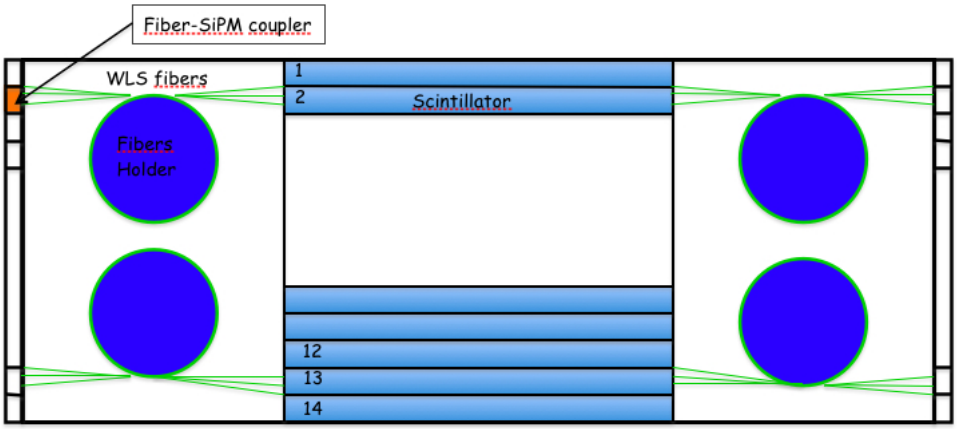

(b) TDC layout

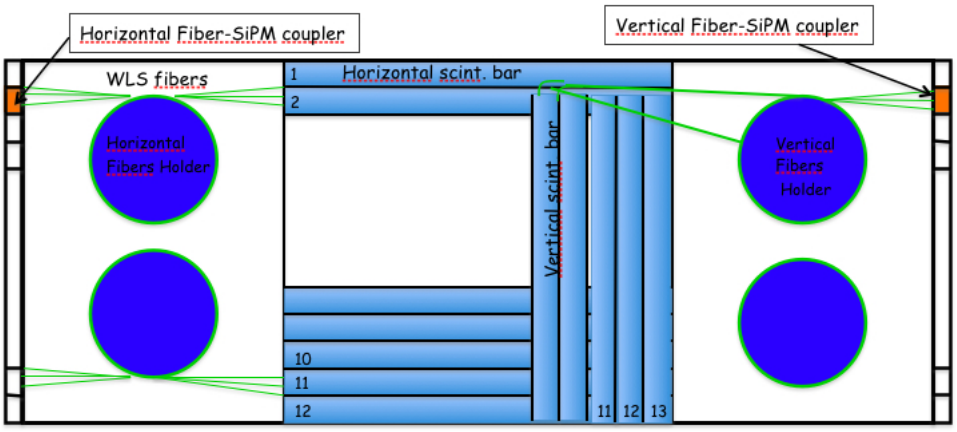

(c) BiRo layout

- **Pizza Box # 7:** TDC-special (MPPC);
- **Pizza Box # 9:** BiRo-standard (fiber Kuraray - 1.2 mm, SiPM 1.4× 3.8 mm^2 - 4380);
- **Pizza Box # 10:** BiRo-standard;
- **Pizza Box # 11:** BiRo-standard;
- **Pizza Box # 12:** BiRo-special (round SiPM - 5550).

Tab. 6.1 shows all details of the pizza boxes assembled; in particular during the test beam a maximum number of detectors[2] with the baseline geometry configuration has been tested. The different fibre features are useful to test the detector resolution in order to find the configuration which gives us the best resolution. It is important to note that the final detector will have ≈4 m long fibres, so different lengths and diameters are helpful to understand the fibres behaviour.

Table 6.1: *Pizza Boxes details.*

Layer	Pizza Box #	Type	Fibres length L (left) cm	Fibres length R (right) cm
0	11	BIRO	210	240
1	2	TDC	310	90
1'	5	TDC	230	170
2	9	BIRO	370	320
3	4	TDC	230	170
4	12	BIRO	210	240
5	3	TDC	260	140
6	10	BIRO	190	280
7	1	TDC	355	45
7'	6	TDC	230	170
8	8	BIRO	110	260

All these modules have been tested with cosmic rays before the shipment to Fermilab giving good results and showing a nice behaviour. In the prototype of the IFR the BiRo modules are layers 0,2,4,6,8 and the other ones are TDC.

[2]In the last days of the test beam we changed the first and seventh layer (1' and 7') as shown in the Tab. 6.1.

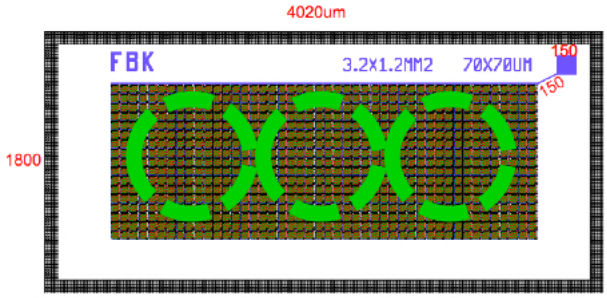

(d) 1.2×3.2 mm^2 - 4380

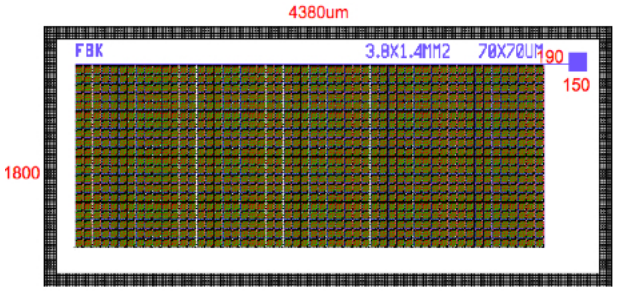

(e) 1.4×3.8 mm^2 - 4020

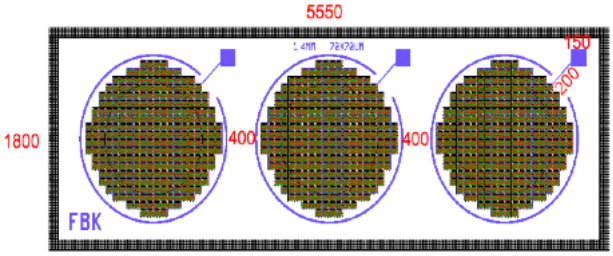

(f) 3 round sensors ϕ =1.4mm - 5550

Figure 6.3: *Three different SiPM geometry tested during the first beam test.*

Figure 6.4: *Internal view of an active layer.*

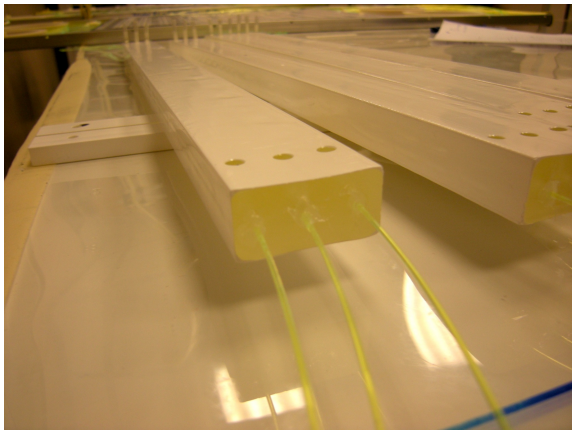

Figure 6.5: *The three fibers carry out signals to the SiPM.*

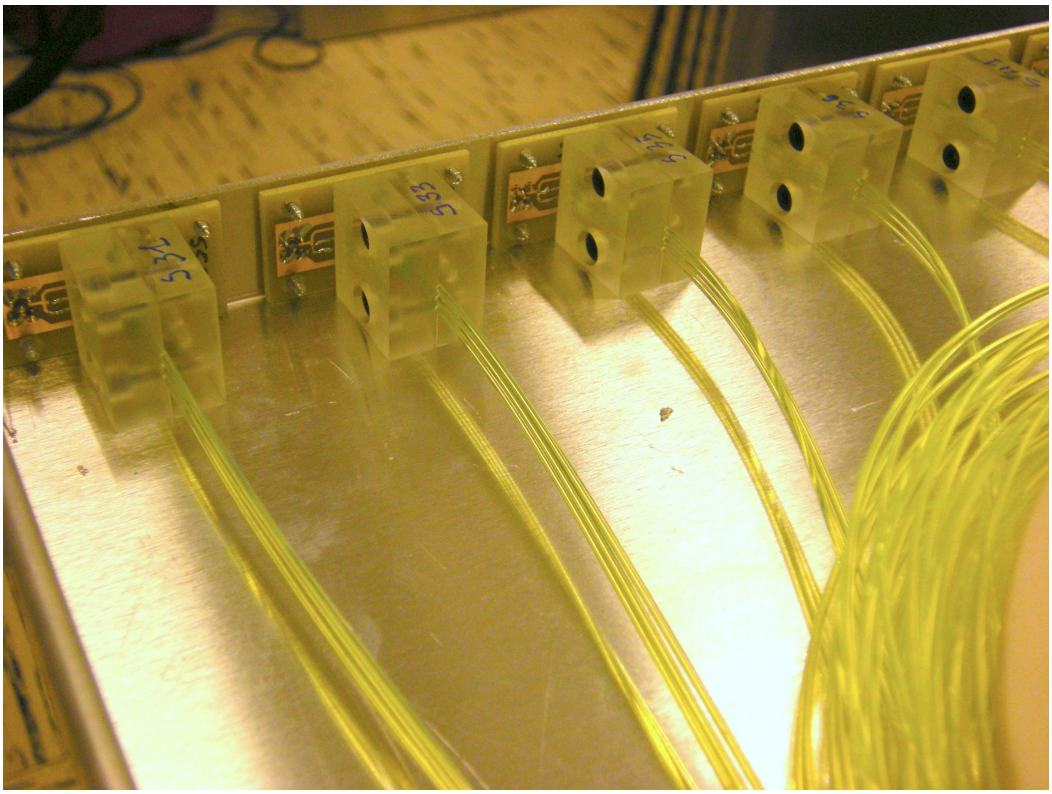

Figure 6.6: *Detail of WLS fibers coupling with SiPM.*

6.2 Fermilab Beam test

The prototype has been tested at the Fermilab Meson Beam Test Facility during November/December 2010. In Fig. 6.7 the location of beam test is shown and in particular it is possible to note the experimental setup for testing our detector: the IFR prototype was between 4 scintillator layers, functioning as trigger, with a Cerenkov detector before and a MWPC (Multi Wire Plate Chamber), useful for particle identification.

During the beam test the opportunity to test the prototype with different particle energies and particle types was allowed, so four different triggers have been made using the two PMTs before the prototype (the s_1 and s_2), behind and beyond the prototype, and two signals from Cerenkov (c_1 and c_2[3]):

- not electron trigger (default) (this is the AND function between s_1, s_2 and $\overline{c_2}$);
- muon trigger (this is the AND function between s_1, s_2, c_1 and $\overline{c_2}$);
- pion trigger (this is the AND function between s_1, s_2, $\overline{c_1}$ and $\overline{c_2}$);
- electron trigger (this is the AND function between s_1, s_2, c_2).

[3] c_1 is the signal that indicate the passage of muon and c_2 indicates an electron.

Fig. 6.8 and 6.9 shows the assembled prototype ready to be tested.

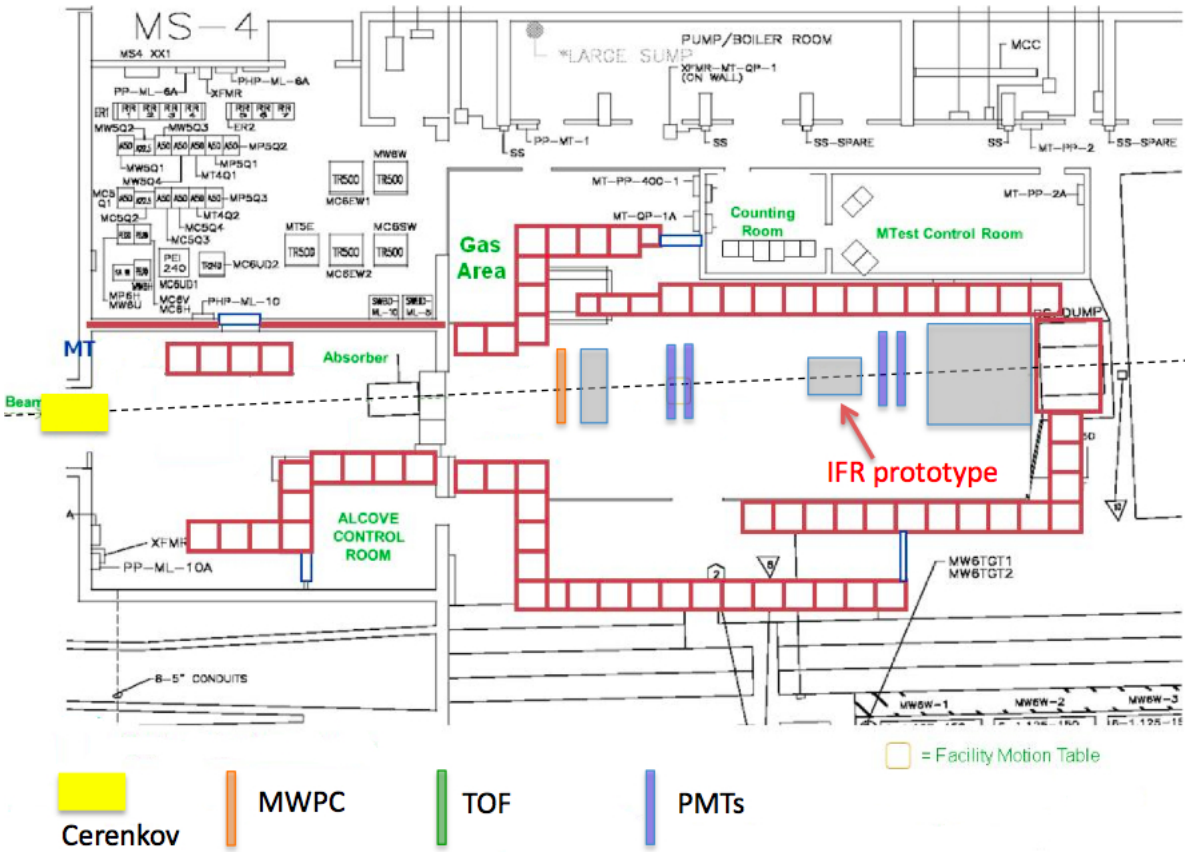

Figure 6.7: *View of experimental setup for Fermilab Beam Test.*

Initially the prototype has been tested using beam, whose particle composition is shown in Fig. 6.10, at an energy of 8 GeV and the main aim of this beam test was to check the prototype at lowest momenta (this has not been possible because some problems with a Cerenkov gas occur, so the lower energy tested was been 4 GeV[4]).

6.2.1 Hit maps

To monitor the detector during the test an online monitor has been developed: this interface consists principally in a plot series of channel counts, to see if there were dead channels. In Fig. 6.11, showing a hit map of a layer with Binary Readout the top of figure represents the y position, while the bottom one the x position[5] of the hit.

In this plot the y axis represents the electronic channel, while the x axis indicates the sample number when the layer is read: the layer is read every 12.5 ns, so 1 is the sample at 12.5 ns, 2 at 25 ns and so on. In this plot concerning a run at 8 GeV, where there were

[4]Beyond this energy the particle identification worked well.

[5]The Z axis is coincident with the beam line.

Figure 6.8: *View of a geometry configuration studied during the beam test.*

Figure 6.9: *View of cabled layers.*

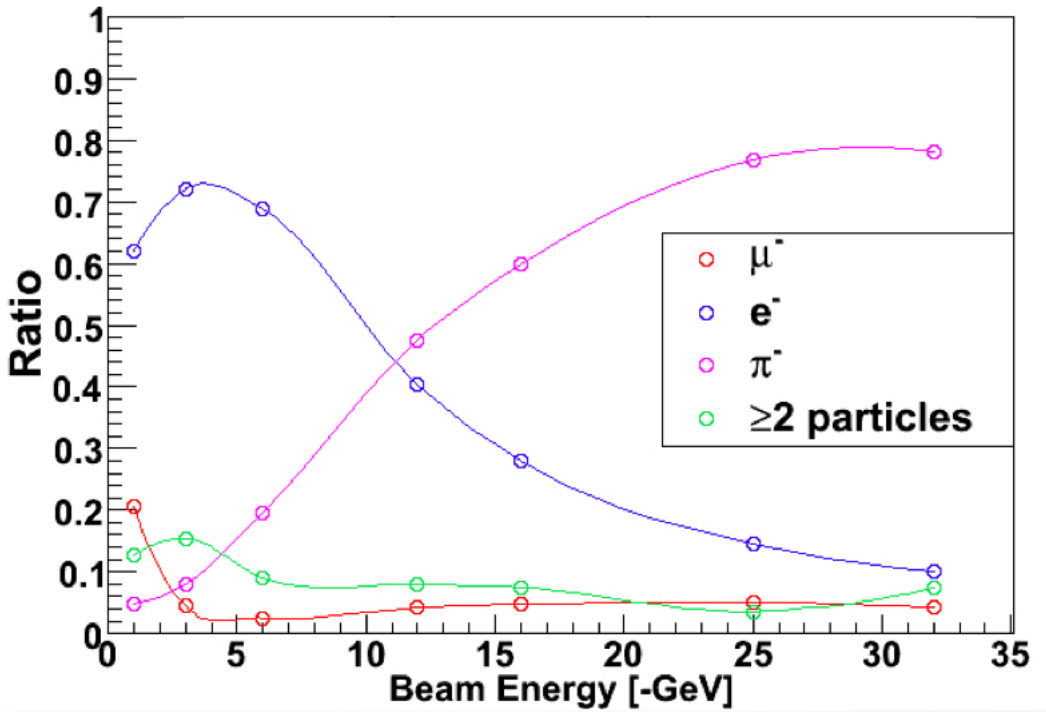

Figure 6.10: *Beam composition from CALICE.*

mostly pions, it is possible to verify the presence of pions. Looking for example at Fig. 6.11, 6.12, 6.13 the propagation of hadronic shower is evident: starting from first figure, where the distribution of hit map is narrower and there are a large amount of counts in central channels, shifting to second one and so on, it is possible to note the widening of the distribution.

One of the advantages of the online monitor was the possibility to control the presence of dead channels at every run, so to test the SiPM quality (see the hole for example at top of Fig. 6.12); while in the bottom of Fig. 6.13 one layer channel has been changed to another electronics channel (channel 24 shifted to channel 29).

The propagation of the hadronic shower is clearly visible in the TDC hit map too (Figures 6.14, 6.15).

6.2.2 Efficiencies

To test the IFR prototype means to calculate the efficiencies of the scintillator layers in order to verify if the detector works properly and can satisfy the physics requirements. The preliminary efficiency of a layer has been calculated using muons, pions and mixed events in this first sample manner: the particle must hit both scintillators behind the prototype and it is a check if hit is visible in a defined layer.

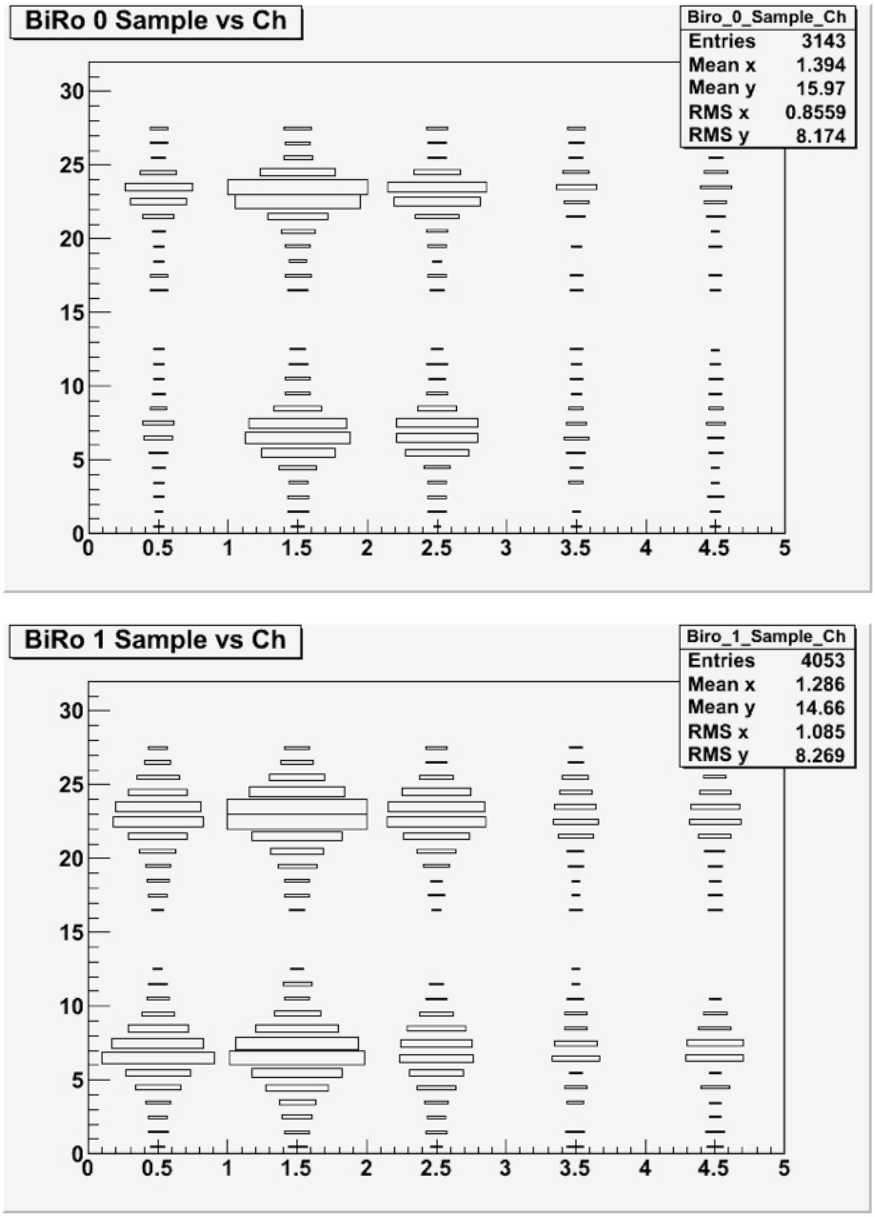

Figure 6.11: *Example of BiRo hit map from Monitoring Online: Layer 0 (top) and Layer 2 (bottom).*

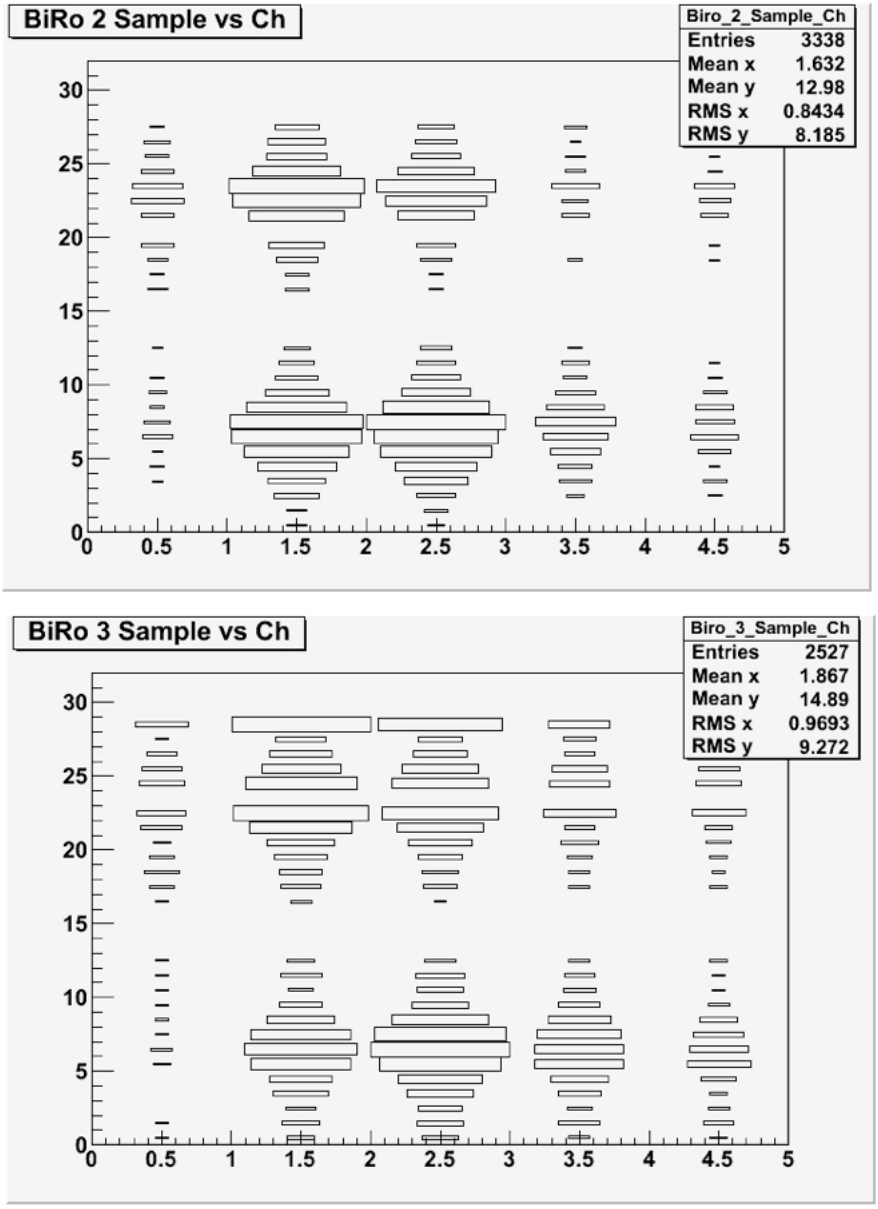

Figure 6.12: *Example of BiRo hit map from Monitoring Online: Layer 4 (top) and Layer 6 (bottom).*

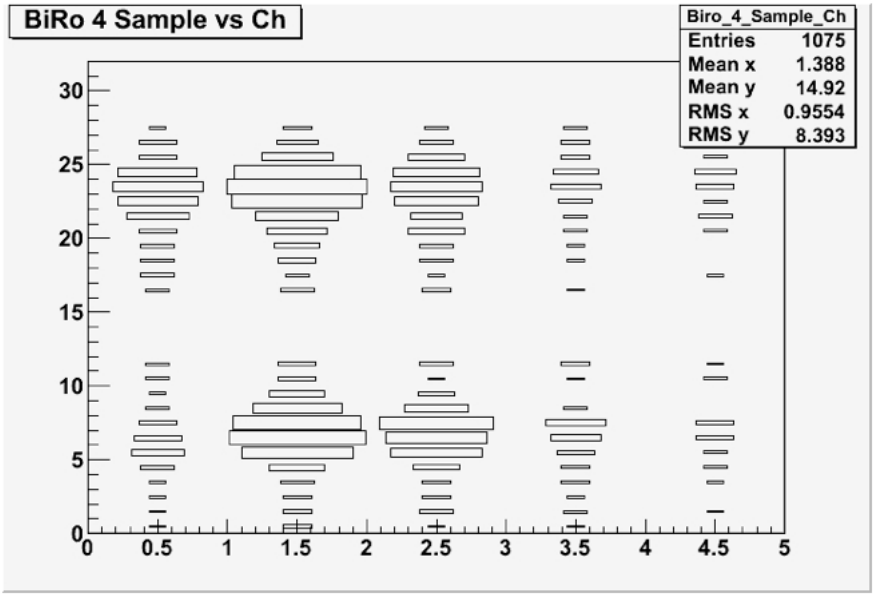

Figure 6.13: *Example of BiRo hit map from Monitoring Online: Layer 8.*

From first data, the detector seems to work properly. In fact in Fig. 6.16 all layers (layer 7 is missed because it was not put inside the detector) have an efficiency more than 90%. These preliminary results are very encouraging and it is interesting to study the efficiencies of a layer, for example, as function of SiPM threshold of photoelectrons. Naturally the detection efficiency decreases increasing the SiPM threshold, as shown in Fig. 6.17, 6.18.

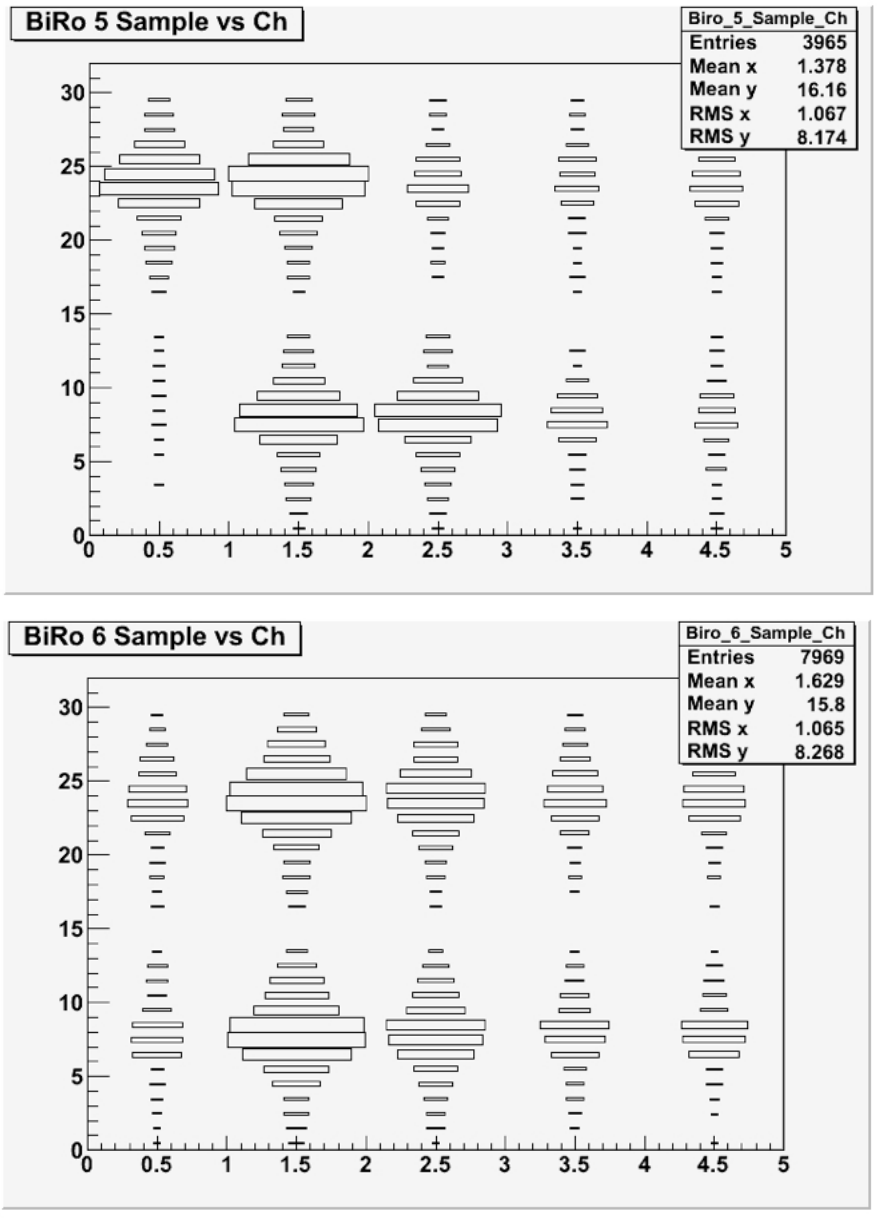

Figure 6.14: *Example of TDC hit map from Monitoring Online: Layer 1 (top) and Layer 3 (bottom).*

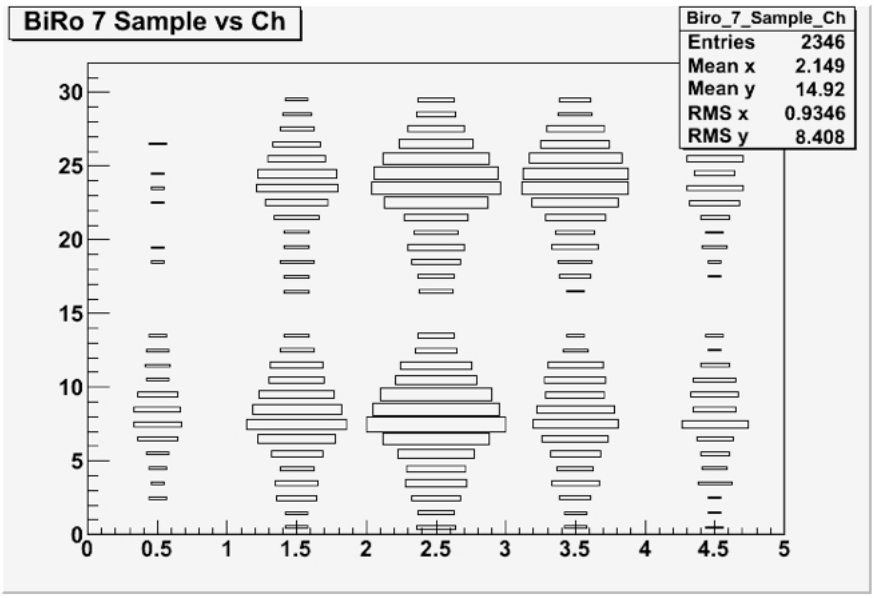

Figure 6.15: *Example of TDC hit map from Monitoring Online: Layer 5.*

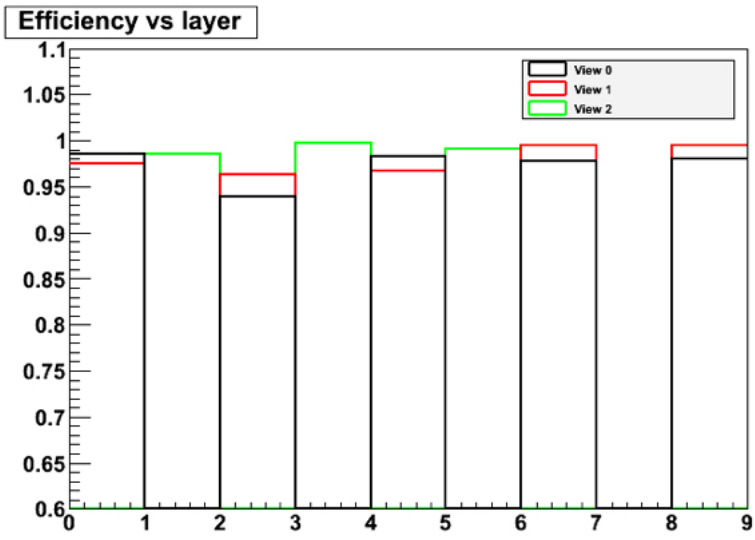

Figure 6.16: *Efficiency versus layer. Black and red line concern to, respectively, X and Y view of BiRo modules, while the green one TDC modules.*

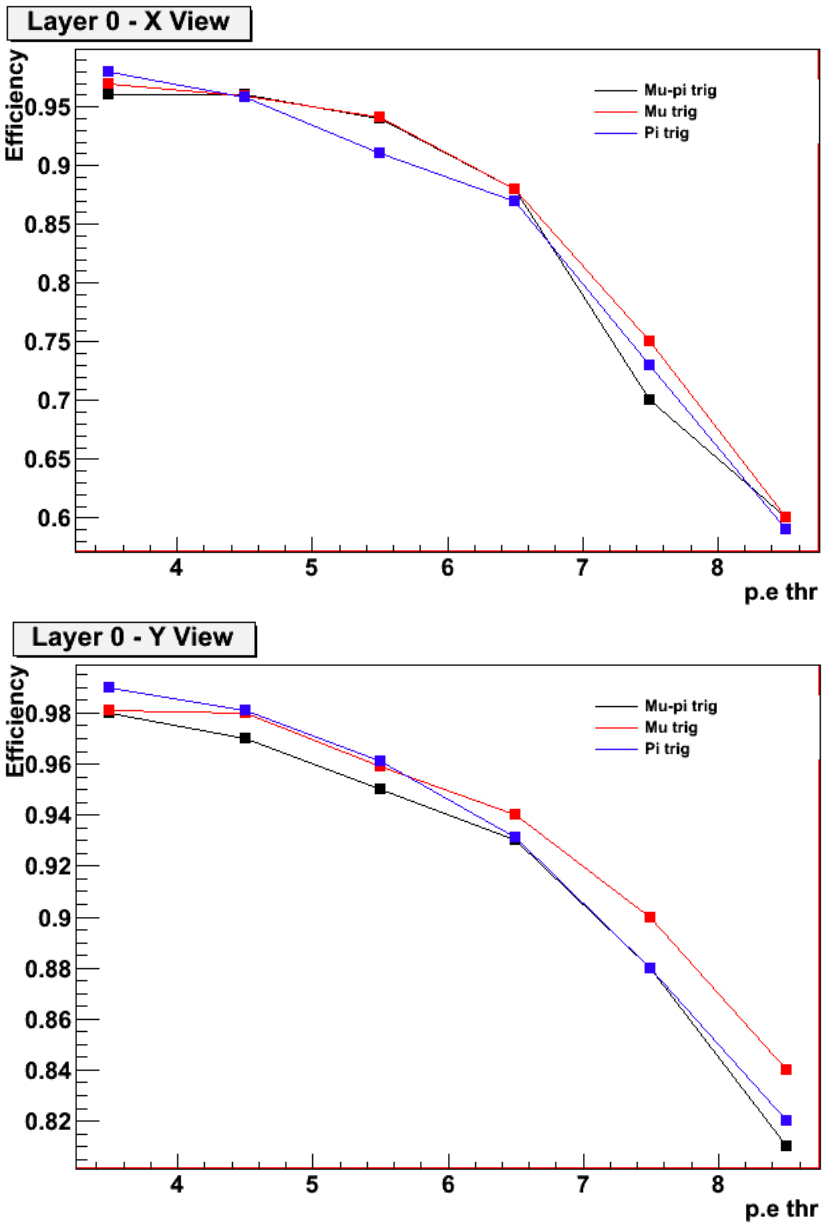

Figure 6.17: *Layer 0 efficiency, at 8 GeV beam energy, X view(top) andY view(bottom), versus SiPM photoelectrons threshold: black line is $\mu - \pi$ trigger, red is μ and blu is π trigger.*

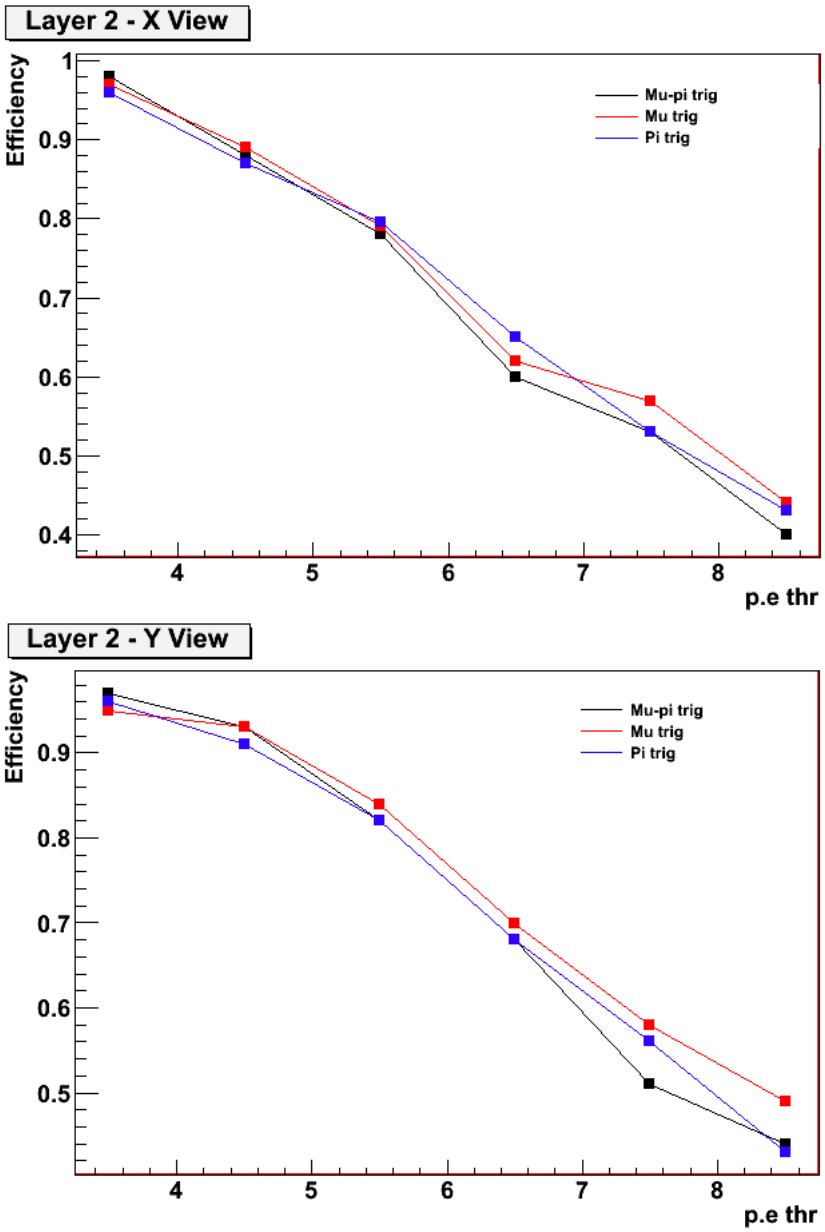

Figure 6.18: *Layer 2 efficiency, at 8 GeV beam energy, X view(top) and Y view(bottom), versus SiPM photoelectrons threshold: black line is $\mu - \pi$ trigger, red is μ and blu is π trigger.*

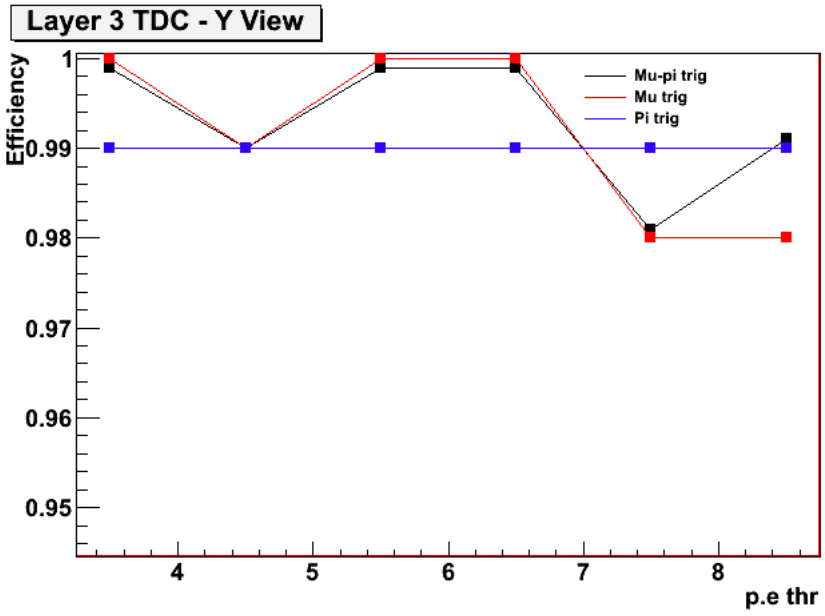

Figure 6.19: *Layer 3 efficiency, at 8 GeV beam energy, versus SiPM photoelectrons threshold: black line is $\mu - \pi$ trigger, red is μ and blu is π trigger.*

6.2.3 Time resolutions

One of the aims of the beam test was to study the time resolution of the layers. In particular to do this the following technique has been adopted: for each detector layer only one scintillator has been studied, in particular the central one, in order to select the scintillator knocked only by the beam that should have the right resolution, avoiding to study the other one that can be hit by the hadronic showers produced by pions.

It is important to note that this is a preliminary study of the beam test data and this evaluations has been conducted analyzing a total data sample of 143.000 events.

To calculate the time resolution we consider the time distribution given by the first scintillator before the prototype(S1), that starts the trigger, and we evaluated his resolution time σ_{S1} fitting this distribution with a gaussian function. In Fig. 6.20 it is possible to see that $\sigma_{S1} = 0.85$ ns and this one is important to calculate the time resolutions for each TDC layer of detector, in fact we will use this equation:

$$\sigma_{\mathrm{Lx}} = \sqrt{\sigma^2_{\text{gauss fit}} - \sigma^2_{S1}} \tag{6.1}$$

where σ_{Lx} indicates the resolution time of the layer x and the $\sigma_{\text{gauss fit}}$ means the σ of the distribution time gaussian fit related to the layer considered. The time resolutions will be evaluated, obviously, at left and right of the scintillator layer in order to verify the dependance of the time resolution from the fibre length.

Looking at Tab. 6.2 it is important to note that the scintillator and the fibres used

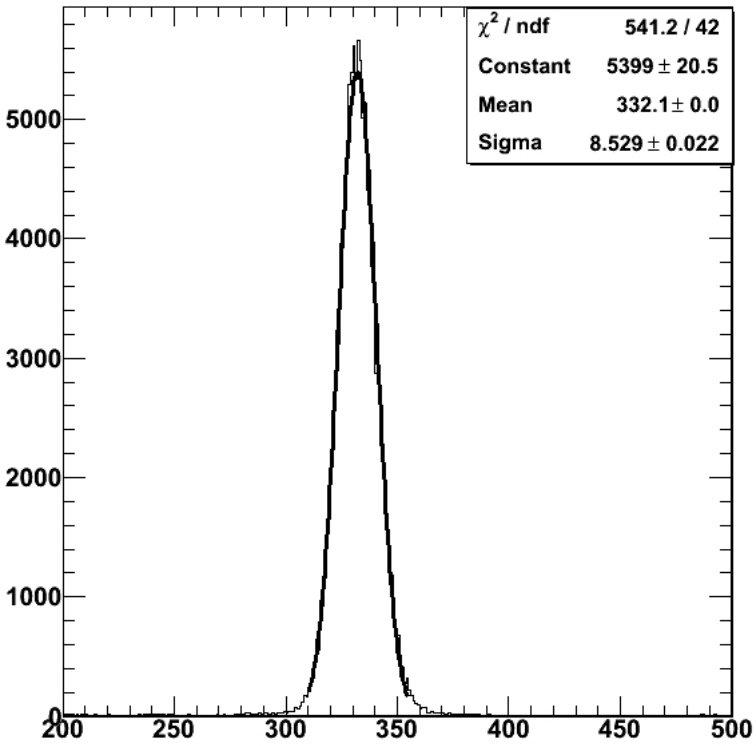

Figure 6.20: *Gaussian fit of the S1 time distribution.*

Table 6.2: *Time resolutions of the TDC layers.*

Layer	$\sigma_{\text{gauss fit}}$(ns)	σ_{Lx}(ns)
1L	1.396 ± 0.008	1.046 ± 0.011
1R	1.195 ± 0.006	0.758 ± 0.010
1L'	1.154 ± 0.013	0.692 ± 0.022
1R'	1.154 ± 0.013	0.692 ± 0.022
3L	1.184 ± 0.005	0.741 ± 0.008
3R	1.181 ± 0.005	0.736 ± 0.008
5L	1.133 ± 0.018	0.656 ± 0.031
5R	1.232 ± 0.019	0.815 ± 0.029
7L	1.500 ± 0.020	1.182 ± 0.025
7R	1.073 ± 0.009	0.546 ± 0.018
7L'	1.049 ± 0.017	0.497 ± 0.036
7R'	0.975 ± 0.015	0.312 ± 0.047

Figure 6.21: *Layer 1 Time resolution.*

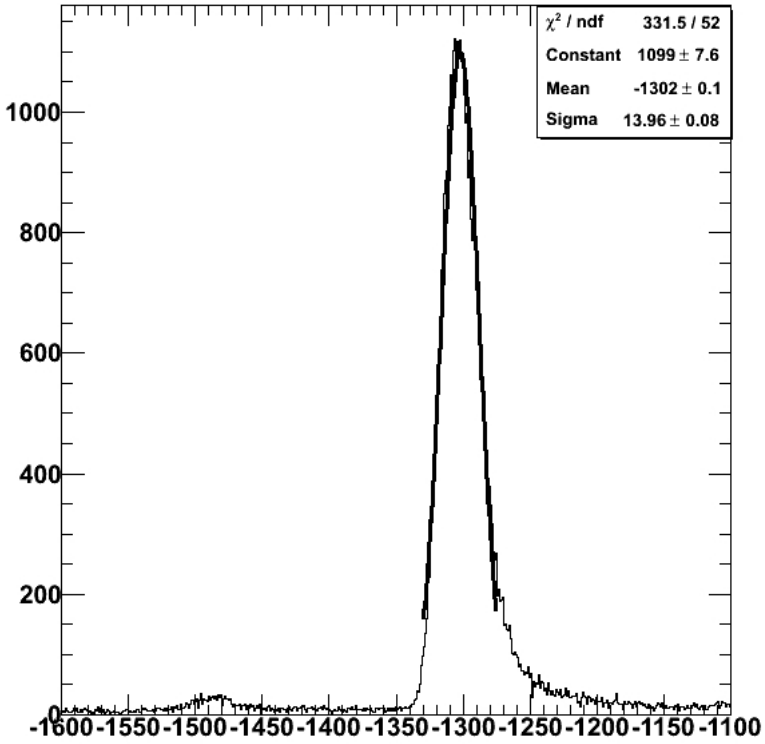

(a) Left side

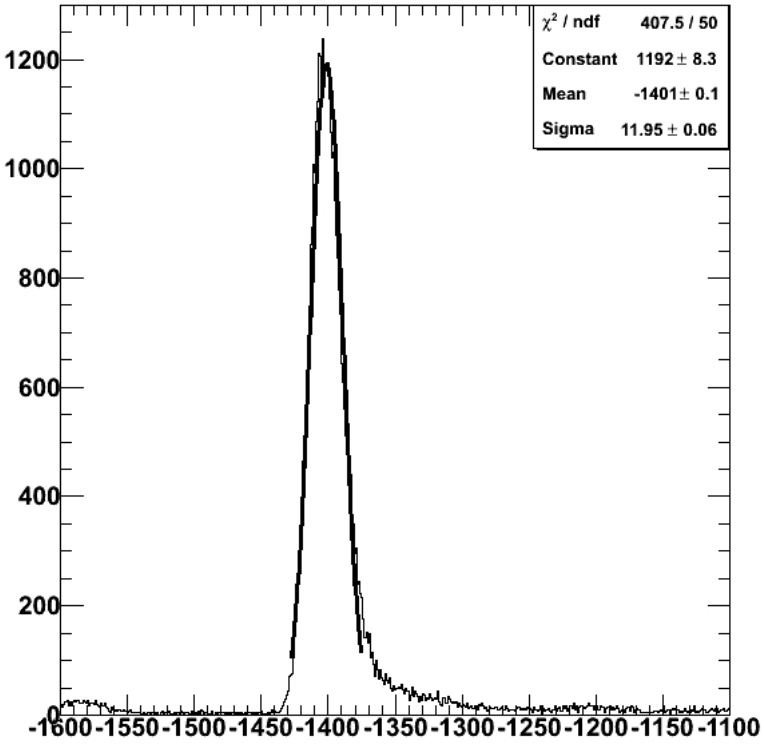

(b) Right side

Figure 6.22: *Layer 1' Time resolution.*

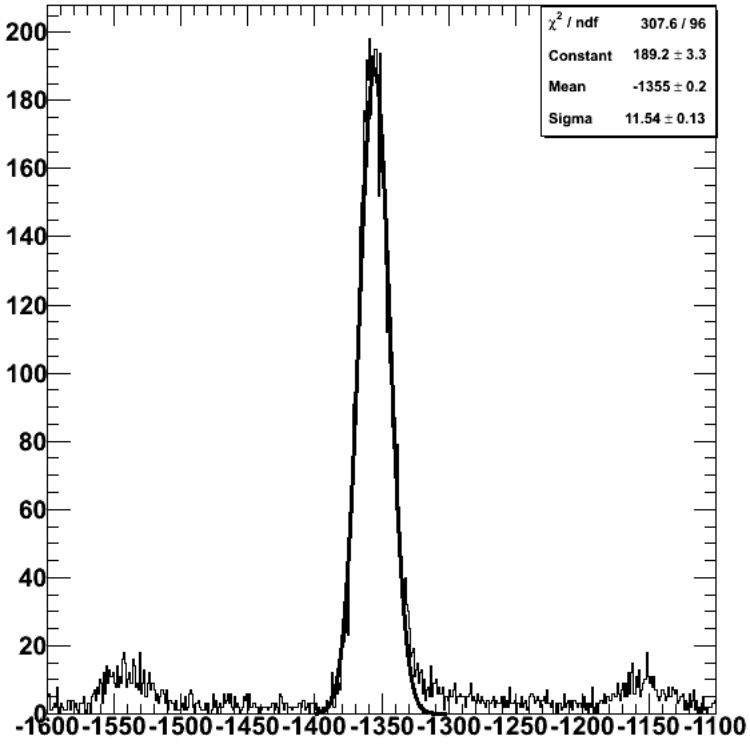

(a) Left side

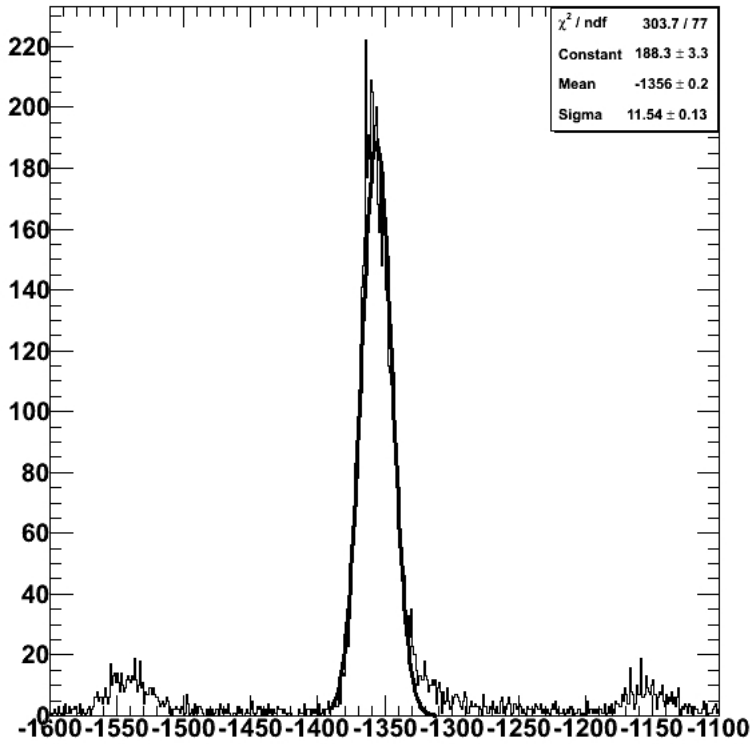

(b) Right side

Figure 6.23: *Layer 3 Time resolution.*

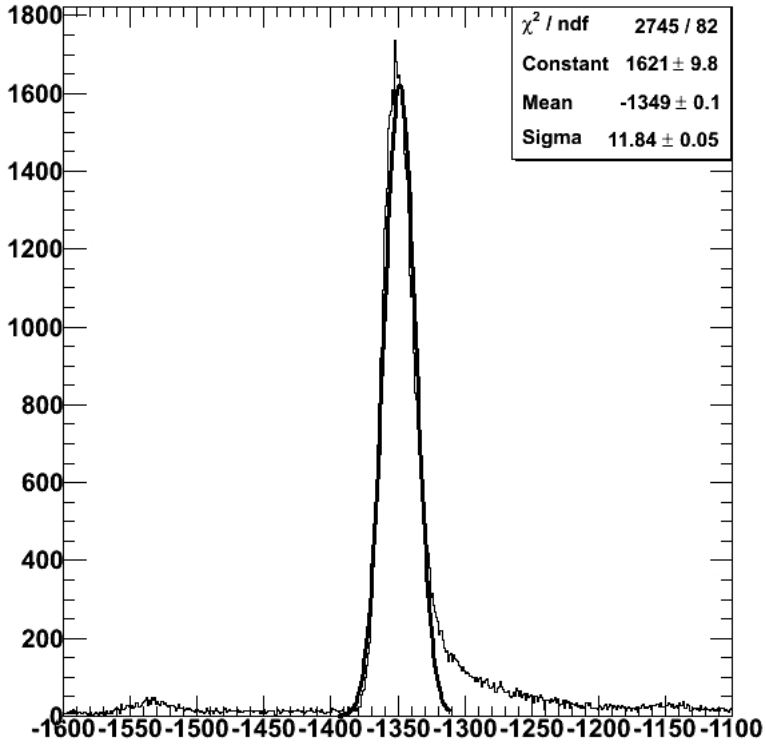

(a) Left side

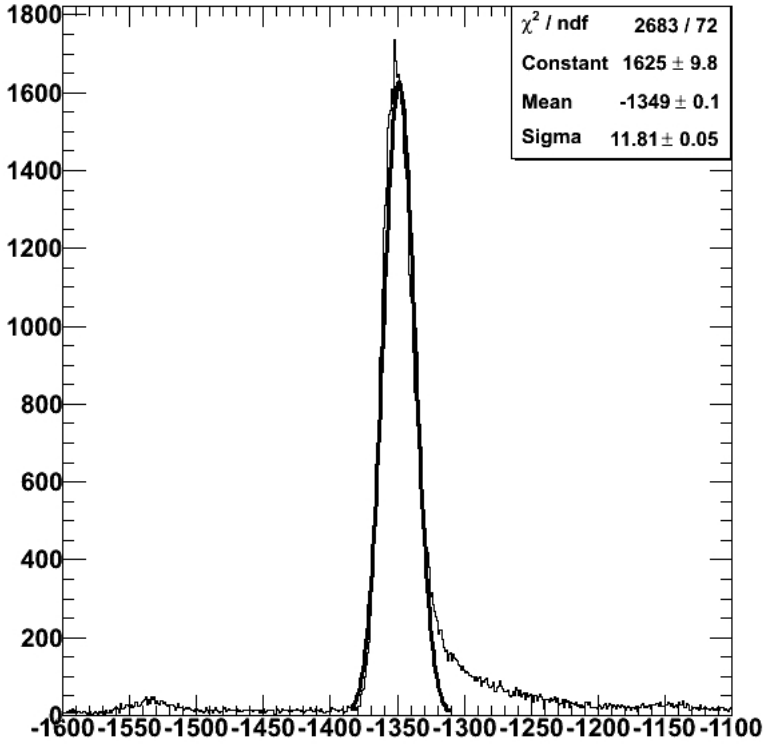

(b) Right side

Figure 6.24: *Layer 5 Time resolution.*

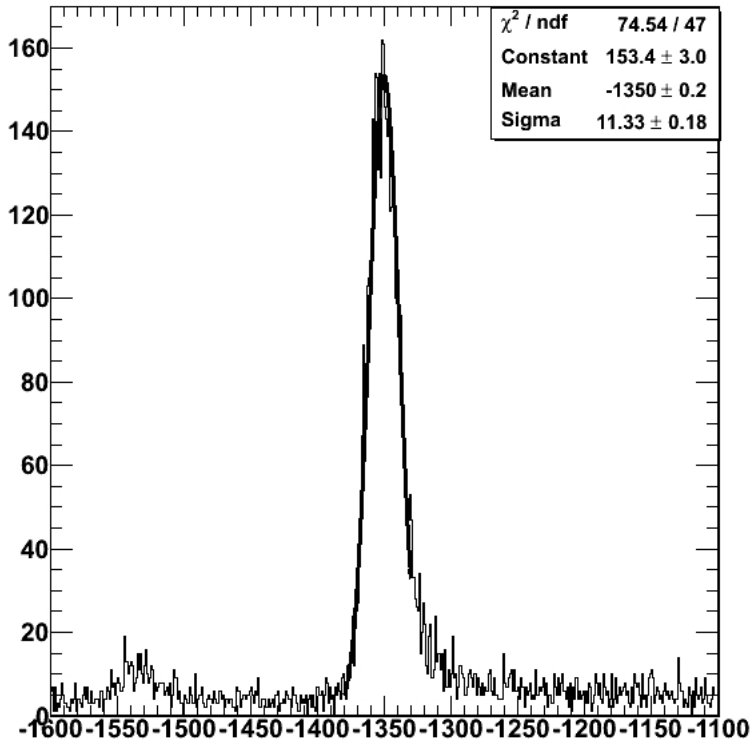

(a) Left side

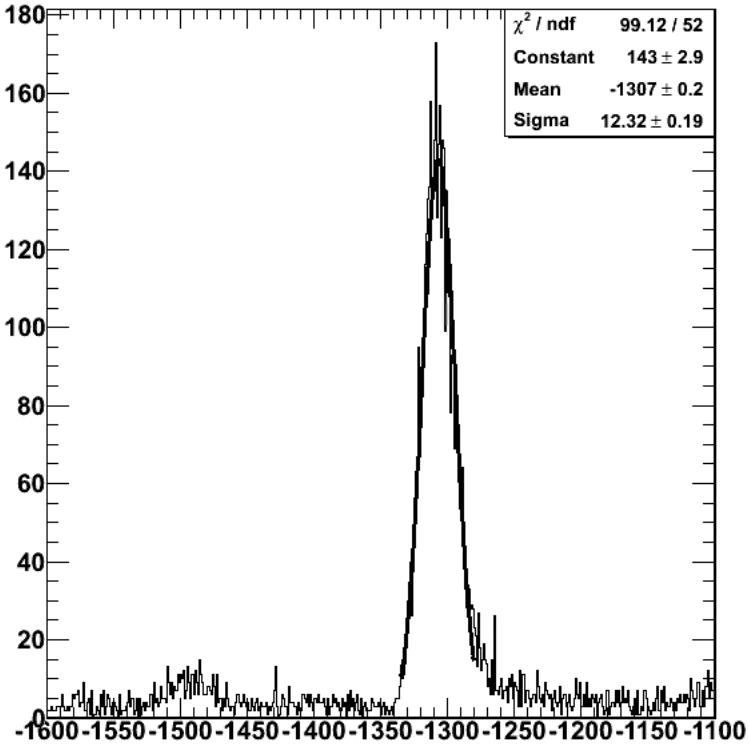

(b) Right side

Figure 6.25: *Layer 7 Time resolution.*

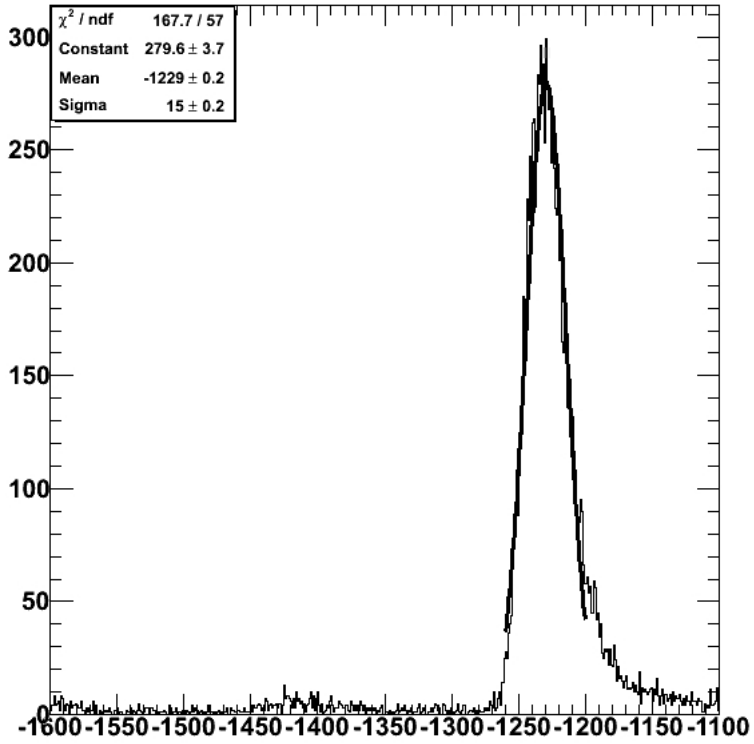

(a) Left side

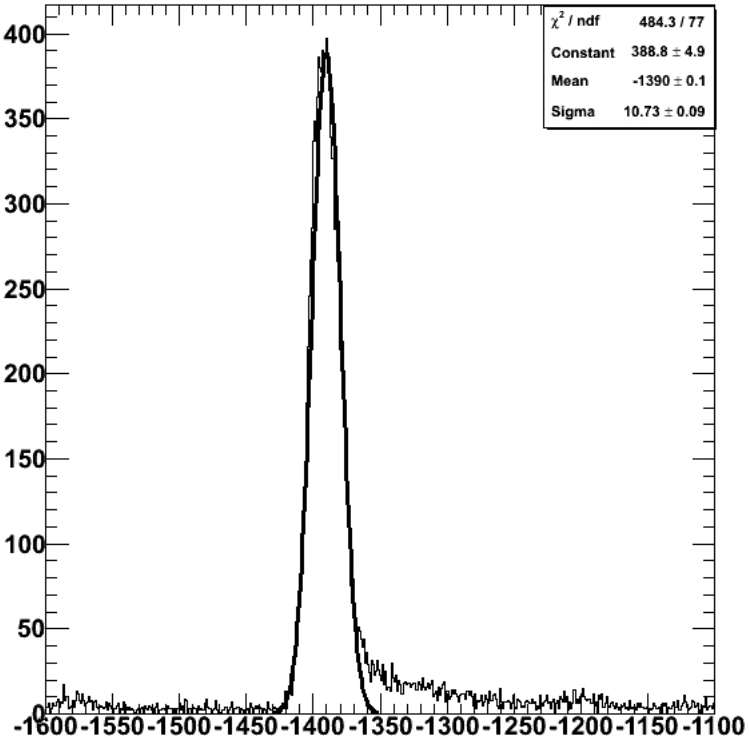

(b) Right side

Figure 6.26: *Layer 7' Time resolution.*

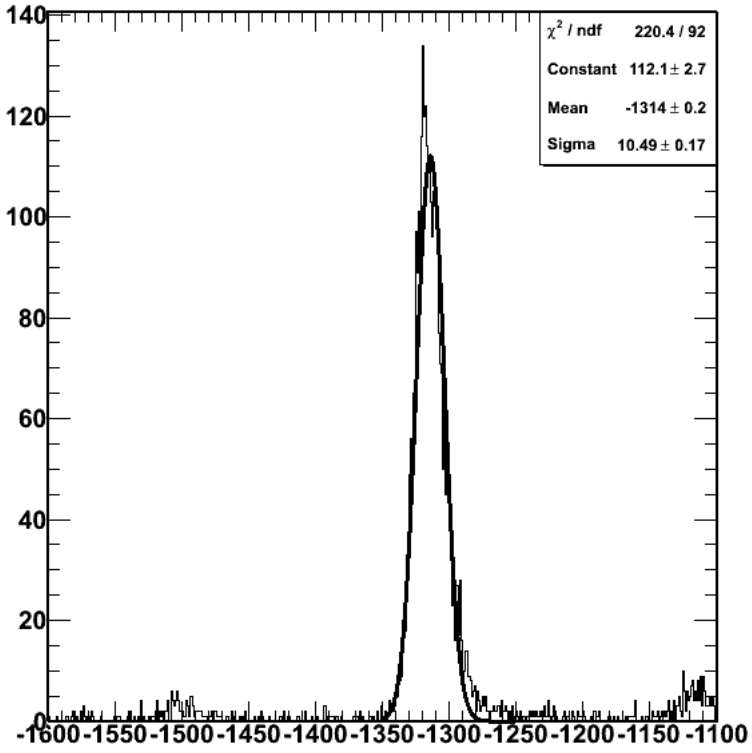

(a) Left side

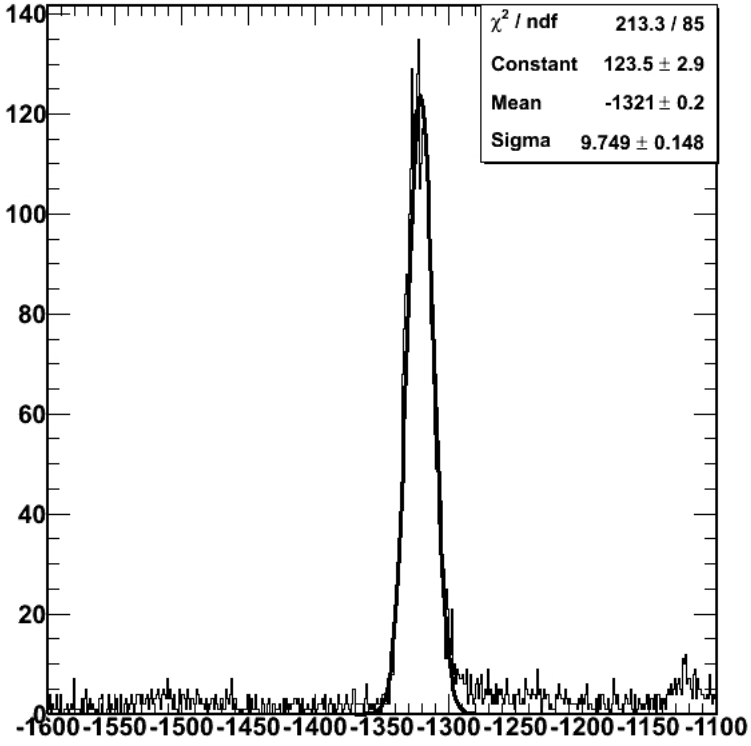

(b) Right side

give very good results. The IFR team aimed at a resolution $\approx$ 1 ns, corresponding to $\approx$ 20 cm, and the first results of the beam test satisfy this condition and it is possible to note that we obtained also better resolution than 1 ns. Naturally the time resolution depends on the fibre length and in fact the best resolution is in layer 7 right side, where the fibre length of the right side was 45 cm. On the other hand the worst resolution found is on the right side of the layer 7', in fact here the fibre was 355 cm long.

Observing the time resolution of the layer 7' , it is possible to remark that this resolution is very low with respect to the other ones: this fact is understandable if we consider that at this point of prototype most probably will arrive either pions that did not interact with iron or muons; so with these very clean events the time resolution is better.

Since 1 ns of time resolution corresponds to 20 cm, it is possible to quantify the length difference between the fibres of a scintillator bar taking those scintillator where there is an appreciable length variation. In fact, for example, layer 3 where the difference between the fibres length is 60 cm, this corresponds to time resolution variation of 3 ns and with this low statistics. In any case we can test if our results are consistent taking for example layer 1 and layer 7, respectively with a 220 cm and 310 cm length difference.

Taking the gaussian peaks of each side it is possible to calculate the dissimilarity, for example for layer 1 the difference is 99 that corresponds to $\approx$ 200 cm and this is not so divergent from the right value of 220 cm; on the other hand for the layer 7 the difference between the two gaussian peaks is 161, that is equal to $\approx$ 322 cm with respect to a correct value of 310 cm. For the other layers the difference is not so precise, principally due to not so high statistics, but it is important to note that in the layer 5 the two peaks are separated too.

The important note to remark, in order to conclude, is that the detector, looking at Tab. 6.2, has a very good time resolutions around 1 ns, that the IFR collaboration are looking for.

Conclusions

The SuperB project is the flagship project of the Istituto Nazionale di Fisica Nucleare (INFN) and 2011 will be the year focused on the drafting of the Technical Design Report. In this year the construction of the infrastructures related to the accelerator machine will probably begin and first data are expected approximately in 2020.

These three years have been dedicated principally to propose at SuperB collaboration a layout of muon detector that can satisfy physics requirements and can warrant a long time of data taking. In this thesis there is a detailed description of the muon detector with all studies considered crucial for the detector optimization: in particular the muon identification and the neutron silicon damage.

From the first simulations we have seen that the IFR detector proposed seems to work very well, with a good muon identification, approximately around at 90% for momentum greater than 1.5 GeV/c, with a pion contamination fixed at 2%. On the other hand, from the point of view of the neutron rate study, it has been shown that with this layout of the detector the rate is higher and we have found a possible solution to avoid the damage of the silicon photo multiplier, decreasing with a 10 cm of polyethylene the rate by an order of magnitude.

Further improvements on these studies are needed, in particular increasing the statistics of data samples and describing in more details the machines, because the more detailed will be the description of the whole detector, the more precise will be the simulations results. Concerning the muon identification, we should study a possible configuration that permits to improve the muon identification at low momenta or to study the muon identification utilizing the inner detectors. Some studies are needed about the identification of the K_L particles with the IFR, in particular to determine if there will be improvements with the 9 scintillators layers configuration.

From the point of view of neutron rate study, a definitive description of the accelerator machine, beam pipe and of the inner detectors is required because, as seen in Chapter 4,

a good photons and electrons/positrons shield can be a neutron generator.

A milestone of the detector design is the comparison between simulations and the beam test data, in order to verify if simulations are reliable: for this reason, concerning to IFR detector, another beam test is planned in July 2011.

From the first look at the beam test data we note that the prototype seems to work properly, giving good time resolutions and efficiencies. The IFR team searches for an efficient and 1 ns time resolution detector and with this layout, this requirement can be satisfied.

Bibliography

[1] http://gdml.web.cern.ch/GDML/.

[2] http://geant4.cern.ch/.

[3] http://root.cern.ch/drupal/.

[4] The BABAR Physics Book. http://www.slac.stanford.edu/pubs/slacreports/slac-r-504.html.

[5] Evtgen, A Monte Carlo Generator for B-Physics. http://robbep.home.cern.ch/robbep/EvtGen/GuideEvtGen.pdf.

[6] TMVA: Toolkit for Multivariate Data Analysis with ROOT. http://tmva.sourceforge.net.

[7] PEP-II: An Asymmetric B Factory. *Conceptual Design Report, CALT-68-1869, LBL-PUB-5379, SLAC-418, UCRL-ID-114055, UC-IIRPA-93-01*, 1993.

[8] http://www.slac.stanford.edu/BFROOT/www/Organization/Spokesperson/P5/, 2005.

[9] K. Abe and al. *Phys. Rev. Lett. 96, 221601*, 2006.

[10] K. Abe and al. [Belle Collaboration]. *arXiv:hep-ex/0408132*.

[11] K. Abe and al. [Belle Collaboration]. *arXiv:hep-ex/0507034*.

[12] A. Akeroyd and al. *SuperKEKB Physics Working Group, arXiv:hep-ex/0406071*, 2004.

[13] M. Angelone and al. *http://arxiv.org/pdf/1002.3480v1*, 2010.

[14] B. Aubert and al. [BABAR Collaboration]. *arXiv:hep-ex/0607107*.

[15] B. Aubert and al. [BABAR Collaboration]. *arXiv:hep-ex/0607104*.

[16] B. Aubert and al. [BABAR Collaboration]. *arXiv:hep-ex/0408086*.

[17] B. Aubert and al. [BABAR Collaboration]. *Phys. Rev. D 66, 010001*, 2002.

[18] B. Aubert and al. [BABAR Collaboration]. *Phys. Rev. Lett. 93, 021804*, 2004.

[19] B. Aubert and al. [BABAR Collaboration]. *Phys. Rev. Lett. 93, 081802*, 2004.

[20] B. Aubert and al. [BABAR Collaboration]. *Phys. Rev. Lett. 94, 221803*, 2005.

[21] B. Aubert and al. [BABAR Collaboration]. *Phys. Rev. D 72, 052004*, 2005.

[22] B. Aubert and al. [BABAR Collaboration]. *Phys. Rev. D 72, 051103*, 2005.

[23] B. Aubert and al. [BABAR Collaboration]. *Phys. Rev. Lett. 96, 241802*, 2006.

[24] B. Aubert and al. [BABAR Collaboration]. *Phys. Rev. Lett. 96, 241802*, 2006.

[25] B. Aubert and al. [BABAR Collaboration]. *Phys. Rev. Lett. 97, 171803*, 2006.

[26] B. Aubert and al. [BABAR Collaboration]. *Phys. Rev. D 73, 092001*, 2006.

[27] Heavy Flavour Averaging Group (E. Barberio and al. *arXiv:hep-ex/0603003*.

[28] J. Benitez and al. *SLAC-PUB-12236*, 2006.

[29] J. Benitez and al. *Nucl. Instrum. Methods Phys. Res., Sect. A 595*, 2008.

[30] Hugo W. Bertini. *Physical Review, 188 4*, 1969.

[31] S. Bettarini and al. Measurement of the Charge Collection Efficiency After Heavy Non-Uniform Irradiation in BABAR Silicon Detectors. *IEEE Trans. Nucl. Sci. 52, 1054*, 2005.

[32] S. Bettarini and al. Development of Deep N-well Monolithic Active Pixels Sensors in a 0.13 μm CMOS Technology. *Nucl. Instr. Methods Phys. Res., Sect. A 572*, 2007.

[33] M. Bona and al. [UTFit Collaboration]. *JHEP 0507, 028*, 2005.

[34] M. Bona and al. [UTFit Collaboration]. *JHEP 0610, 081*, 2006.

[35] A. Bondar, T. Gershon, and P. Krokovny. *Phys. Rev. B* **624**, *1*, 2005.

[36] G. Calderini and al. Report of the Physics Impact of Beam Background Task Force. *BaBar Analysis Document BABAR-BAD-707*, 2001.

[37] K. F. Chen and al. [Belle Collaboration]. *Phys. Rev. Lett. 98, 031802*, 2007.

[38] S. Chen and al. [CLEO Collaboration]. *Phys. Rev. Lett. 87, 251807*, 2001.

[39] BABAR Collaboration. *BABAR-CONF-06/040, SLAC-PUB-12015*, 2006.

[40] BABAR Collaboration. *BABAR-CONF-06/18, SLAC-PUB-11987*, 2006.

[41] BABAR Collaboration. *BABAR-CONF-06/038, SLAC-PUB-12028*, 2006.

[42] Belle Collaboration. *Phys. Rev. D* **73**, *112009*, 2006.

[43] Belle Collaboration. *Phys. Rev. Lett.* **98**, *031802*, 2007.

[44] MINOS collaboration. *"The MINOS Technical Design Report" NuMI Note, NuMIL-337.*

[45] N. Satoyama[Belle Collaboration]. *arXiv:hep-ex/0611045*, 2006.

[46] SLIM5 Collaboration. Silicon detectors with Low Interaction with Material.

[47] UTfit Collaboration. *JHEP 0507, 028*, 2005.

[48] Hamamatsu Company. `http://sales.hamamatsu.com/en/products/solid-state-division/siphotodiode-series/mppc.php`.

[49] Saint-Gobain Crystals. `http://www.detectors.saint-gobain.com/fibers.aspx`.

[50] M. Gronau D. Atwood and A. Soni. *Phys. Rev. Lett. 79, 185*, 1997.

[51] M. Hazumi D. Atwood, T. Gershon and A. Soni. *Phys. Rev. D 71, 076003*, 2005.

[52] D.V.Pestrikov. Vertical Synchrobetatron Resonances due to Beam-Beam Interaction with Horizontal Crossing. *Nucl. Instr. Methods Phys. Res., Sect. A 336, 427*, 1993.

[53] C. Piemonte et al. *Il Nuovo Cimento C, vol. 30, no. 5, pp. 473-482.*

[54] Heavy Flavour Averaging Group (E. Barberio et al.). *arXiv:hep-ex/0603003.*

[55] W.-M. Yao et al. *Review of Particle Physics, J. Phys. G 33, 1*, 2006.

[56] B. Aubert et al. [BABAR Collaboration]. *"The BABAR Detector", Nucl. Instrum. Methods Phys. Res., Sect. A 479, 1*, 2002.

[57] M. Bona et al. [UTFit Collaboration]. *JHEP 0507, 028*, 2005.

[58] American Society for Testing and Materials. Standard practice for characterizing neutron fluence spectra in terms of an equivalent monoenergetic neutron fluence for radiation hardness testing of electronics. 1993.

[59] T. Gershon and A. Soni. *J. Phys. G: Nucl. Part. Phys. 34, 479*, 2007.

[60] T. Gershon and A. Soni. *J. Phys. G: Nucl. Part. Phys. 34, 479*, 2007.

[61] M. Gronau and D. London. *Phys. Rev. Lett. 65, 3381*, 1990.

[62] M. Gronau, J. L. Rosner, and J. Zupan. *Phys. Rev. B* **74***, 093003*, 2006.

[63] Y. Grossman, Z. Ligeti, Y. Nir, and H. Quinn. *Phys. Rev. B* **68***, 015004*, 2003.

[64] S. Hashimoto and M. Hazumi. *KEK-REPORT-2004-4*, 2004.

[65] K. Ikado and al. *Phys. Rev. Lett. 97, 251802*, 2006.

[66] A. Ishikawa and al. [Belle Collaboration]. *Phys. Rev. Lett. 96, 251801*, 2006.

[67] M. Iwasaki and al. [Belle Collaboration]. *Phys. Rev. D 72, 092005*, 2005.

[68] T. Kawasaki and al. Vertex detector for super belle experiment. *Nucl. Instr. Methods Phys. Res., Sect. A 560,195*, 2006.

[69] R. Kleiss and H. Burkhardt. *Comput. Phys. Commun. 81,372*, 1994.

[70] P. Koppenburg and al. [Belle Collaboration]. *Phys. Rev. Lett. 93, 061803*, 2004.

[71] Kuraray. `http://df.unife.it/u/baldini/superB/Kuraray.pdf`.

[72] O. Long, R. N. Cahn, and D. Kirkby. *Phys. Rev. D* **68***, 034010*, 2003.

[73] M. Misiak and al. *Phys. Rev. Lett. 98, 022002*, 2007.

[74] E.A. Kuraev M.S. Zolotarev and V.G. Serbo. *INP-Preprint 81-63, Novosibirsk*, 1987.

[75] M. Nakao and al. [Belle Collaboration]. *Phys. Rev. D 69, 112001*, 2004.

[76] S. Nishida and al. [Belle Collaboration]. *Phys. Rev. Lett. 93, 031803*, 2004.

[77] K. Ohmi and al. Luminosity Limit due to the Beam-Beam Interactions with or without Crossing Angle. *Phys. Rev. ST Accel. Beams 7, 104401*, 2004.

[78] P.Chen. *Proceedings DPF Summer Study SNOWMASS'88, World Scientific*, 1989.

[79] A. Poluektov and al. [Belle Collaboration]. *Phys. Rev. D 73, 112009*, 2006.

[80] P. Raimondi. *"Status of the SuperB Effort," presentation at the 2nd Workshop on Super B Factory, LNF-INFN, Frascati*, 2006.

[81] P. Raimondi and M. Zobov. DAFNE Technical Note G-58. 2003.

[82] G. Rizzo and al. A Novel Monolithic Active Pixel Detector in 0.13 μm Triple Well CMOS Technology with Pixel Level Analog Processing. *Nucl. Instr. Methods Phys. Res., Sect. A 565, 195*, 2006.

[83] D. Schulte. *Ph. D. thesis, University of Hamburg*, 1996.

[84] S.Korpar and al. *Nucl. Instrum. Methods Phys. Res., Sect. A 553*, 2005.

[85] Geant4 task force. `http://geant4.cern.ch/support/proc_mod_catalog/physics_lists/referencePL.shtml`.

[86] Y. Ushiroda and al. [Belle Collaboration]. *Phys. Rev. D 74, 111104*, 2006.

[87] J. Va'vra and al. *SLAC-PUB-12803*, 2007.

[88] J. Va'vra and al. *Nucl. Instrum. Methods Phys. Res., Sect. A 606*, 2009.

[89] M. Winter and al. Contributed paper to Vith International Meeting on Front End Electronics for High Energy, Nuclear, Medical and Space Applications, Perugia, Italy. 2006.

[90] K. Yokoya and P. Chen. Beam-beam phenomena in linear colliders. *Proceeding of a Topical Course held at the Joint US-CERN School on Particle Accelerators*, 1990.

[91] J. Zupan. *arXiv:hep-ph/0701004*.